Measuring the energies and multiplicities of prompt gamma-ray emissions from neutron-induced fission of ^{235}U using the STEFF spectrometer

James Andrew Ryan

A thesis submitted to the University of Manchester for the degree of Doctor of Philosophy in the Faculty of Science and Engineering.

School of Physics and Astronomy

University of Manchester

2017

Contents

List of Figures

List of Tables

Abstract

ABSTRACT OF THESIS submitted to the University of Manchester by James Andrew Ryan for the Degree of Doctor of Philosophy and entitled Measuring the energies and multiplicities of prompt gamma-ray emissions from neutron-induced fission of ^{235}U using the STEFF spectrometer.

Date of submission: 25/09/2017

Following a NEA high priority nuclear data request, an experimental campaign to measure the prompt γ-ray emissions from ^{235}U has been performed. This has used the STEFF spectrometer at the new Experimental Area 2 (EAR2) within the neutron time-of-flight facility (n_TOF), a white neutron source facility at CERN with energies from thermal to approximately 1 GeV.

Prior to the experimental campaign, STEFF has been optimised for the environment of EAR2. The experimental hall features a high background γ-ray rate, due to the nature of the spallation neutron source. Thus an investigation into reduction of the background γ-ray rate, encountered by the NaI(Tl) detector array of STEFF, has been carried out. This has been via simulations using the simulation package FLUKA. Various materials and shielding geometries have been investigated but the effects determined to be insufficient in reducing the background rate by a meaningful amount.

The NaI(Tl) detectors have been modified to improve their performance in a high count rate environment, and their behaviour characterised to understand the response to higher count rates. Initial testing demonstrated that the modified detectors maintain a potential to measure γ-ray multiplicities up to 3 counts per microsecond. However, the energy resolution fails somewhere below 1.75 counts per microsecond.

The experimental campaign has produced a large amount of data. The preliminary analysis of phase one data has considered incoming neutron energies ranging from thermal to an upper limit of 1 eV, with a minimum γ-ray energy threshold of 160 keV. Results have been achieved for the prompt fission γ-ray multiplicity and total energy of $M_\gamma = 6.3 \pm 0.2$ and $E_{S,\gamma} = 9.0 \pm 0.1$ MeV respectively. Further work is ongoing by the STEFF team at Manchester to improve upon these results and analyse the remainder of the data set at higher incoming neutron energies.

Declaration

No portion of the work referred to in this thesis has been submitted in support of an application for another degree or qualification of this or any other university or other institute of learning.

Copyright Statement

1. The author of this thesis (including any appendices and/or schedules to this thesis) owns certain copyright or related rights in it (the ”Copyright”) and s/he has given The University of Manchester certain rights to use such Copyright, including for administrative purposes.

2. Copies of this thesis, either in full or in extracts and whether in hard or electronic copy, may be made only in accordance with the Copyright, Designs and Patents Act 1988 (as amended) and regulations issued under it or, where appropriate, in accordance with licensing agreements which the University has from time to time. This page must form part of any such copies made.

3. The ownership of certain Copyright, patents, designs, trade marks and other intellectual property (the ”Intellectual Property”) and any reproductions of copyright works in the thesis, for example graphs and tables (”Reproductions”), which may be described in this thesis, may not be owned by the author and may be owned by third parties. Such Intellectual Property and Reproductions cannot and must not be made available for use without the prior written permission of the owner(s) of the relevant Intellectual Property and/or Reproductions.

4. Further information on the conditions under which disclosure, publication and commercialisation of this thesis, the Copyright and any Intellectual Property and/or Reproductions described in it may take place is available in the University IP Policy (see http://documents.manchester.ac.uk/DocuInfo.aspx?DocID=487), in any relevant Thesis restriction declarations deposited in the University Library, The University Library’s regulations (see http://www.manchester.ac.uk/library/aboutus/regulations) and in The University’s policy on Presentation of Theses.

Acknowledgements

I would like to thank my supervisor Prof. Jon Billowes and my advisor Dr. Gavin Smith for giving me the opportunity to work not only in a leading nuclear physics department but also to work with a very interesting experiment in an exciting experimental facility at CERN. A huge amount of gratitude must also be extended to Dr Toby Wright for all the assistance he has provided these past 4 years, his contributions could fill an acknowledgements section by itself.

A big thank you to the two Andys, for their work developing and building STEFF at n_TOF. I would also like to thank the n_TOF collaboration for the huge amount of assistance provided before, during and after the STEFF experiments. The local team especially deserve thanks for making me feel welcome during my time in France. Thanks are also extended to Stuart Warren for his work during the STEFF campaigns.

Thank you to the 4th floor PhD office for providing countless hours of entertainment over the years, along with some questionable quotes. A big thanks to Lawrie and Patrick for putting me up on my several returns to Manchester in my final write-up phase.

And of course a huge, huge thank you to Danielle. You have put up with a lot more than most people would, and have made the last two years of my life that much better. This document is a testament to your effort and patience just as much as my own.

1

Motivation & Objectives

1.1 Motivation

The NEA (*Nuclear Energy Agency*) compile a 'High Priority Request List' designed to gather in one place all nuclear data measurement requirements considered most beneficial to the nuclear industry [1]. One such request is the increased precision for measurements of the prompt γ-ray emissions from the ^{235}U(n,f) reaction. A prompt γ ray is typically one that is emitted within a few nanoseconds of the fission process occurring. A more thorough description of prompt γ rays can be found in Section 2.2.1.

The motivation behind this high-priority request is that the energy from the γ rays accounts for roughly 10% of the total energy released in the core of a nuclear reactor. Due to the propagation of these γ rays, this has a domninant effect on the total heating across the entire reactor. Of this fraction approximately 40% comes from the prompt γ rays emitted by fission fragments. Due to this large contribution in overall energy produced within a nuclear reactor, any uncertainties in the prompt fission fragment γ-ray data are potential major sources of uncertainty when determining the heating effects within reactors [2]. Much of the current data in the nuclear data libraries concerning γ-ray energy, and multiplicity spectra comes from the early 1970's [3–5]. New measurements have been performed more recently (summarised in 1.2.1), however the results achieved by these continue to vary significantly (on the order of 15% of the measured energy). Therefore

improvements on these measurements are strongly desired. Since the original request a further review of past findings and new findings has concluded that there is still significant dispersion between quoted results and that this must be improved [6]. A further motivation behind this data request results from the fact that the early measurements of these prompt γ rays focused only on neutron induced fission using thermal neutrons. Nuclear reactors which use a fast neutron spectrum are gaining more interest, both as methods of producing power and experimental reactors [7, 8]. The Jules-Horowitz Reactor is one example of an experimental reactor which utilises a fast neutron spectrum. In order for experiments carried out within such a reactor it is imperative that systematic uncertainties (such as those present due to γ ray heating effects due to prompt emissions) are as well understood and characterised as possible. For this reason the data request stipulates an even more precise measurement for the uncertainty to support Jules Horowitz Reactor operations (5% uncertainty for JHR vs. 7% in the standard request) [6, 8].

The NEA have requested that uncertainties on these measurements be reduced to below 7%, or 5% in order to support the Jules Horowitz Reactor. The proposed experiment hopes to achieve this, along with the added benefit of improving current standards for measurements of prompt γ rays emitted when fission is induced by a higher energy neutron (i.e. in the region of 1 MeV).

1.2 Objectives

The objective of the work described within this thesis is to provide more precise data for prompt γ-ray emissions by utilising a novel technique which enables the highlighting of any systematic uncertainties in other measurements. The measurements described within are the result of a unique combination of a 2E,2v fission device (described in detail in Chapter 4) in coincidence with γ-ray detection. Combining this with a white neutron source allows data to be taken simultaneously at low neutron energies (where it can be compared with other results using different experimental techniques) and also at higher neutron energies, providing new insights and significant uncertainty reductions.

1.2.1 Previous Works

Along with previous work performed by the STEFF detector [9–11], there has been a great interest in the measurement of prompt γ rays for a number of years. Several of these measurements have been collated within Table 1.1 along with an entry from one of the industry standard evaluated data library, ENDF/VII-B [12], for comparison. Dedicated measurements of the prompt γ-ray emission from thermal fission of ^{235}U dates as far back as the 1970s [3–5]. These experiments have varied in many ways, the key differences being the system energetics (neutron energies and γ-ray energies examined), the fissile target properties, and the detector setups involved. These are discussed in further detail below.

Table 1.1: Collection of previous measurements for average γ-ray multiplicity and energy, per fission of ^{235}U, along with the neutron energy range considered.

Cited Work	Average Multiplicity, $\bar{\nu}_\gamma$	Average γ-ray Energy, (ε_γ) (MeV)	Total Emitted Energy, $E_{\gamma,total}$ (MeV)	Neutron Energy Range
Verbinski (1973) [5]	6.70 ± 0.30	0.97 ± 0.05	6.51 ± 0.30	Thermal (0.025 eV)
Pleasonton (1972) [4]	6.51 ± 0.30	0.99 ± 0.07	6.43 ± 0.30	Thermal
Peelle (1971) [3]	7.45 ± 0.35	0.96	7.18 ± 0.26	Thermal
Obserstedt (2014) [13]	8.19 ± 0.11	0.85 ± 0.02	6.92 ± 0.09	Thermal
DANCE (2015) [14]	7.35 ± 0.35	N/A	8.35 ± 0.40	Thermal - 100 keV
ENDF/B-VII [12]	6.86	0.96	6.58	Thermal
STEFF (2015) [9]	7.74 ± 0.12	1.08 ± 0.03	8.40 ± 0.26	Thermal

System Energetics

Table 1.1 demonstrates that, historically, measurements have been focused on thermal neutron induced fission primarily, with five of the previous six measurements listed focusing solely on thermal energies (discounting the ENDF entry as this is an amalgamation of many previous measurements). The measurement by Wu is the only previous measurement detailed here to break this trend, increasing the energy threshold to neutrons with an energy of 100 keV. The work discussed in this thesis details an experiment which utilises a white neutron energy spectrum, reaching energies greater than 1 MeV. However the analysis and results presented have only considered up to 1 eV, with the remainder of the data

set to be analysed in the future.

The γ-ray energy threshold applied in previous results has varied from 10 keV, in the measurement by Oberstedt, to 150 keV, in the measurement by Wu. The results quoted in this thesis have been achieved utilising a threshold of 160 keV. As this has been applied digitally in post-processing, it may be possible in the future to re-analyse these data utilising a lower threshold if this becomes feasible (due to dealing with the high background issues discussed later within the thesis).

Target Properties

Most of the previous measurements (including the previous STEFF measurement) have utilised highly enriched uranium metal targets. The experiment discussed in Pleasonton, however, used a ceramic U_3O_8 target. All targets used have been highly enriched (above 99%) in uranium-235.

This experiment was divided into two phases, the first utilising a metal target and the second utilising a ceramic UO_2 target. This way it should be possible, once data from both phases is analysed, to understand any systematic effects which could arise due to the different target types considered.

Detector Setups

The detector setups for the early measurements were relatively simple, consisting of a fission tagging detection method (e.g. a PPAC chamber) in conjunction with some form of γ-ray detector. As time has progressed the methods to measure and characterise the fission process have grown more sophisticated, and have the ability to characterise properties of the fission fragments themselves, in conjunction with use as triggers for prompt γ-ray detection. One such system is the 2E,2v method used by STEFF which can produce a large amount of information about the fission fragments themselves, along with providing an accurate measure of the γ-ray emissions from fission events. Oberstedt [13] have utilised such a method whilst using a variety of lanthanide-halide scintillators, which are capable

of providing extremely fast timing responses. In this measurement, γ rays were measured in coincidence with fission fragments via utilisation of multiple ionisation chambers.

These measurements have used either a single or small number of γ-ray detectors. The measurement described by Wu has used a 4π array of BaF_2 scintillators, in order to maximise efficiency in detecting the prompt γ-ray spectrum. The fission fragment tagging method for this experiment was a PPAC detector.

Measurements using STEFF, including the one discussed and analysed within this thesis, use a double fission tagging method to isolate prompt fission γ rays. This is achieved via a set of gaseous ionisation chambers, along with fast timing response micro-channel plates (MCPs) and multi-wire proportional counters (MWPCs) to determine fission fragment characteristics. Twelve sodium iodide scintillators (NaI(Tl)) are placed around the central target chamber of STEFF, to measure the γ-ray response, covering a solid angle of approximately 25%. Further details on the STEFF spectrometer can be found in Chapter 4.

2

Theory

It is hard to say exactly when the discipline of nuclear physics was first established. Ernest Rutherford discovered in 1911 that at the centre of an atom existed a very dense, positively charged core, which he called a nucleus. The decades before this discovery had been abuzz with revelations; from Becquerel discovering radioactivity to Curie discovering radium [15]. However it was not until the late 1930s that the concept of nuclear fission began to assemble in physicists' minds, and despite great strides being made at a rapid pace, nuclear fission is such a complex process that to this day theory is still unable to predict every aspect of the fission process. Thus necessitating experiments to probe the process more deeply [16]. This chapter will discuss an outline of the fundamental physics underpinning the nuclear fission process.

2.1 Nuclear Fission

When James Chadwick discovered the neutron in 1932 it constituted a way to probe and interact with nuclei that could evade the repulsive Coulomb forces encountered when attempting to use protons or alpha particles. This prompted Enrico Fermi to begin a suite of work bombarding a wide range of elements with these newly discovered neutrons. In 1934 he published what he thought was the discovery of the first *transuranic* elements, though it was later discovered that he had unknowingly discovered fission. It was not until

1938 when Otto Hahn and Fritz Strassmann proved that the products of Fermi's reactions were in fact barium and other lower mass elements that there was concrete evidence nuclear fission had indeed occurred. Lise Meitner and Otto Frisch then proceeded to suggest the mechanism through which nuclear fission was occurring, i.e. that a uranium nucleus was capturing a neutron, leading to instability within the nucleus and subsequent splitting. Furthermore they calculated the expected energy release to be 200 MeV, which was later confirmed experimentally by Frisch[16, 17].

Such a large energy release from a single reaction was hitherto unprecedented. The energy release from nuclear energy being orders of magnitude greater than energy released by chemical interactions. Figure 2.1 demonstrates where this energy actually comes from. This graph depicts the nuclear binding energy per nucleon. This intrinsic nuclear energy binds the nucleus together and is the source of the huge release of energy during fission. For heavier elements, to the right of the graph, the binding energy per nucleon is around 7.5 MeV. The nuclei produced via the fission process have individual masses in the range of 90 - 140 atomic mass units (amu), for which the binding energy per nucleon is closer to 8.5 MeV. It is this increase in binding energy between the original and product nuclei that is the source of the release.

2.1.1 The Liquid Drop Model

Analogies can be drawn between the properties dictating the binding energy of a nucleus and those dictating the stability of a uniformly charged liquid drop [18]. The result of this analogy is encapsulated within the formula for binding energy, known as *The Semi-Empirical Mass Formula* (Equation 2.1). As the name dictates, this is a formula which is derived partly theoretically and partly based on empirical measurements. More specifically, the general terms have their root in theory but the coefficient of each term is found via experiment. The first three terms of the formula originate from a macroscopic description of the nucleus (and subsequent parallels drawn to a liquid drop).

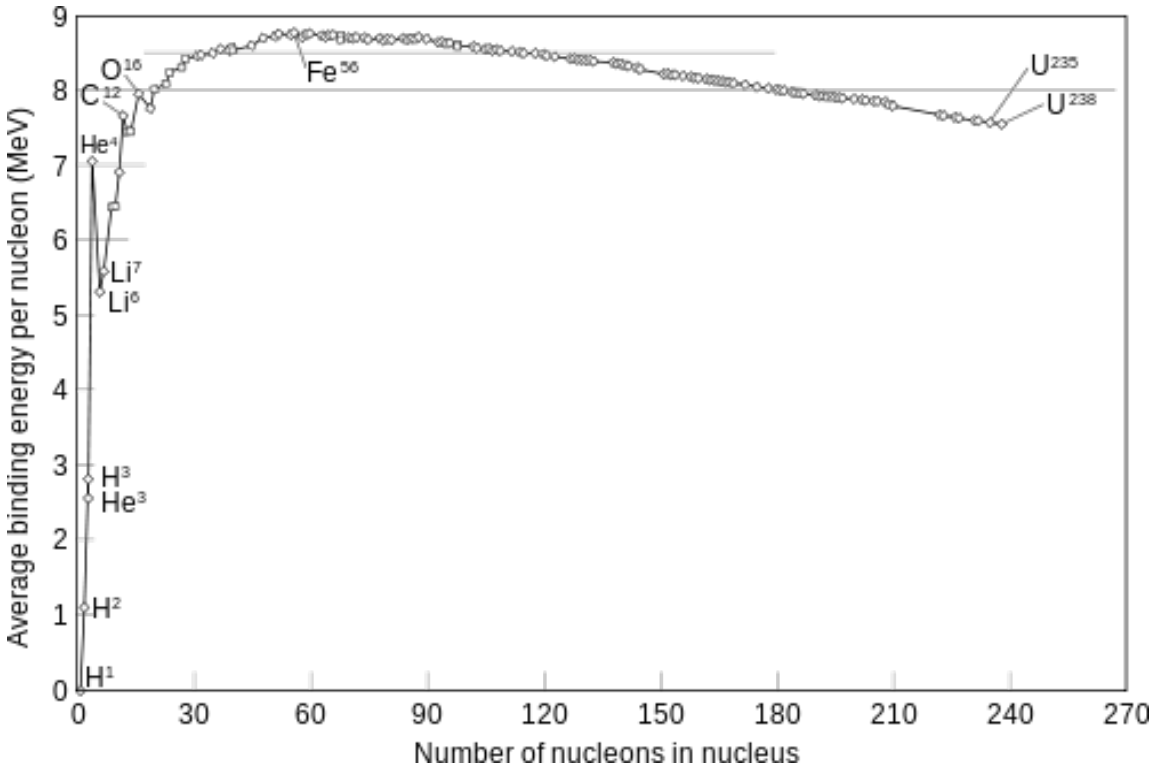

Figure 2.1: Graph to show how the binding energy per nucleon changes with nucleon number. As the curve peaks at A=56, large, heavy elements splitting into two smaller elements will release energy; and small, light elements combining into a single heavier element will also release energy. Created using data from the Atomic Mass Data Center[19].

$$E_B(Z,A) = a_V \cdot A - a_S \cdot A^{2/3} - a_C \cdot Z(Z-1) \cdot A^{-1/3} - a_{Sym} \cdot \frac{(A-2Z)^2}{A} + \delta \qquad (2.1)$$

The first term, $a_V \cdot A$, is known as the volume term. To a first order, as the volume of a nucleus increases so does the binding energy. Each nucleon binds with the other nucleons within the nucleus, thus the total binding energy is proportional to the number of nucleons, A.

The second term, $-a_S \cdot A^{2/3}$, is the surface term. This is a correction factor to the volume term as the first term over-estimates the total binding energy. This is due to the fact that nucleons towards the edge of the nucleus will interact with fewer other nucleons, and thus cannot influence the binding energy as much.

The third term, $-a_C \cdot Z(Z-1) \cdot A^{-1/3}$, is the Coulomb term. This term is due to the protons within the nucleus repelling one another. Since the number of distinct interactions between Z protons is $Z(Z-1)$ this term is proportional to that, along with being inversely

proportional to $A^{1/3}$ to account for the Coulomb potential having a $\frac{1}{r}$ dependence.

The sum of these terms is almost sufficient to describe fully the binding energy curve, however there are two additional corrections which must be made before the correct formula is fully reproduced. These terms depend not on macroscopic properties derived from the liquid-drop model, but on microscopic properties of the nucleus. There is the asymmetry term and the nuclear pairing term.

The asymmetry term, $-a_{Sym} \cdot \frac{(A-2Z)^2}{A}$, accounts for the stability of a nucleus for which $N = Z$, due to the effect of the Pauli exclusion principle when filling nucleon energy levels within a nucleus. A large disparity in neutron number, N, and proton number, Z, results in a higher energy state. The pairing term, δ, has a very small, but important, effect on binding energy. This pairing term is representative of the increased stability of so-called "even-even" nuclei, i.e. the number of protons and the number of neutrons are both even. The reverse of this being that an odd-odd nucleus is slightly detrimental to stability (and an odd-even nucleus has no pairing term). The pairing term is shown further in Equation 2.2.

$$\delta(Z,A) = \begin{cases} +\left(\frac{a_P}{A^{1/2}}\right) & \text{N and Z are EVEN} \\ -\left(\frac{a_P}{A^{1/2}}\right) & \text{N and Z are ODD} \\ 0 & \text{N is ODD and Z is EVEN, or N is EVEN and Z is ODD} \end{cases} \tag{2.2}$$

The final form, as described in Equation 2.1, is known as the *Weizacker mass formula* and the values of the coefficients, a_i, depend slightly on specific binding energies used when deriving values. Common values for the coefficients (taken from [20, 21]) are $a_V = 16\,MeV$, $a_S = 18\,MeV$, $a_C = 0.7\,MeV$, $a_{Sym} = 24\,MeV$, and $a_P = 11.18\,MeV$.

The fission process itself can be described, qualitatively, by reference to this liquid-drop model. Figure 2.2 shows a step-by-step breakdown of the fission process and how this can be likened to a liquid droplet splitting into two smaller droplets. For all but the extremely heavy elements (i.e. masses above the order of $A \sim 240$) there is an energy barrier

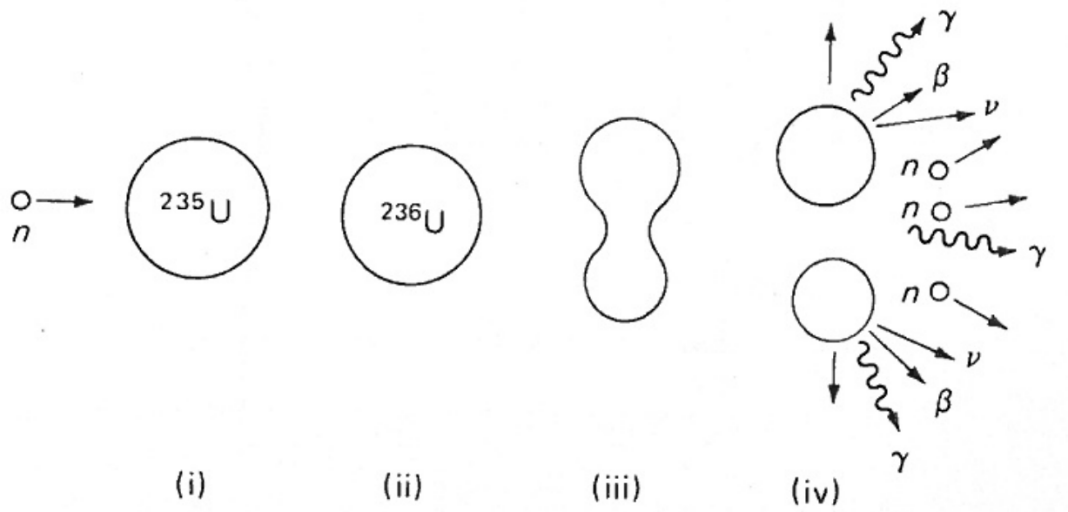

Figure 2.2: Schematic representation of nuclear fission in analogy to the splitting of a liquid drop. (i) Neutron & nucleus interaction, (ii) Compound ^{236}U nucleus, (iii) Deformation/necking of the excited nucleus, and (iv) Fission fragments. This schematic has condensed the primary and secondary fragment decays into a single step.[22]

to overcome, known as the *Fission Barrier*, before the fission process can occur; as demonstrated in Figure 2.3. A nucleus may overcome this fission barrier spontaneously or the required energy may be supplied via an external particle, as is the case in neutron-induced fission. Spontaneous fission is a relatively rare phenomenon, typically only occurring for very heavy elements that meet the condition described in Equation 2.3. However, due to quantum-tunnelling, it is possible to observe spontaneous fission for nuclei not meeting this criterion, for example ^{238}U and ^{240}Pu.

$$\frac{Z^2}{A} \gtrsim 49 \tag{2.3}$$

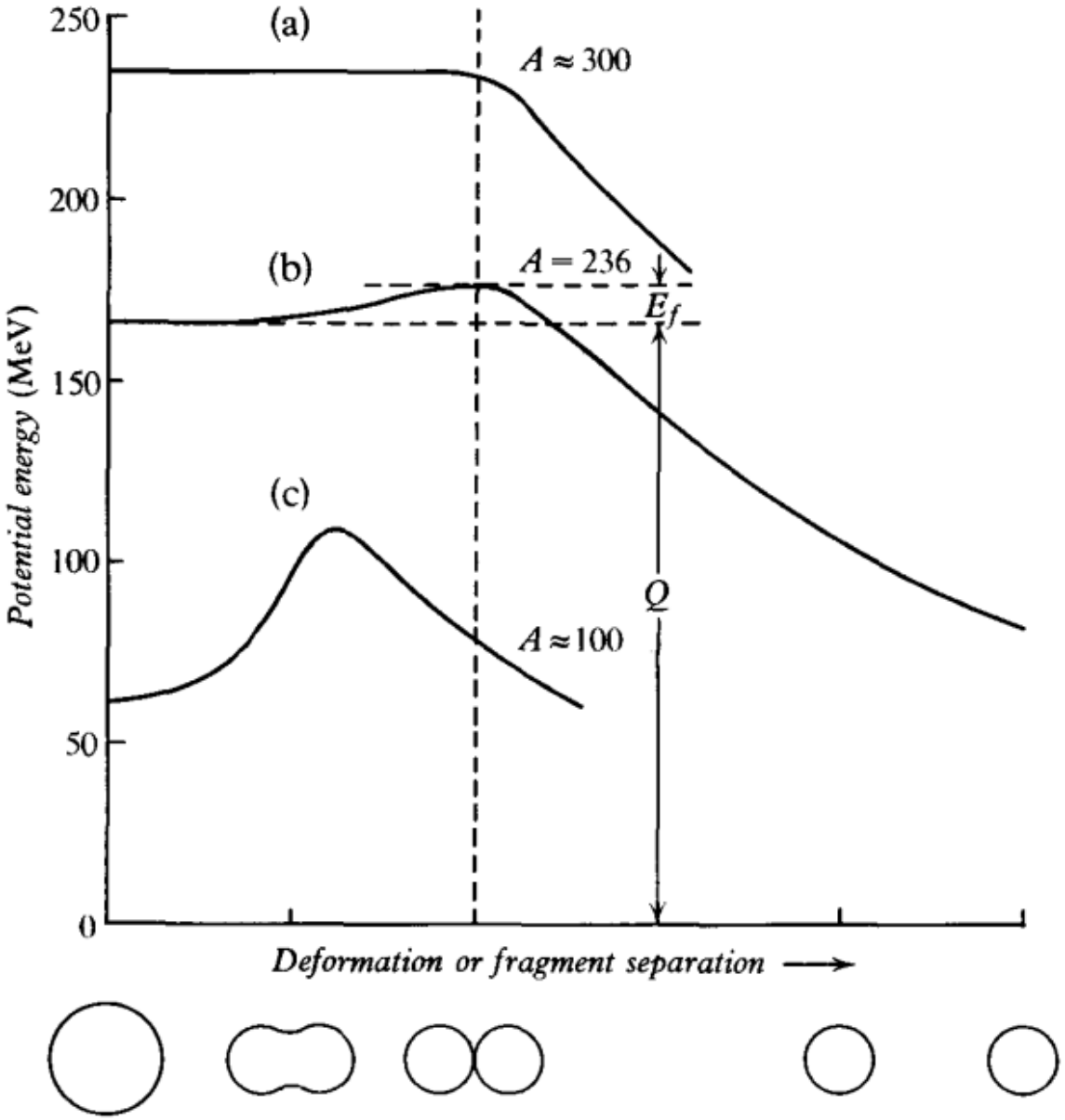

Figure 2.3: The energetics of the fission process for 3 values of parent atomic mass. Note that despite being overall exoergic (i.e. energy is ultimately released), the fission process needs to overcome the initial energy deficit of the fission barrier (E_f) in order for fission to take place. The overall energy released is Q. The vertical dashed line splitting the graph into two halves, the left showing the potential energy of the single-nucleus system, and the right showing how the energy of the system evolves after the fission event and the fragments separate due to mutual Coulomb repulsion.[23]

2.2 Products of the Fission Process

The most common type of fission within a nuclear reactor is neutron-induced fission. The subject of the experiment discussed in Chapter 7 is the neutron induced fission of uranium-235. Equation 2.4 demonstrates an example of this occurrence, but the products noted there are just one example of many possible outcomes. Approximately 200 MeV of energy is released per fission of ^{235}U nuclei. A breakdown of how this energy is distributed among all products of the fission process can be seen in Table 2.1. One can see that the majority of this energy is in the form of kinetic energy of the fission fragments with the remainder being split between prompt releases (both γ rays and neutrons), and secondary releases (daughter product decays).

$$n + {}^{235}_{92}U \rightarrow {}^{236}_{92}U^{*} \rightarrow {}^{147}_{57}La + {}^{87}_{35}Br + 2n \tag{2.4}$$

2.2.1 Primary Fission Products

The term primary fission products refers to those products created within the order of the first few nanoseconds of fission [25]. According to the timeline of fission in Figure 2.4 this includes the fission fragments themselves, along with any prompt neutrons or γ rays that are emitted during the fission process.

With thermal energy neutrons, the nuclear fission of uranium-235 almost always results in two fission fragments with significantly different mass, one so-called light frag-

Product	Energy (MeV)
Fission fragments	168
Prompt neutrons	5
Prompt γ rays	7
Capture γ rays	7
Daughter product β emission	8
Daughter product ν emission	12
Daughter product γ emission	6

Table 2.1: Energy distribution among products of ^{235}U fission (average values) [9, 24].

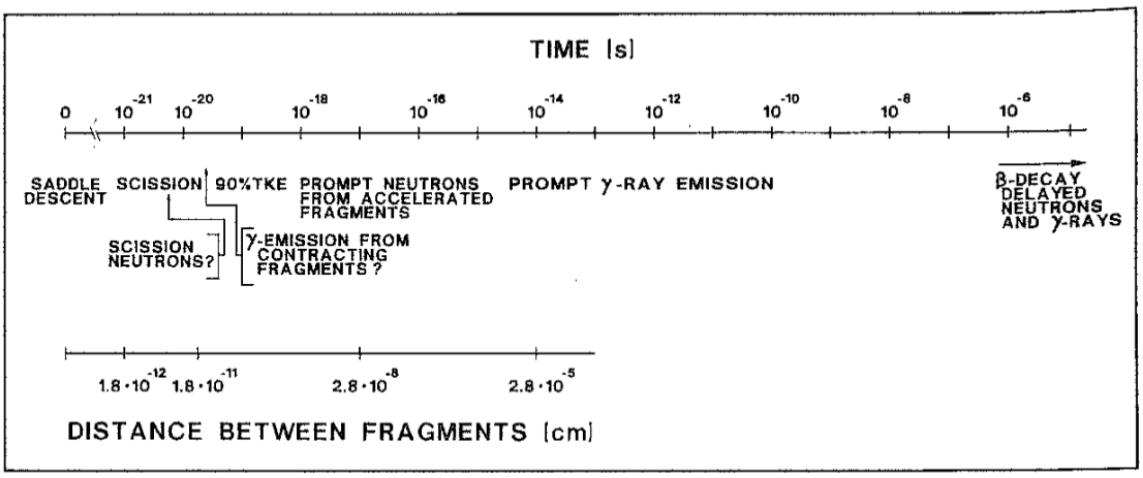

Figure 2.4: Annotated timeline of the fission process.[10]

ment and another so-called heavy fragment. This can produce a whole range of different isotopes (the fission yield distribution becomes more symmetric as neutron energy increases [26]). Figure 2.5 shows the distribution of fission fragments masses and their approximate yield. Note the fragment masses can vary from around 70 and 160 atomic mass units, with the most likely values being in the 96 and 135 region [27]. Fission fragments are formed with a high excitation energy and spin, typically around 20 MeV and 7 $\hbar$ respectively; additionally the fission fragments form as ions and thus gain further energy due to mutual Coulomb repulsion. To de-excite the fragment will subsequently emit neutrons and γ rays to reach a more stable state [29].

Prompt Neutrons

According to compound nuclear lifetime measurements and associated calculations, the emission of prompt neutrons occurs between 10^{-18} and 10^{-13} seconds after fission [30]. For neutron-induced fission, the multiplicity and energy spectra of these prompt neutrons depend upon the energy of the incoming neutron. On average, thermal-induced fission of uranium-235 releases 2.47 ± 0.08 prompt neutrons per fission, with an energy distribution shown in Figure 2.6 [31]. High energy incoming neutrons will result in greater multiplicities and shift the outgoing neutron energy spectrum higher, as a higher energy incoming neutron will result in a compound nucleus with greater excitation energy prior to fission-

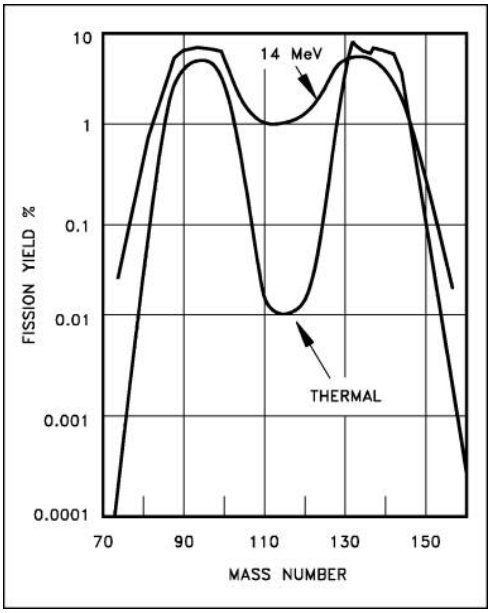

Figure 2.5: The fission fragment mass distribution for neutron-induced fission of U-235 for thermal and fast neutron energies, note the increased symmetry for the fast neutron yield [28].

ing. This in turn produces fission fragments with a higher excitation energy, potentially overcoming the minimum neutron emission energy by a large margin [30, 32].

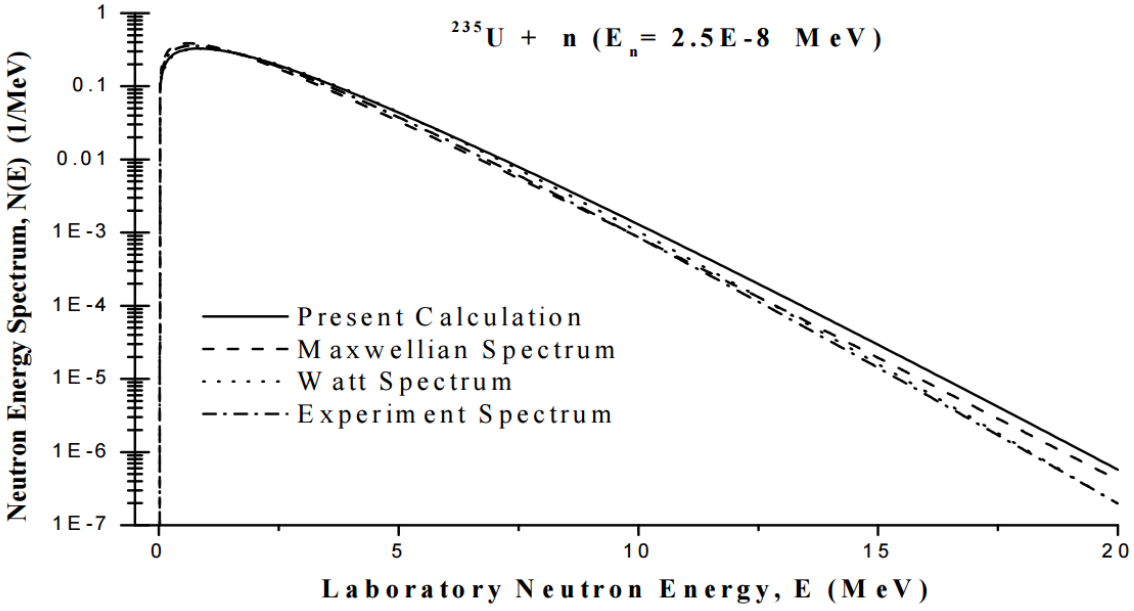

Figure 2.6: Prompt fission neutron spectrum, for various models, resulting from thermal neutron induced fission of ^{235}U [33].

Prompt γ rays

Emission of the prompt neutrons removes a large amount of energy and a small amount of angular momentum. The daughter nuclei remain in a highly excited state, each fragment possessing an average excitation of 4 MeV, along with retaining large amounts of angular momentum ($6\hbar$) [34]. This excitation energy and angular momentum is removed via the emission of prompt γ-rays. These γ-rays which remove orbital angular momentum may be classed as a function of the quantum number L. The majority of these γ rays are dipole, $L = 1$, or quadrupole $L = 2$.

The prompt γ-ray decay of a fission fragment can be considered in two manners. Initially the excited nucleus will decay via emitting a small number of high-energy γ rays, each carrying little spin; such γ rays are known as *statistical* γ *rays*. These statistical γ rays are electric dipole (E1) transitions. The number of statistical γ rays depends upon the excitation of the fragment but typically there are between one and three of these emitted per fragment.

Following these emissions the nucleus is in a lower excited state but still retains a considerable amount of angular momentum (2-2.5 MeV, spin $5\hbar$). In order to remove the angular momentum, along with any persistent excitation energy, the nucleus emits several γ rays carrying high spin but low energy. These are known as *yrast* γ *rays*, and are due to quadrupole transitions (E2) [34]. Figure 2.7 depicts a simplified graphical representation of this dual emission treatment.

A statistical model predicting the probability $P(J_i)$ of the initial spin state, J_i, of the fission fragment is described in detail in [35]. This can be summarised by the expression,

$$P(J_i) \propto (2J+1) \cdot \exp\left[\frac{(J_i+1/2)^2}{B^2}\right], \tag{2.5}$$

where B is proportional to the root mean square of the angular momentum, J_{rms} of the fission fragment. This model is used later in Chapter 8 to calculate the γ-ray multiplicity measured by STEFF.

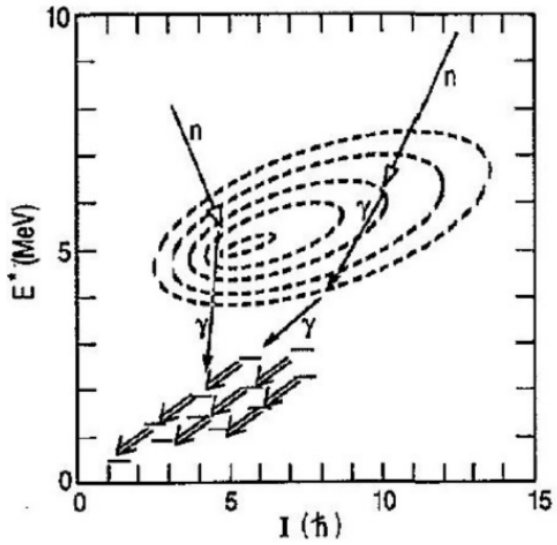

Figure 2.7: A simplified representation of the decay of a fission fragment following emission of prompt neutrons. A clear distinction between the two types of γ ray (*statistical* and *yrast*) can be seen [29].

Angular Distribution

The fission fragment and γ rays produced during the fission process are emitted in a non-isotropic fashion, there is an angular distribution. In a fission-tagging experiment, such as the one discussed in this thesis, it is important to understand the angular distribution of the emitted prompt γ rays, relative to the direction of travel of each fission fragment, since this will affect the efficacy of detecting γ rays based on the location of the γ-ray detector. Skarsvåg has investigated this angular distribution for thermal fission of uranium-235, and the results can be found in Figure 2.8 [36]. It can be seen that the angular dependence varies up to approximate 20% between 0 and 90 degrees. This relationship is important to include in the analysis, as variation in detector positioning could lead to a large shift in measured results.

2.2.2 Secondary Fission Products

The heavier elements on the periodic table have a neutron to proton ratio around ~ 1.5, whereas for medium-mass elements this ratio is closer to $1.3 \sim 1.4$. The result of this is that when a heavy nucleus splits and forms two lighter nuclei, even after the prompt neu-

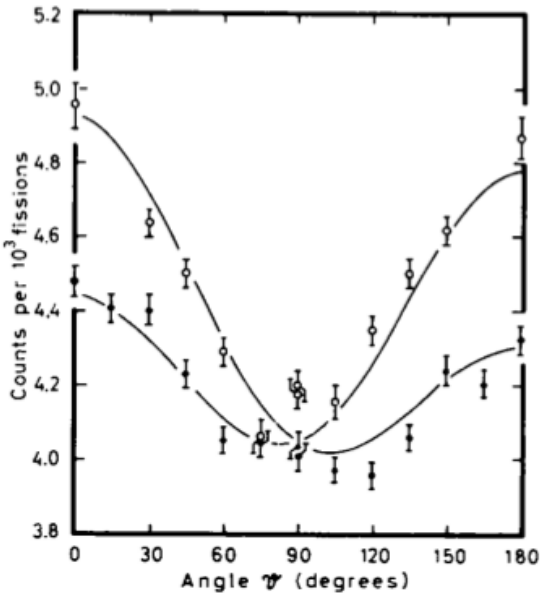

Figure 2.8: The angular distribution of γ rays relative to the direction of motion of the light fission fragment, as measured by Skarsvåg [36]. The different symbols used (dots and circles) represent different geometries used in the underlying measurement. The solid lines correspond to γ-ray emissions after the light fragment has been stopped in the target backing which was present.

tron evaporation, the two fission fragment products are neutron-rich, and thus unstable. It is this instability that gives rise to so-called secondary fission products. These are the products emitted, in accordance with the timeline above, more than one microsecond after the fission event has taken place. The unstable fission fragment nuclei may decay in a variety of manners, typically β^- decay and γ decays. However, sometimes the instability of the fragment nucleus is so great a β-delayed neutron is ejected. It is these delayed neutrons that enable nuclear fission power reactors to be able to function. As these neutrons allow a degree of reactor control at timescales with which human response is feasible (delayed neutrons typically appear at the order of seconds to minutes post-fission).

As can be seen then the process of nuclear fission is a very complex one, with many processes involved. This means that performing measurements to understand the many properties of the fission process is a difficult task. The many detection systems of the STEFF spectrometer allow many parts and processes of fission events to be measured, as will be discussed further in later chapters.

3

The Neutron Time-of-Flight (n_TOF) Facility

The neutron time-of-flight (n_TOF) facility at CERN was originally proposed by Carlo Rubbia in 1998, and the facility has been operational since 2001. The running of the facility can be considered in three distinct phases: phase one (2001-2004), phase two (2008-2012) and phase three (2014 - present). Each phase represents an important upgrade to the facility and its experimental capabilities [37, 38]. The primary objective of n_TOF is the measurement of neutron-induced reactions, typically neutron cross-sections but also other aspects of neutron-induced reactions. Since opening, n_TOF has measured several types of neutron reactions ((n,f),(n,α),(n,γ), etc.) using over forty different, distinct isotopes. This chapter describes the facility at which the experiment described within this thesis took place.

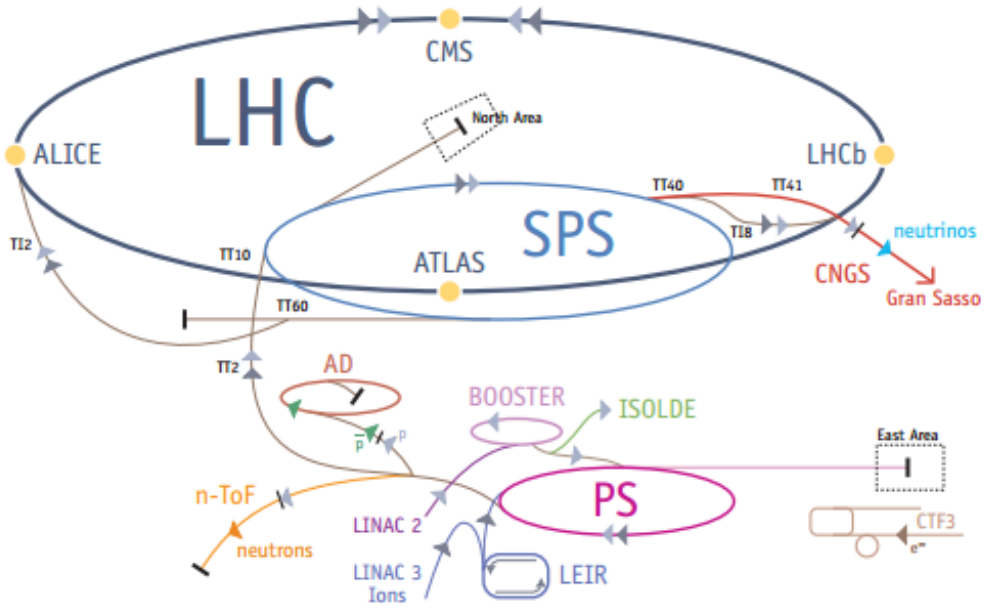

Figure 3.1: The CERN accelerator complex, showing the various accelerator rings and experimental facilities. The n_TOF facility can be seen in the lower left region of the diagram.

3.1 The n_TOF Facility

The n_TOF facility is situated as part of the 'Proton Synchroton' (PS) complex within the accelerator setup at CERN (see Figure 3.1). The facility utilises a beam of protons with 20 GeV/c momentum supplied by PS and these impinge upon a cylindrical lead target (40 cm in length and 60 cm in diameter). A 7 ns wide pulse of approximately 7×10^{12} protons strikes the lead target on average once every 1.2 seconds. The large, dense target (see Figure 3.2), coupled with the high energy of the impinging proton beam, means that each proton is capable of producing over 250 neutrons [39]. This results in a very high instantaneous neutron flux. Immediately surrounding the lead target is a 1 cm layer of water used to cool the target, as the high energy proton beam results in approximately 50 kJ of energy being deposited every 5 s [40]. Surrounding this layer of water on the front facing side of the target (i.e. towards the first n_TOF experimental area) is a second layer of borated water, 4 cm in thickness (H_2O + 1.28%H_3BO_3). This water acts as a moderator for the emerging neutrons, whilst the boron within the water lowers the in-

Figure 3.2: The current lead spallation target used at n_TOF, pictured during its installation.

beam γ-ray background by reducing the numbe of neutrons captured within hydrogen (which subsequently emits a 2.2 MeV γ ray). The result is an emerging neutron spectrum covering a range of energies from < 1 meV up to the order of several GeV [41].

Upon completion, the n_TOF facility consisted of a single experimental area (EAR1). This is composed of a 185 m flight path extending from the lead spallation target, horizontally, to an experimental hall. This experimental area has been operating successfully for 16 years and has measured the properties of numerous neutron induced reactions [42].

3.1.1 Experimental Area 2 (EAR2)

After the success of the original experimental area the expansion of n_TOF to include a second beamline, experimental area 2 (EAR2), was proposed by the n_TOF collaboration and approved by the CERN Research Board [43] in June 2012 [44, 45]. This expansion takes advantage of the fact that neutron emission from a spallation target occurs in an almost isotropic distribution once the neutrons have emerged from the surrounding

layers of water (in reality this distribution is slightly forward-focused). Construction of the new beamline and experimental area began in May 2013, concurrent with the 'Long Shutdown' [1] (LS1), and was completed in July 2014. After 18 months of shutdown the first 20 GeV/c proton beam pulse was sent to the n_TOF spallation target and the first neutron beams were observed in both areas on 25/7/2014. Six months of commissioning measurements followed in order to properly characterise the new beamline, so as to to accurately determine its properties; this was in addition to performing important, initial detector tests [46].

A computer-aided design (CAD) geometry of the EAR2 beamline can be seen in Figure 3.3. The distance shown from the spallation target at the base of the facility to the EAR2 bunker (i.e. the experimental hall) is approximately 20 m in length. This is shorter than the flight path length of EAR1 by a factor of 9.25. This neutron beamline contains magnets and collimators designed to shape the neutron beam and remove the majority of contaminants before reaching the experimental area. Furthermore there is a beam dump situated within the roof of the experimental area bunker, in order to prevent the neutrons escaping the facility. Both the beam dump and collimating system have been the subjects of intensive study and simulation work to ensure as low a background rate as possible is encountered by detectors utilised by experiments within the facility, as well as limiting the potential radiation dose rate experienced in nearby working areas [47]. The major features within the beamline are listed in Table 3.1, each of these must be carefully configured to meet their respective needs. A brief summary of each feature and its main purpose follows:

- 1st collimator – The first major piece of apparatus encountered by the neutron beam is the first beam collimator. This initial collimator is a simple one composed entirely of iron and featuring a cylindrical aperture with a constant 200 mm diameter. It is designed to provide some initial shaping of the neutron beam by using the dense

[1] A long shutdown is a prolonged halt of beam experiments in order for CERN to maintain and upgrade as necessary. LS1 began in February 2013. http://home.web.cern.ch/about/updates/2013/02/long-shutdown-1-exciting-times-ahead

iron to remove stray particles.

- Sweeping magnet – After the first collimator comes a 0.2 Tm permanent magnet which serves to remove charged particles from the neutron beam.

- Filter box – A filter box approximately half-way up the beamline containing isotopes which may be inserted into the path of the neutron beam, altering the neutron flux and aiding in the determination of the neutron induced background levels.

- 2nd collimator – A second collimator just before the experimental hall provides final shaping of the neutron beam to provide as well-defined a beam as possible for experiments within EAR2. This second collimator may either be a narrow collimator (20 mm diameter) or a wide collimator (70 mm diameter), as is required by a particular experiment. The geometry of this collimator depends on the type in question, varying in material and aperture size. The specific material arrangements used differ for the narrow and wide collimators, however both feature dense iron or steel to attenuate γ rays and a neutron absorbing material to remove stray neutrons from the beam. For an example geometry of these collimators, see Figure 3.4. The differences in these collimators are described later when discussing the experimental campaign.

- Experimental area – A large room (40.8 m^2 by 5 m high) in which experimental apparatus may be placed [44].

- Beam dump – Within the roof of the experimental hall there is a large beam dump, which absorbs any neutrons which may have travelled through the experimental area unimpeded. In order to do so most effectively, the beam dump above EAR2 is composed of several different materials. It contains a neutron moderator to slow the neutrons (borated polythene), a neutron capturing material to absorb the slowed neutrons (boron carbide) and then a high-Z material in order to attenuate any γ rays produced by the neutron moderation and absorption process (iron or steel).

[1]Only one of these 2nd collimators is present in the beam at any one time, dependent on the nature

Table 3.1: Beam line elements and their position with respect to the center of the n_TOF spallation target

Beam line element	Distance to spallation target centre (m)
1st collimator	7.4 – 8.4 (d = 200 mm)
Magnet centre	10.4
Filter box	11.4
[1]2nd collimator (narrow)	15.04 – 18.04 (d = 70 – 20 mm)
[1]2nd collimator (wide)	15.04 – 19.54 (d = 100 – 70 mm)
Experimental area	18.16 – 23.66
Beam dump	24.73

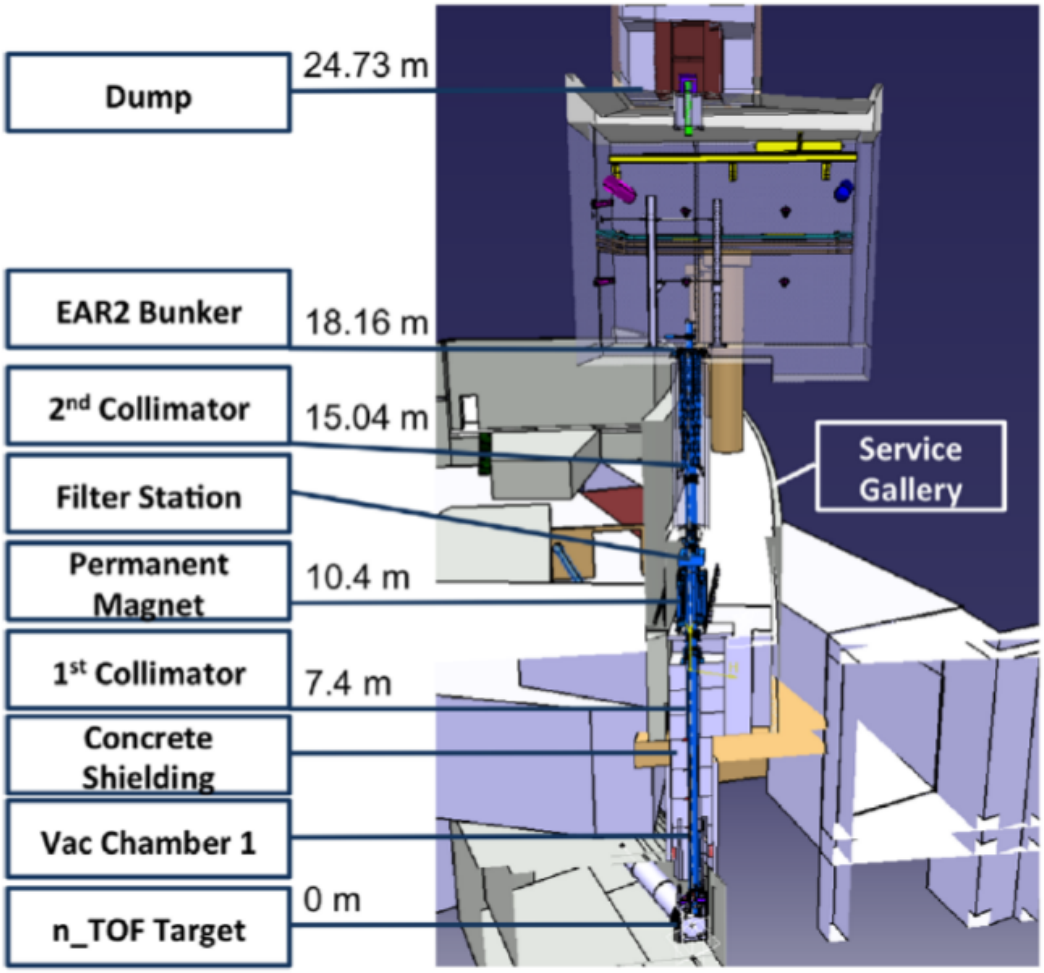

Figure 3.3: The layout of the EAR2 beamline, with key beam components and approximate distances from lead target labelled [48]

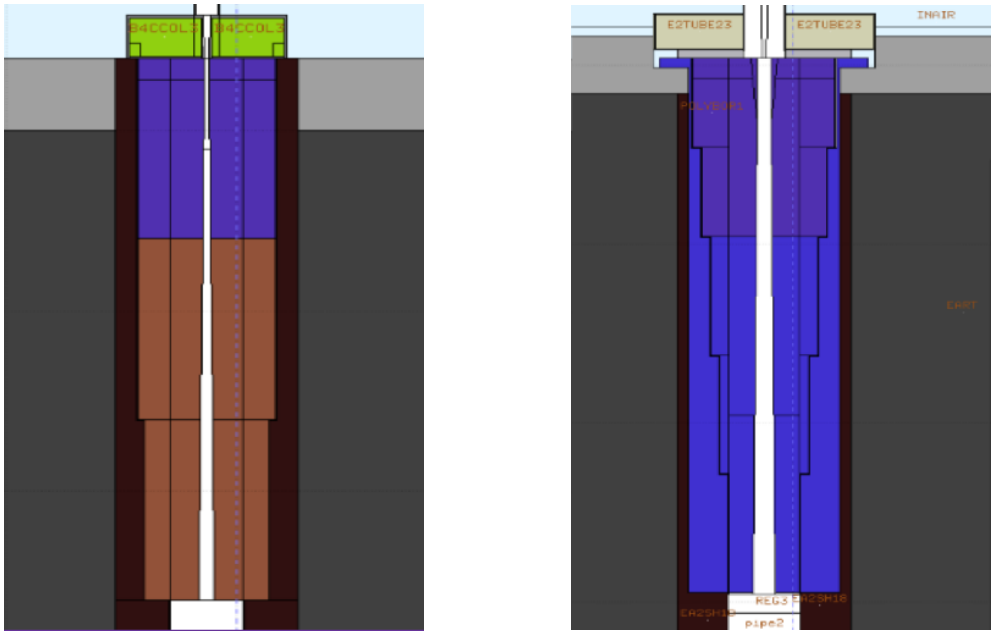

(a) The n_TOF EAR2 narrow collimator.

(b) The n_TOF EAR2 wide collimator.

Figure 3.4: Comparison of the two collimators available at n_TOF EAR2, represented using the geometry package of FLUKA [49]. Material key: Brown = Iron, Purple = Borated polythene, Green = Boron Carbide, Dark Blue = Iron

Neutron Fluence

One of the major benefits of EAR2 compared to EAR1 is that the much shorter flight path leads to a greatly increased instantaneous flux (since flux goes as $\frac{1}{r^2}$). Integrating this increased flux over time results in a greater neutron fluence in EAR2. Prior to the commissioning of EAR2, the expected neutron fluence was simulated by V. Vlachoudis [44], the result of these simulations, and a comparison to the known fluence in EAR1, can be found in Table 3.2. On average the fluence in EAR2 is approximately a factor of 18 greater than that of EAR1. This has huge implications as it means EAR2 is capable of performing measurements using much smaller targets, and also using radioactive isotopes with much greater activities than was previously possible. This is because a higher neutron flux leads to a much higher signal to ambient background ratio. Experiments which would have previously been dominated by the background radioactive decay of the target sample in EAR1 may now be performed in EAR2. Of particular interest is the strong increase in

of the experiment taking place.

Table 3.2: Integrated neutron fluence simulation results for EAR2, across several energy intervals, and comparison with experimental results for EAR1.

Energy Interval	EAR2 n cm^{-2} pulse^{-1}	Statistical uncertainty [%]	EAR1 n cm^{-2} pulse^{-1}	Statistical uncertainty [%]	Gain
0.02 – 10 eV	1.64e6	2.0	1.07e5	0.2	15.4
10 eV – 1 keV	1.07e6	1.4	3.98e4	0.3	26.8
1 keV – 100 keV	1.36e6	1.3	5.02e4	0.2	27.0
0.1 – 10 MeV	3.00e6	0.9	1.76e5	0.1	17.1
10 – 200 MeV	4.78e5	2.0	4.15e4	0.3	11.5
Total Range	**7.54e6**	**0.6**	**4.14e5**	**0.08**	**18.2**

neutron fluence in the eV-keV region. This energy region is of particular interest going forward for research supporting Generation-IV nuclear reactors, many of which are likely to operate at greater than thermal neutron energies. Figure 3.5 also shows graphically the difference in neutron fluence for the two areas. Note the strong dips featured in the EAR2 results, these are due to the greatly increased amount of structural material in the path of the neutron beam, particularly the large amounts of aluminium causing the large dip at the 30 keV energy region. This is material that is necessary to support and reinforce the lead spallation target [50].

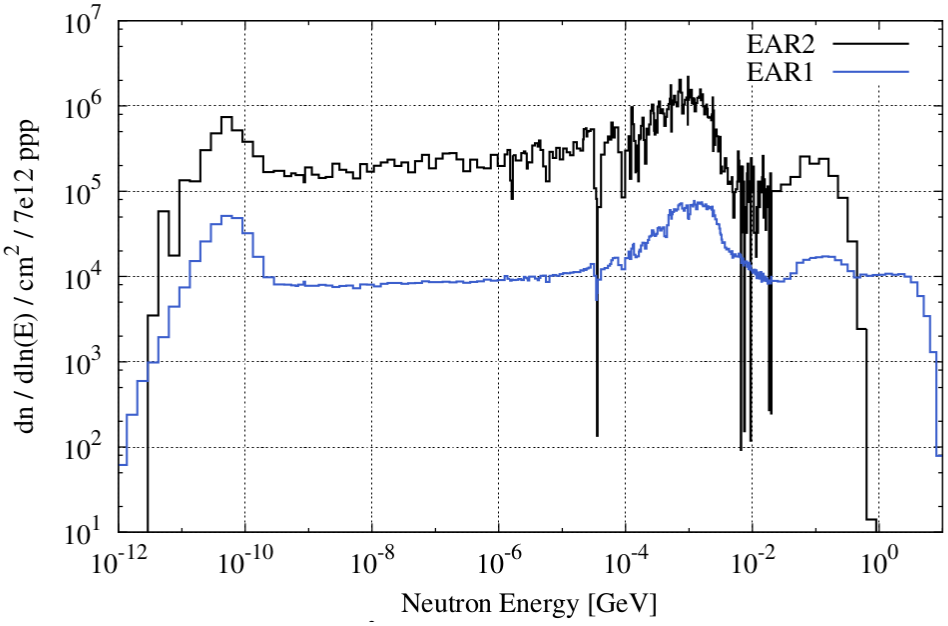

Figure 3.5: Comparison of neutron fluence per cm^2 in EAR1 (blue) and EAR2 (black) from sub-thermal energies to greater than 1 GeV, as determined by FLUKA simulations [44].

The fluence results mentioned thus far are only the results of simulations. An important part of the commissioning process for the experimental area consists of experimentally determining the neutron flux to as high an accuracy as possible. This is done by utilising so-called *standard cross-sections*, a number of isotopes for which the cross-section is already well established. These are listed in Table 3.3 along with the energy range they are used to measure [51].

Table 3.3: Standard cross sections used to determine neutron flux at n_TOF.

Reaction	Energy Range
^{1}H(n,n)	1 keV to 20 MeV
^{3}He(n,p)	0.025 eV to 50 keV
^{6}Li(n,t)	0.025 eV to 1 MeV
^{10}B(n,α)	0.025 eV to 250 keV
^{nat}C(n,n)	0.025 eV to 1.8 MeV
^{197}Au(n,γ)	0.025 eV, and 0.2 to 2.5 MeV
^{235}U(n,f)	0.025 eV, and 0.15 to 20 MeV
^{238}U(n,f)	threshold to 20 MeV

Neutron beam profile

For all n_TOF measurements it is imperative to know the spatial distribution of the neutron beam, in order to know how much of the beam is impinging upon the experiment sample. This profile is largely dependent upon the second collimator, and also varies with neutron energy (due to varying moderation paths) [52]. The expected beam profile for EAR2 was calculated mathematically and subject of FLUKA simulations prior to the development of the EAR2 facility. The results of these calculations and simulations can be seen in Figure 3.6. During commissioning of the new area one of the key measurements is the characterisation of this spatial distribution using position sensitive detectors, such as the SILI2D or XYMicroMeGas detectors [53, 54]. Early results of this analysis can be seen in Figure 3.7 [55, 56]. These results only consider the narrow collimator of EAR2. Work to characterise the beam profile with the wide collimator setup is currently ongoing.

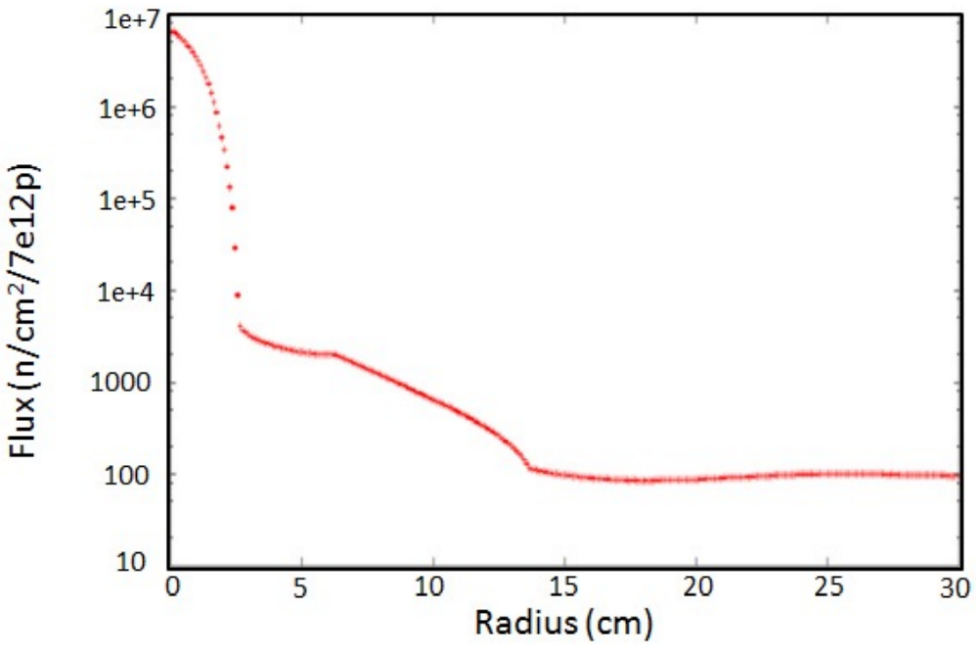

Figure 3.6: Beam profile simulated results [55].

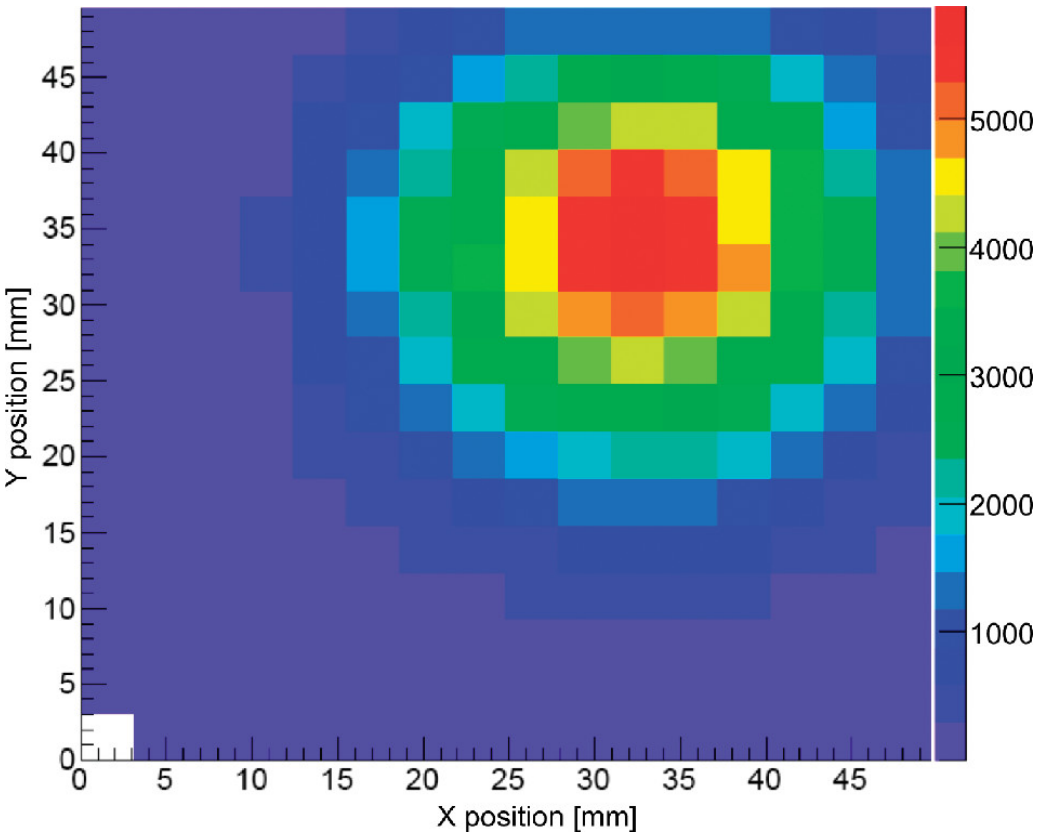

Figure 3.7: Beam profile experimental results [56].

Neutron energy resolution

The energy of a neutron induced reaction in the experimental area is calculated by measuring the time-of-flight of the neutron which has caused the reaction and dividing the distance travelled by the neutron by this time, as shown by the equation

$$E_n = \frac{1}{2} m_n \left(\frac{L}{t}\right)^2 = \alpha^2 \frac{L^2}{t^2}, \tag{3.1}$$

where m_n is the neutron mass in eV/c^2, L is the flight path length of the neutron in metres, and t is the time-of-flight of the neutron in microseconds and the resulting neutron energy, E_n is given in eV (note that this equation is only valid in the non-relativistic case, where $v \ll c$). The factor α in Equation 3.1 represents the neutron mass factor after each of the units of the equation have been appropriately converted; taking the speed of light $c = 299.8\ m\ \mu s^{-1}$ and $m_n = 939.6\ \frac{MeV}{c^2}$. This constant factor becomes $\alpha = 72.29 \frac{\sqrt{eV} \cdot \mu s}{m}$.

The time-of-flight of a neutron is calculated by comparing the timestamp of the neutron production (i.e. the moment the proton pulse impinges upon the spallation target) with the timestamp of the resulting experimental reaction (i.e. the timestamp of the signal within the appropriate detector). There is, however, an intrinsic resolution for the resulting neutron energy based on an amalgamation of underlying resolutions of this process. The time-of-flight resolution depends upon the width of the proton pulse (7 ns RMS [57]) and the time resolution of the detectors measuring the impingement time and detection time. The flight path length depends upon moderation paths taken by neutrons as they leave the target and interact within the water moderation layer surrounding the target. This contribution to resonance broadening effects is known as the *Resolution Function* [58]. The overall broadening of measured resonances combines this resolution function with a contribution from the thermal motion of the nuclei in question (i.e. Doppler broadening) and the width of the proton pulse.

This resolution function is determined via simulation (example results shown in Figure 3.8) and then subsequently confirmed via comparison to experimental results. Experi-

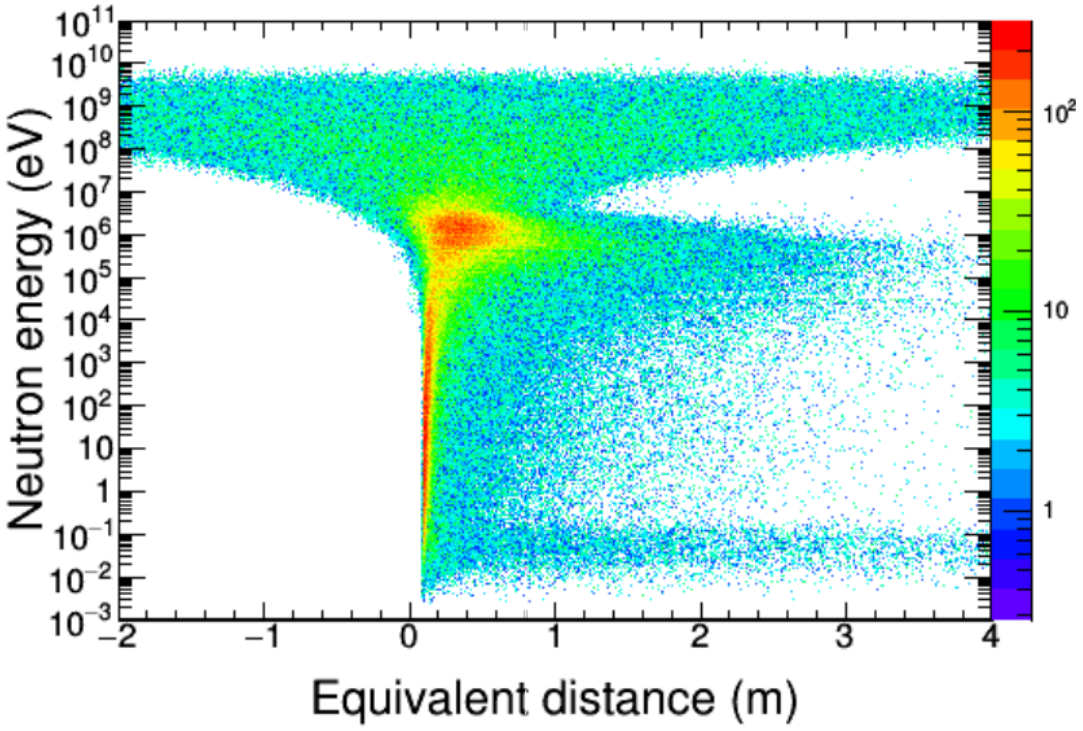

Figure 3.8: Probability distribution of the equivalent moderation distance, as a function of neutron energy, obtained from GEANT4 simulations of the n_TOF spallation target. The negative values at high neutron energies are caused by the convolution of the results of the simulations with the width of the incoming proton pulse [59].

mental confirmation requires using a sample of an isotope which has a sufficiently distinct resonance (i.e. well separated from nearby resonances) at a sufficiently high energy such that the Doppler broadening effect due to thermal motion no longer dominates the resolution of the measurement. At n_TOF, numerous samples are used to aid in determining the resolution function. One such sample is ^{56}Fe, as this has suitable capture resonances, for example at an energy of approximately 81 keV (as shown in Figure 3.9).

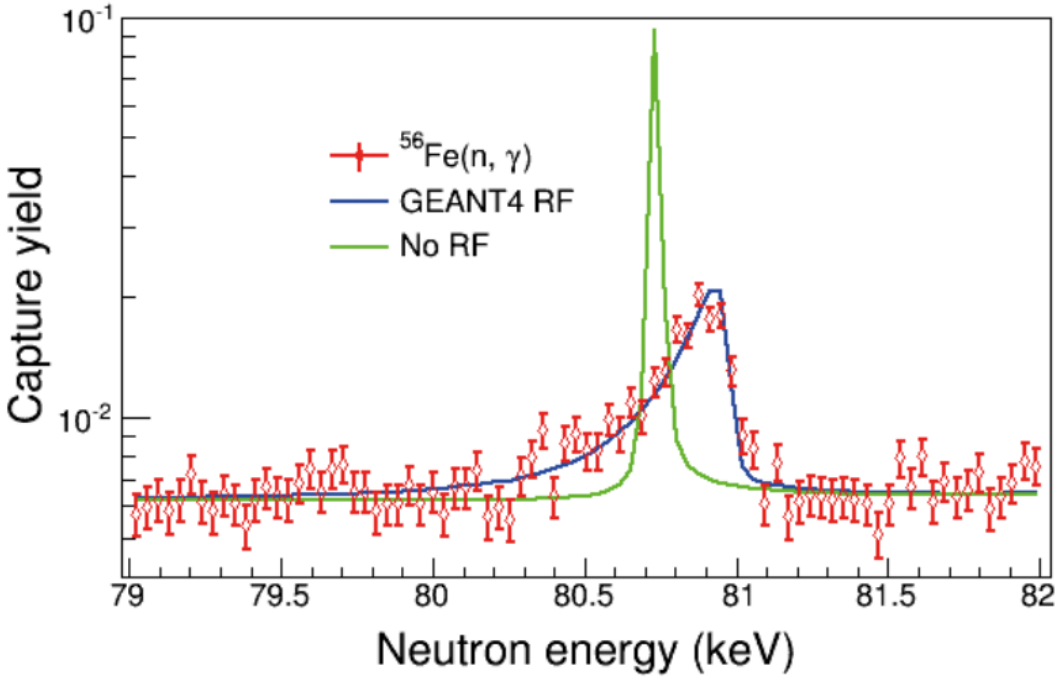

Figure 3.9: A comparison between a measured resonance of the capture cross-section in ^{56}Fe, and a simulated resonance both with and without the resolution function [59].

The "γ flash"

The proton spallation reaction not only creates neutrons, but also creates unwanted by-products. These by-products consist primarily of γ rays, along with other short-lived particles such as pions. These by-products may travel along the experimental beamline and reach the experimental hall where they will increase the background count rates within any detectors and have the potential to overwhelm detectors, rendering them unusable for a sustained length of time. The sweeping magnet within the beamline attempts to mitigate this by removing charged particles travelling through it; however, the magnet has no effect on neutral particles. There is also the possiblity for further unwanted particles to be created in the portion of the beamline after the sweeping magnet (for instance through collisions with the beam collimator, or with vacuum windows etc.). This prompt radiation is referred to as the "γ flash", named so because the major component is γ rays. The type of detector within STEFF which exhibits the most dramatic response to the γ flash is the NaI(Tl) scintillation detector which, as a large γ-ray detector, is to be expected. An example of

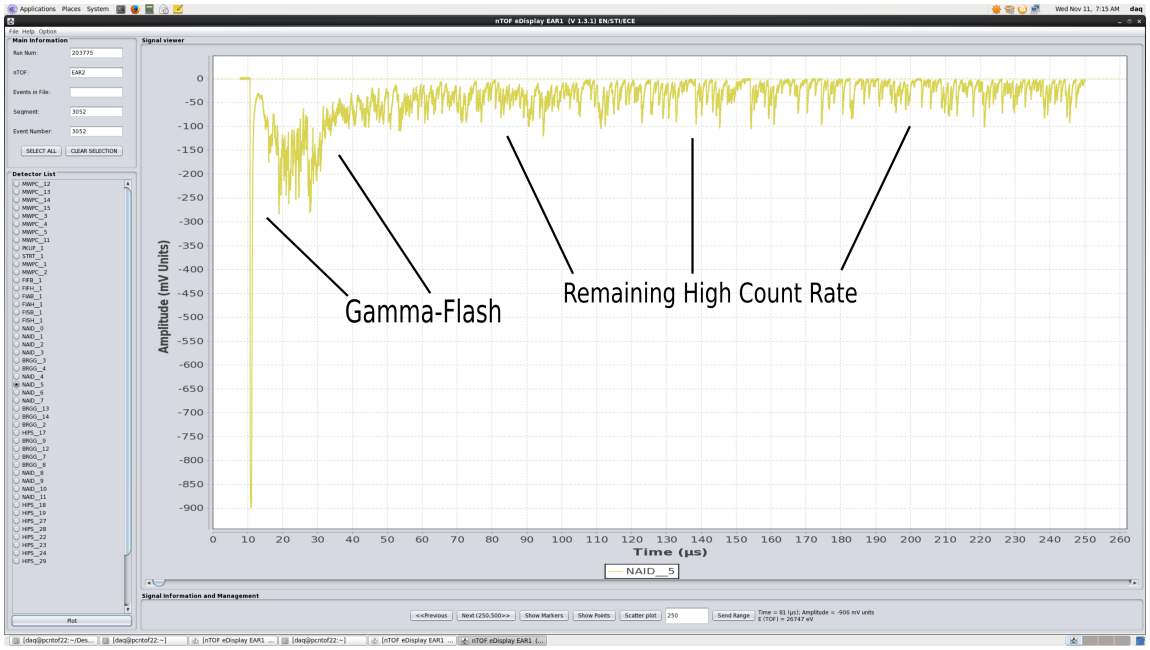

Figure 3.10: The response of a NaI(Tl) detector to the γ flash for the narrow collimator setup in EAR2, during phase one of the experimental campaign.

how a NaI(Tl) detector is blinded can be seen in Figure 3.10. The detector experiences a huge signal response that only begins to fully decay away after around 50 μs, though even after that time a very high count rate still remains. A thorough investigation has been performed in order to try and characterise the effect of the γ flash on each of the various types of detector, confirming that the primarily affected detector is the NaI(Tl) [60]. This work was performed only on the narrow collimator setup in EAR2. Moving to a wide collimator setup has a large effect on the γ flash and greatly increases the effects seen in the detectors.

Figure 3.11 shows the energy spectra of the γ-ray background present in the experimental hall of EAR2. The results are broken down into *Prompt* γ (ToF$\leq$ 200 ns) and *Delayed* γ (ToF $>$ 200 ns, typically up to around ToF $\sim$ 5 ms). The prompt γ rays identified here are the primary contributors to the γ flash [48]. As shown, the energies of the photons within the γ flash can extend up to the order of several hundred MeV, however the dominant region is below 10 MeV.

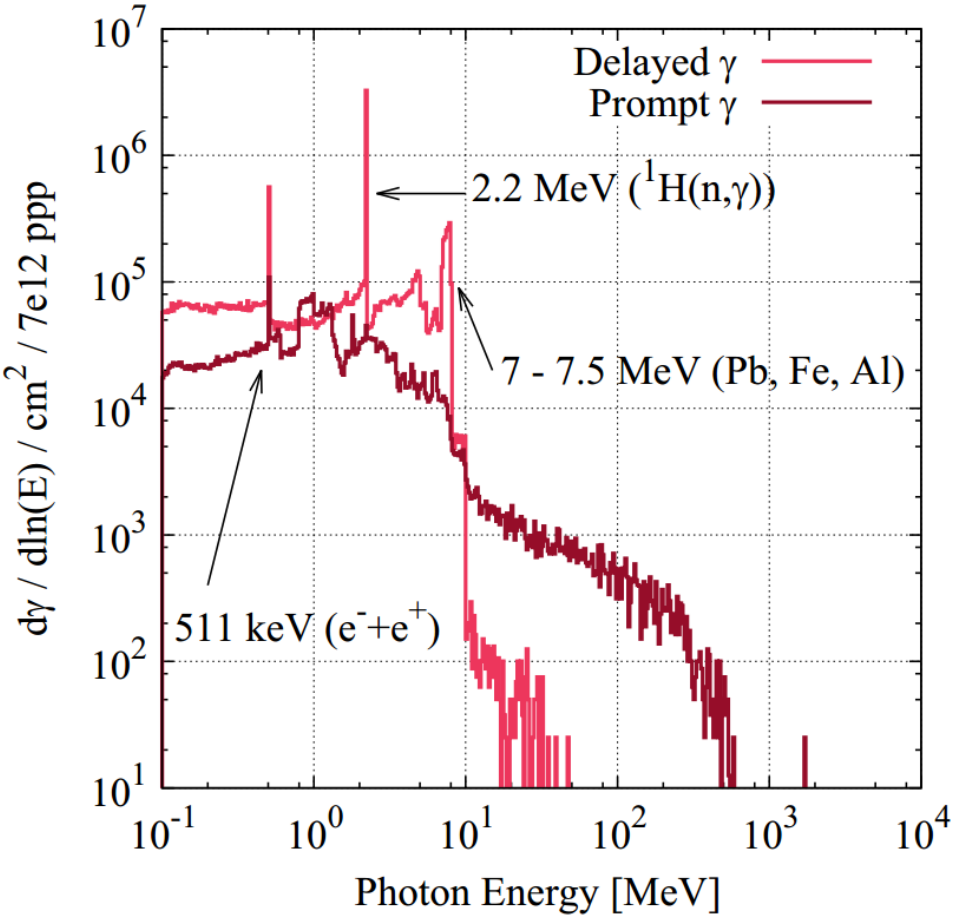

Figure 3.11: Photon energy spectra in EAR2, categorised as prompt or delayed photons [48].

3.1.2 The Data Acquisition System (DAQ)

The large instantaneous neutron flux at n_TOF requires a data acquisition system (DAQ) which is capable of reading data at a very fast rate, transfering the data to memory and having minimal dead-time [61]. The n_TOF DAQ utilises high performance flash-ADC digitizers to directly digitize and store raw data signals, which allows dedicated off-line analysis to be carried out along with numerous software processing techniques to mitigate problems with the raw data. This, however, does result in large amounts of data which need to be stored and transferred at a high rate. At the time of the experiment described in Chapter 7 the n_TOF DAQ utilised 120 data channels spread across 24 data cards, these cards are split between EAR1 and EAR2.

The DAQ is triggered to commence data reading by receipt of a signal created approximately 10 μs before the proton pulse impinges upon the n_TOF lead target. This opens a time window (the length of which the user may define) during which the DAQ takes data. Each data card may be customised individually, adjusting the length of this time window and also the sampling rate at which the data is taken (from approximately 100 MHz to 1.8 GHz). There exists within the DAQ the ability to reduce the amount of non-valuable data being taken by a "zero-suppression" algorithm. This enables users to set a signal threshold and only signals above this threshold are stored. These non-suppressed raw data signals and important experimental information (date, run number, sampling rate etc.) are gathered in a binary format then formatted into a data buffer and subsequently grouped into data streams (a data stream typically consists of four data buffers). The digitized data streams are then stored on a temporary disk before being uploaded to a central database known as the Cern Advanced STORage manager (CASTOR) [62]. At CASTOR these data are stored on disk and on tape, where they can be accessed at a later date as needed for analysis. The team at the n_TOF facility have produced routines which allow the conversion of these raw data traces and experimental information into ROOT [63] file outputs containing the requisite information in a list-style format. This is achieved via pulse shape analysis of the raw traces [64].

4

The SpecTrometer for Exotic Fission Fragments (STEFF)

The SpecTrometer for Exotic Fission Fragments (STEFF) is a 2-velocity, 2-energy (2v2E) apparatus designed to detect fission fragments and, in coincidence, aims to perform prompt (i.e. sub-microsecond) γ-ray spectroscopy of the fragments. A detailed schematic of STEFF can be seen in Figure 4.1, where it can be seen that STEFF consists of a central, spherical chamber surrounded by an array of scintillation detectors, with four fission fragment detector arms protruding from this central section. The arms detect the velocities and energies of fission fragments and utilise these values to calculate fission fragment masses and obtain fragment mass yields. This calculation is simply a rearrangement of the equation for kinetic energy,

$$m = \frac{2E}{v^2} \tag{4.1}$$

The STEFF detector is actually a collection of many smaller detectors all working in unison to measure and characterise properties of fission fragments and the nuclear fission process. These smaller detectors can be grouped into three major categories, complimenting and combining to investigate the whole fission process; these three categories are:

- Timing detectors - used to determine the velocity of detected fission fragments, and to accurately determine the time at which a fission event occurs. These detectors are situated on the fission fragment arms.

- Ion chambers - used to determine the energy of detected fission fragments. These detectors are situated on the fission fragment arms.

- γ-ray scintillators - used to detect γ-ray energies and multiplicities. These detectors are surrounding the STEFF central chamber.

For more information on the performance of these specific detectors, see [9–11].

Naming Convention

In order to maintain clarity throughout the rest of the document, the following names will be used to refer to specific fission fragment arms of the STEFF detector:

- *BRGG arm* - The BRGG arm is the fission fragment arm which features the start detector at its entrance aperture.

- *HIPS arm* - The HIPS arm is the opposite arm to the BRGG arm along the horizontal axis. This is so-named due to the ion chamber within this arm previously featuring in the HIPS (Heavy Ion Particle Spectrometer) experimental setup.

- *FiFI BRGG arm* - The FiFI BRGG arm is the off-axis fission fragment arm on the side of the BRGG arm.

- *FiFI HIPS arm* - The FiFI HIPS arm is the off-axis fission fragment arm on the side of the HIPS arm.

4.1 Upgrades to the STEFF Spectrometer

Before continuing it is important to note that between this run and those previous, the STEFF spectrometer has undergone a series of upgrades in order to improve its capacity for the measurement of nuclear data in experiments such as that outlined within this thesis. The most significant of which are briefly outlined here:

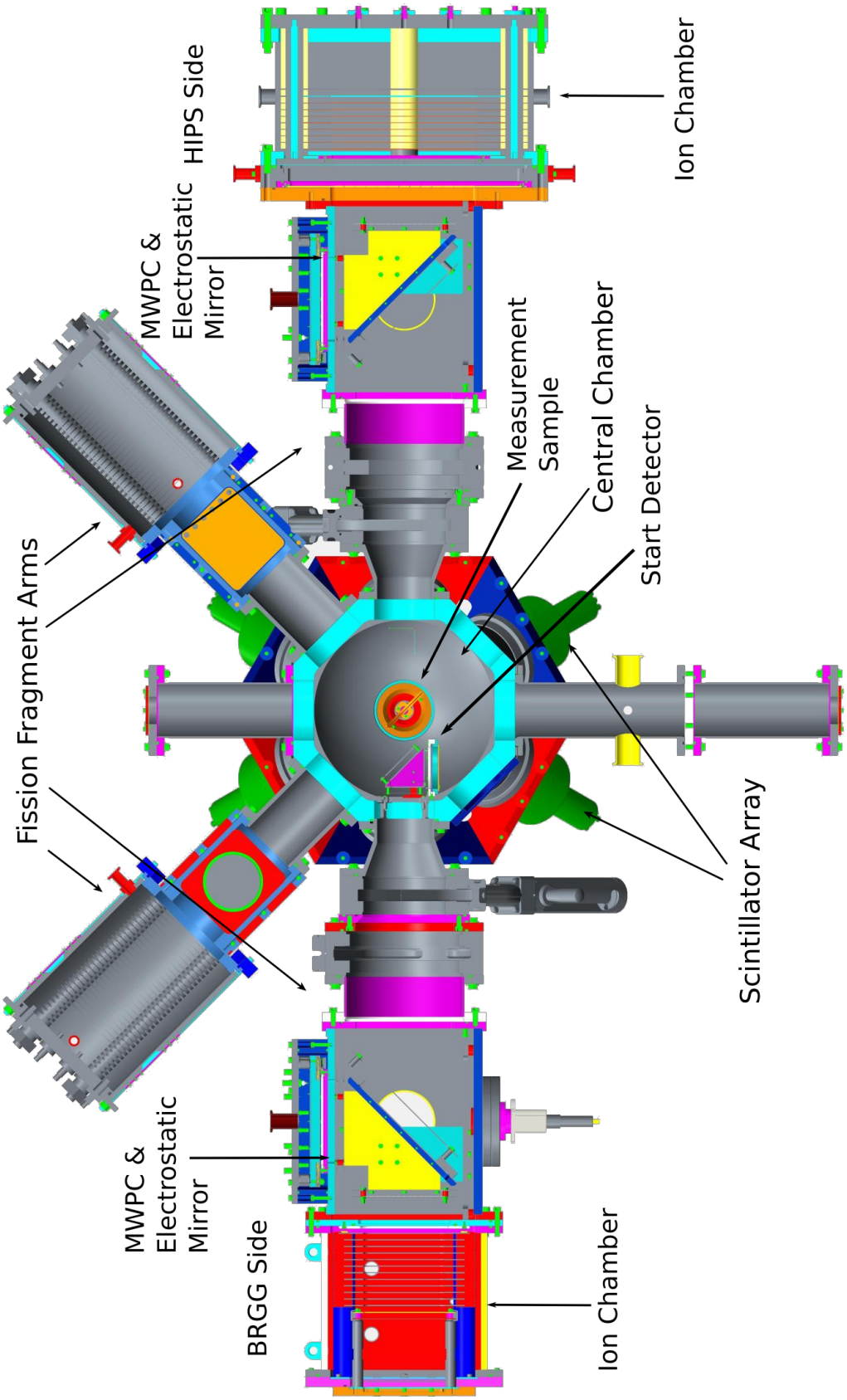

Figure 4.1: A detailed, false-colour schematic of the SpecTrometer for Exotic Fission Fragments (STEFF), with several sections highlighted.

- *Extra fission fragment detection arms.* In order to improve the geometric efficiency of STEFF, two additional arms have been added to the central chamber. These additional arms can be seen in Figure 4.1, they are the arms mutually angled 45 degrees both to the main and vertical axes of STEFF. The addition of these arms increases the solid angle covered by fission fragment detectors from 60 milli-steradians to 134 milli-steradians. These detectors are referred to as "FiFI arms", short for "Fission Fragment Identifier arms".

- *Sodium iodide scintillator upgrades.* Adjustments to the electronics of the NaI(Tl) detectors have been made in order to improve the detector performances in a high photon flux environment; these adjustments are explained in greater detail in section 4.4, and the results of the modifications outlined in Chapter 6.

- *Stop detector improvements.* The stop detectors (described further below) have been subject to extensive testing and development in order to improve their efficiency; and the overall detection efficiency of fission fragments within STEFF. Owing to the fact that both stop detectors must trigger in conjunction to provide a full description of any fission event, any inefficiency of the stop detectors is multiplied two-fold. So improvements to these detectors will have a large end-result on the overall efficiency [65].

4.2 Timing Detectors

As can be seen from Equation 4.1, an accurate determination of fission fragment mass relies heavily upon accurate measurements of fission fragment velocities. Therefore, ensuring that the timing measurements are as precise as possible is crucial to minimising the uncertainties for the masses of fission fragments measured by STEFF. To this purpose STEFF has a collection of dedicated timing detectors designed to measure fission fragments in several key locations within the STEFF system. These detectors can be nominally divided into two sub-classes, "Start" and "Stop" detectors, whose locations and

functions are explained in detail below.

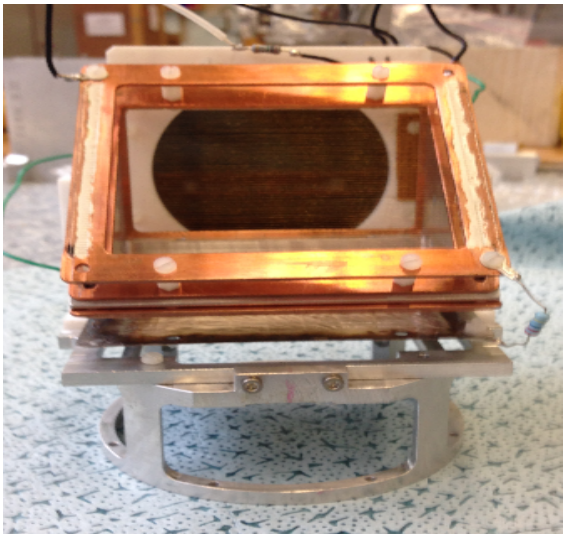

(a) A photograph of the STEFF start detector. This is a top down view, therefore the fission source would be above the picture, the BRGG detector arm below and the MCP is at the rear of the STRT detector.

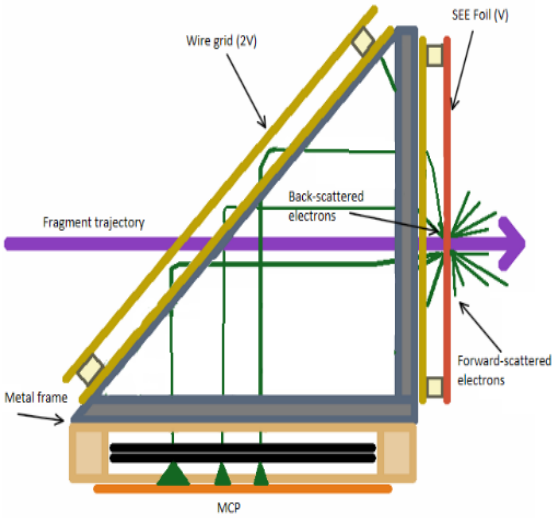

(b) A diagram of the STEFF start detector demonstrating electron creation and detection.

Figure 4.2: STRT detector components and diagram [65].

4.2.1 Start Detectors - Micro-Channel Plates

In previous runs there was a single STEFF start detector inside the central chamber located approximately 15 cm from the experimental target, aligned along the horizontal axis of STEFF. However, as part of the recent augmentation of STEFF (section 4.1), the addition of two extra fission fragment arms has brought the total number of start detectors to three. The original start detector located adjacent to the experimental target, designed to trigger on fission fragments entering the main arm of STEFF, and one start detector in each of the FiFI arms to trigger on fission fragments entering these arms. These detectors feature three main components: an electron source (an electron emitting foil), an electron guide and accelerator (an electrostatic mirror) and an amplifier/detector combination (a very fast Micro Channel Plate (MCP) detector) [9–11, 65].

A photograph of the main arm start detector can be seen in Figure 4.2a, and a diagram

demonstrating how these detectors operate is shown in Figure 4.2b [65]. The purple arrow shows a fission fragment passing through the detector; this will interact with the electron emitting foil, liberating electrons from the foil surface in all directions. The foil maintains a negative voltage ($-V$) which accelerates electrons away from the surface. The back-scattered electrons are accelerated towards a wire grid held at a higher magnitude negative voltage ($-2V$). The subsequent electric potential generated by the foil and wire grid decelerates the electrons and redirects them towards a micro-channel plate detector where a signal can be collected and amplified. The process of generating, accelerating and detecting these electrons occurs of several nanoseconds, which enables very good time resolution from such detectors. One minor disadvantage of this detector is that the foil may spontaneously eject electrons at a low, but non-negligible rate. These spontaneously emitted electrons may then form spurious detector signals which must be dealt with during analysis. For further information on micro-channel plate detectors, see [66].

4.2.2 Stop Detectors - PPACs & Multi-Wire Proportional Chambers

Within the main arms there exist stop detectors, one in each arm; the FiFI arms lack the required space to accommodate a stop detector and thus they are not present therein. These stop detectors provide a second time stamp for each fission fragment, enabling a speed measurement for each. These detectors are slightly more complex than the start detectors, but they similarly contain a foil-mirror system (albeit much larger, see Figure 4.3a). Instead of detection via a system of micro-channel plates, however, the electrons from this foil are accelerated vertically by the electrostatic mirror into a gaseous detector. Similarly to the start detector these detectors also suffer from spontaneous electron emission at a non-negligible rate. For phase one of the experimental campaign these gas detectors were Parallel Plate Avalanche Counters (PPACs) and for phase two they were replaced with Multi-Wire Proportional Chambers (MWPCs). Figure 4.3 shows an example of the combination of electrostatic mirror and gaseous detector used for these detectors. The gas in these detectors is high-purity isobutane ($\geq 99\%$ iC_4H_{10}), held at approximately 10 mbar of

pressure. Accelerated electrons enter the gaseous medium with high energy and proceed to create further electron-ion pairs within the gas. These electron-ion pairs will then drift towards the detector anode (be it a plate within a PPAC or a system of wires held taut across the top of the detector region in an MWPC), creating a signal which is then propagated through a pre-amplifier to register as a detectable signal. For more detailed information on the physics of Parallel Plate Avalanche Counters see Coffin and Engelstein [67] and for Multi-Wire Proportional Chambers, see [68].

4.3 Ion Chambers

At the end of each detector arm is a large, gaseous, ionisation chamber. The total solid angle coverage of these large detectors is 134 mSr (30 mSr in each of the main arms and 37 mSr in each FiFI arm). Each fission event usually emits two fragments in opposite directions, meaning that the solid angle efficiency of the FiFI arms is increased by a factor of two (this does not apply for the main arms as these are on the same axis as one another); this results in a geometric efficiency of approximately 2% across the four ion chambers. The gas in question is also the high-purity isobutane used within the MWPC detectors, although held at a higher pressure in order to stop the fission fragments, which have a greater energy and range than the electrons encountered within the MWPC detectors. There are four ion chambers in all, one at the end of each arm, and the pressures these are held are split two-fold: the BRGG arm ion chamber is held at 70 mbar of pressure whilst the HIPS arm ion chamber is held at 100 mbar of pressure. This is because the HIPS ion chamber does not have the same depth and thus must reduce the fission fragment range within the detector as full characterisation of the fragment requires the whole of its energy to be deposited within the gaseous medium. Both the FiFI BRGG and the FiFI HIPS arms are also held at 100 mbar of pressure, though this is due to the setup of the gas and vacuum systems within STEFF rather than a choice based on any physics requirements (see Section 4.5).

These chambers are designed to stop any fission fragment within the gaseous medium.

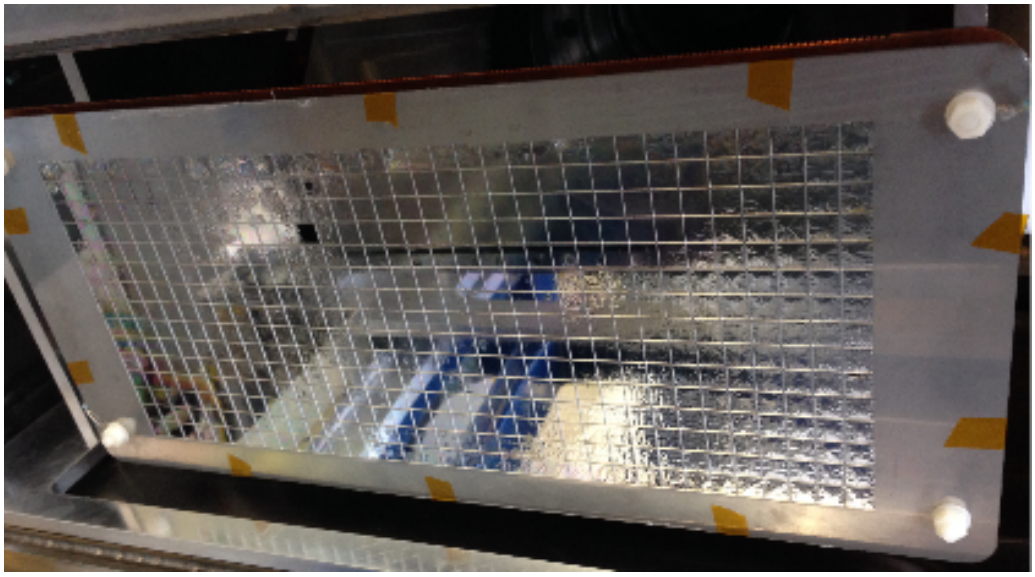

(a) A photograph of the electron emitting foil of the STOP detector.

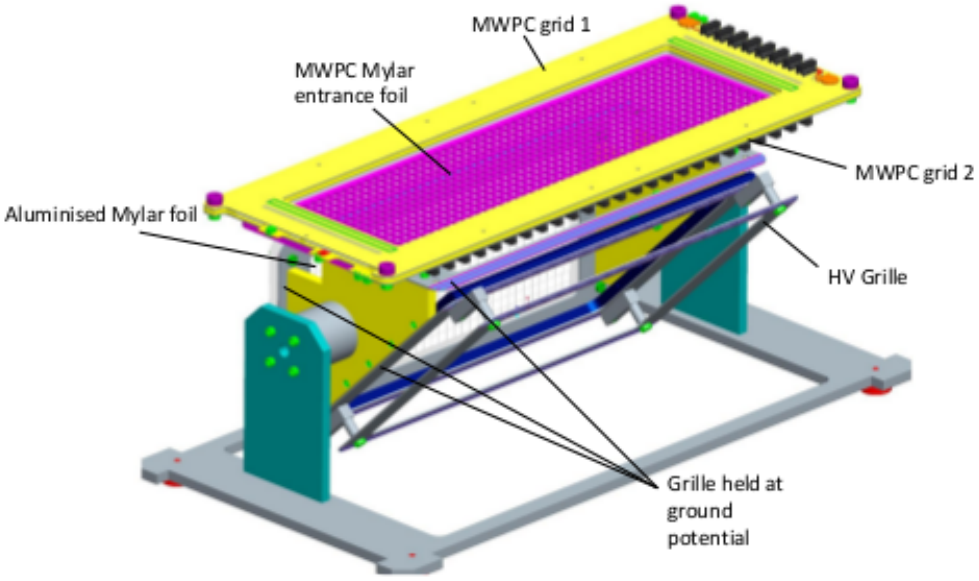

(b) A diagram of the STOP start detector, featuring electron foil, electrostatic mirror, and the Multi-Wire Proportional Chamber system [9].

Figure 4.3: STOP detector components and diagram.

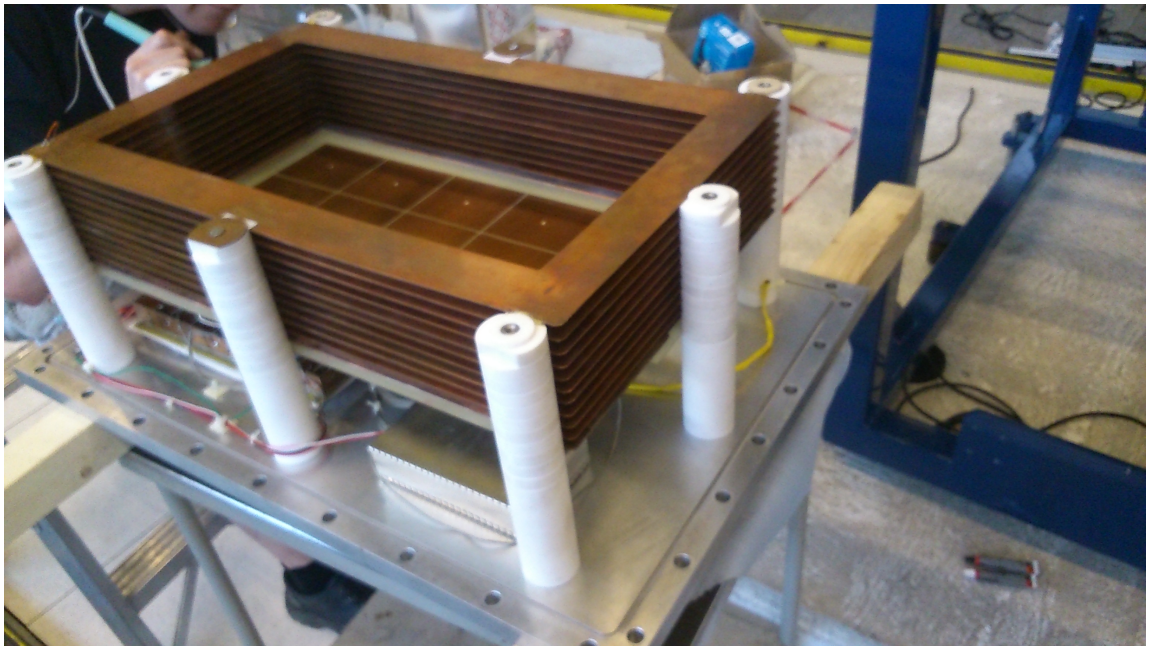

Figure 4.4: An internal view of the BRGG arm ion chamber. The field shaping rings are clearly visible being supported by plastic arms, several of the detector anodes can be seen along the rear wall of the chamber.

The fission fragment charge, Z, and the fission fragment energy, E, can be determined by analysing the total fragment energy loss and the rate of energy loss per unit path length, as described previously in [9], [10], and [65]. Using this in conjunction with the velocity measured by the previously described timing detectors means equation 4.1 can be used to obtain a value for the mass of the fission fragment.

As the fission fragment passes through the gaseous medium within the ion chamber electrons are liberated from the gas molecules. A large positive potential (c. +1 KV) accelerates the liberated electrons. The accelerated electrons pass through a Frisch grid and are subsequently collected by detectors anodes on the rear wall of the ion chamber. This produces a signal which may be detected. Figure 4.4 shows the inside of the BRGG arm ion chamber, within which can be seen numerous metal bands. These are the 'Field Shaping Rings' which, using a voltage divider chain, distribute the aforementioned potential linearly within the detector region leading up to the Frisch grid and anode regions of the ion chamber. These help to homogenise and stabilise the electromagnetic field within the ion chamber and preserves the shape features of the resulting signal [65, 69].

4.4 γ-Ray Detector Array

Surrounding the central chamber of STEFF is an array of γ-ray scintillation detectors composed of two rings of six detectors. Each ring is angled $\pm 45^{\circ}$ to the horizontal plane and each detector is spaced out equally around the ring in 60° intervals. In phase one of the STEFF experimental campaign (section 7.1) this array consisted of twelve NaI(Tl) (*sodium iodide*) detectors; whereas in phase two (section 7.2) one of the NaI(Tl) scintillators was swapped for a $LaBr_3$ (*Lanthanum Bromide*) detector in order to improve the performance of the array at higher count rates (due to its faster response and smaller size the $LaBr_3$ is capable of surviving γ-ray background rates which the NaI(Tl) cannot). Figure 4.5 shows a single NaI(Tl) detector undergoing a calibration measurement, and Figure 4.6 shows the set-up of the array surrounding STEFF during the experiment. These are large detectors, 127 mm in diameter and 102 mm in height, designed to maximise the efficiency of detecting any prompt γ rays produced. The active surface of each detector is situated approximately 200 mm from the centre of the target chamber of STEFF, this results in a geometric efficiency of $30\% \pm 2\%$ in campaign phase one. The $LaBr_3$ detector however is a smaller, cuboidal detector with an active area of 50.8 mm square; the replacing of a single NaI(Tl) with this $LaBr_3$ results in a geometric efficiency of $28\% \pm 2\%$ for campaign phase two. These NaI(Tl) scintillators are very commonly used detectors in the field of nuclear physics and especially γ-ray spectroscopy. In this experimental campaign they have been used to detect the prompt γ rays emitted from the fission of the uranium targets. Modern experiments have begun to utilise lanthanum halide detectors, such as $LaBr_3$, to enable faster response measurements of γ ray emissions.

In order to minimise background detections due to Compton scattering between detectors, each of these detectors is surrounded by a 6 mm thick tungsten cylinder, known as a 'Compton suppressor'. Despite efforts to minimise the γ-ray background as much as possible there still exists a very large background rate present within the NaI(Tl) detectors. Fortunately the use of coincidence techniques means the majority of this background can

be easily disregarded. This coincidence technique consists of identifying where STEFF has detected a fission fragment, and then applying an appropriate time gate to only retain information for γ rays which may have resulted from the fission process. This technique is discussed in further detail, along with how it was applied within the analysis routines, within Sections 8.1 & 8.2 in Chapter 8.

4.4.1 Scintillation Detection

As mentioned previously, NaI(Tl) detectors are scintillation detectors; when a γ ray enters a scintillation crystal the photons interact with the detector medium via three main routes: *Compton scattering*, *pair production*, and *photoelectric absorption*. These interactions excite electrons within the crystal lattice, with energies dependent upon the energy of the incoming γ ray. Excited electrons propagate through the crystal, imparting their energy to the lattice electrons which proceed to later de-excite subsequently emitting visible photons. The energy of these visible photons is shifted compared to the incoming energy, due to the scintillation crystal being doped (in the case of NaI(Tl) detectors this doping agent is thallium). This energy shift allows the photons to travel further through the crystal unimpeded. Eventually these visible photons reach a photocathode at the rear of the scintillation crystal, which serves as the divide between that and the photomultiplier tube (PMT). The photons incident on the photocathode produce multiple electrons, then through a series of dynode chains (held at progressively higher magnitude of electropotential) these electrons multiply through the PMT until they reach an anode at the end of the PMT and produce a detector signal [10, 70, 71]. The "decay constant" (i.e. the typical time taken for excited electrons within the scintillation crystal to emit fluorescent light) for a NaI(Tl) scintillator is 0.23 μs, making these quite slow scintillators (other detectors can achieve decay constants as low as the nanosecond timescale) [72]. Further information on scintillation detectors, photomultiplier tubes and NaI(Tl) detectors specifically can be found in Knoll [72].

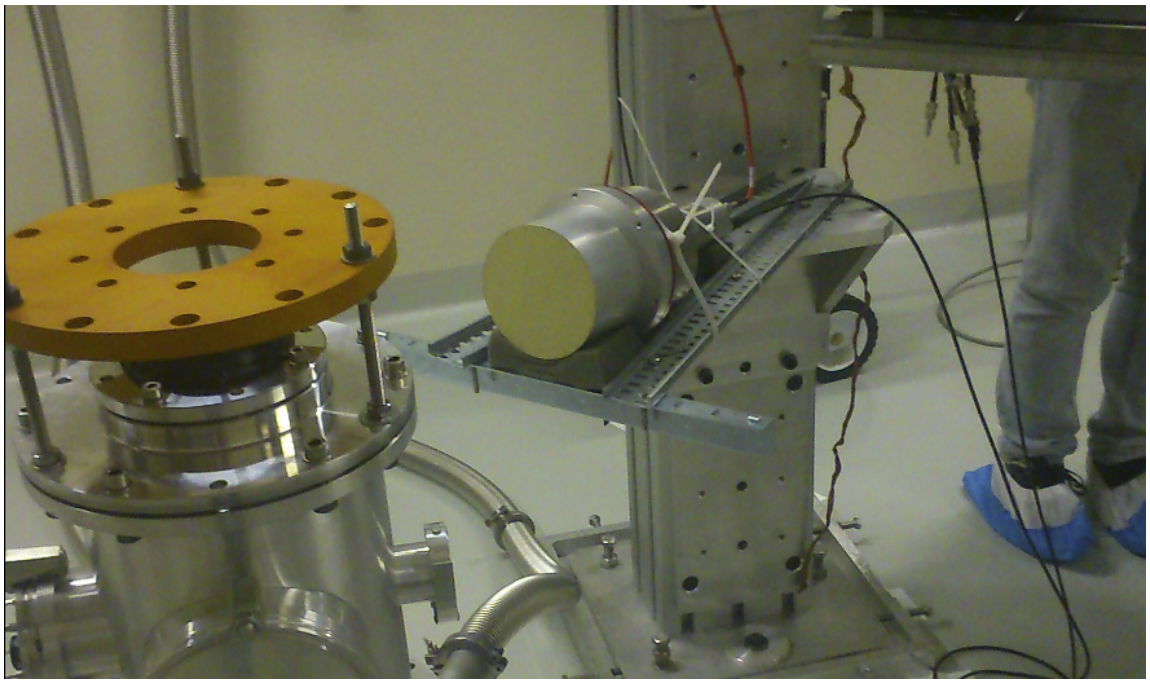

Figure 4.5: One of the NaI(Tl) scintillation detectors undergoing testing and calibration.

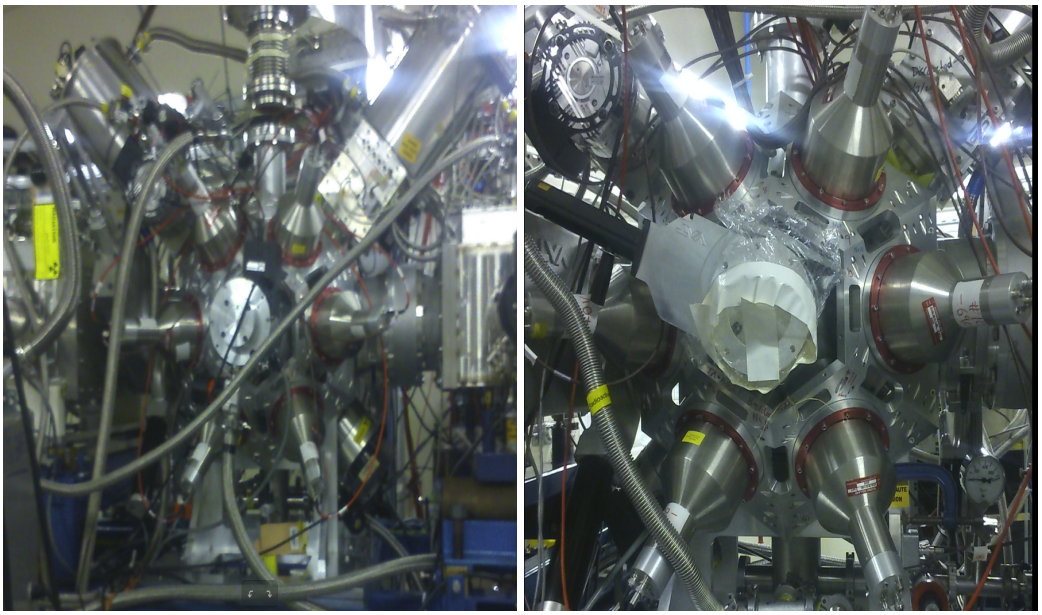

(a) East wall side. (b) West wall side.

Figure 4.6: (a) The east-wall side of the STEFF experiment NaI(Tl) array. The single $LaBr_3$ detector used in phase two of the experimental campaign would be present in the top-right of the array here, however it was not introduced until after this picture was taken. (b) The west-wall side of the STEFF experiment NaI(Tl) array.

4.4.2 NaI Modifications

These detectors have been used in previous measurements with STEFF, including a similar measurement on ^{235}U at the Institute Langue-Levin in Grenoble [9], in which the experimental conditions were largely different from those at n_TOF. Until this experimental campaign these detectors had never been used in a high count-rate environment; instead being used at the end of a beamline coming from a thermal flux research reactor, where the γ count rates and background rates were substantially lower. To aid their performance in preparation for this experiment the sodium iodide detectors have undergone modifications to improve their response to the high rate environment of n_TOF EAR2, the details of these modifications and the results of testing them can be found Chapter 6.

4.5 Gas & Vacuum Systems

Different regions within the STEFF spectrometer require different pressures in order for STEFF to operate effectively. Sections 4.3 and 4.2 mentioned the fact that the gas within the ionisation chambers is held at either 70 mbar or 100 mbar and within the multi-wire proportional chamber it is at a pressure of 10 mbar. In addition to these pressure requirements it is vital that the central chamber of STEFF and the chambers holding the large electrostatic mirrors are kept at a high vacuum. In order that any detected fission fragments maintain as much as possible of their original, released energy (and so that the large electrostatic mirrors do not spontaneously discharge, or 'spark'), these regions must be maintained to the order of 10^{-6} mbar or below. This is achieved through six turbo-molecular vacuum pumps on the central chamber and surrounding arms (two on the central chamber, one on each electrostatic mirror chamber and one on each FiFI arm).

Separating these gas-filled detector regions from the low vacuum regions is achieved by using six 0.9 micron thick aluminized mylar windows (a mylar polymer with a thin deposited layer of aluminium) supported by a steel mesh frame.

The gas within the gaseous detectors of STEFF does not sit idle but requires continuous

circulation and feedthrough. This is because the detection of fission fragments (or electrons, as is the case of the MWPC detectors) ionises the gaseous medium, which affects the chemical properties of the gas and results in significantly poorer detector performance if left uncorrected, as much as 1% signal degradation per hour of un-refreshed gas [73].

Prior to filling the various STEFF regions with gas the system must be fully evacuated and held at vacuum for a prolonged period of time (typically at least the order of days), this is to remove all traces of gas and moisture within the detector in order to minimise impurities whilst the system is running. It requires a prolonged duration due to the outgassing of the various materials throughout STEFF (i.e. the releasing of gas previously contained within the material structure) – in particular the large structures supporting the electrostatic mirrors retain a lot of gas within the plastic from which they are made. It is these plastic structures which cause the majority of the outgassing. The continuous gas flow is achieved by the use of several baratrons to control the gas supply and exhaust rates (Figure 4.8), all the while being carefully monitored through an assortment of vacuum gauges/controllers (Figure 4.9). This results in quite a complex gas control and distribution set up (Figure 4.7) to ensure gas flows or does not flow to each volume within STEFF as is required.

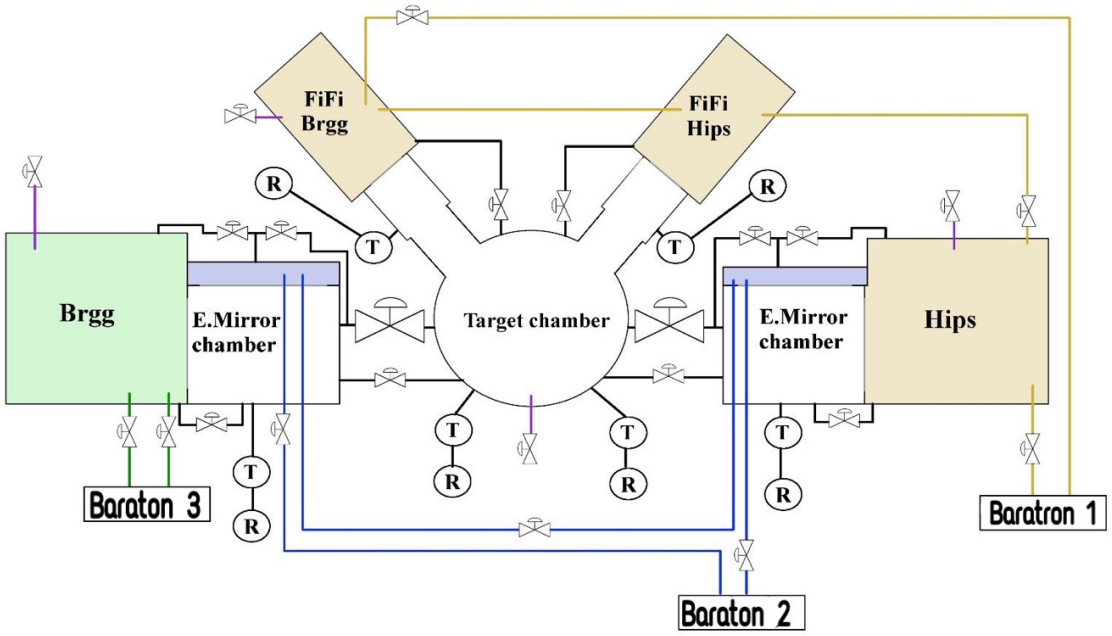

Figure 4.7: Diagram of gas flow routes and controllers surrounding STEFF. The gas flow can be considered in three distinct regions: Baratron 1) 70 mbar isobutane flowing through the HIPS ionisation chamber and the two FiFI arms, Baratron 2) 10 mbar isobutane flowing through the MWPC detectors, and Baratron 3) 100 mbar isobutane flowing through the Bragg arm ionisation chamber. Also present on this diagram are the turbo-molecular vacuum pumps (T) and rotary vacuum pumps (R).

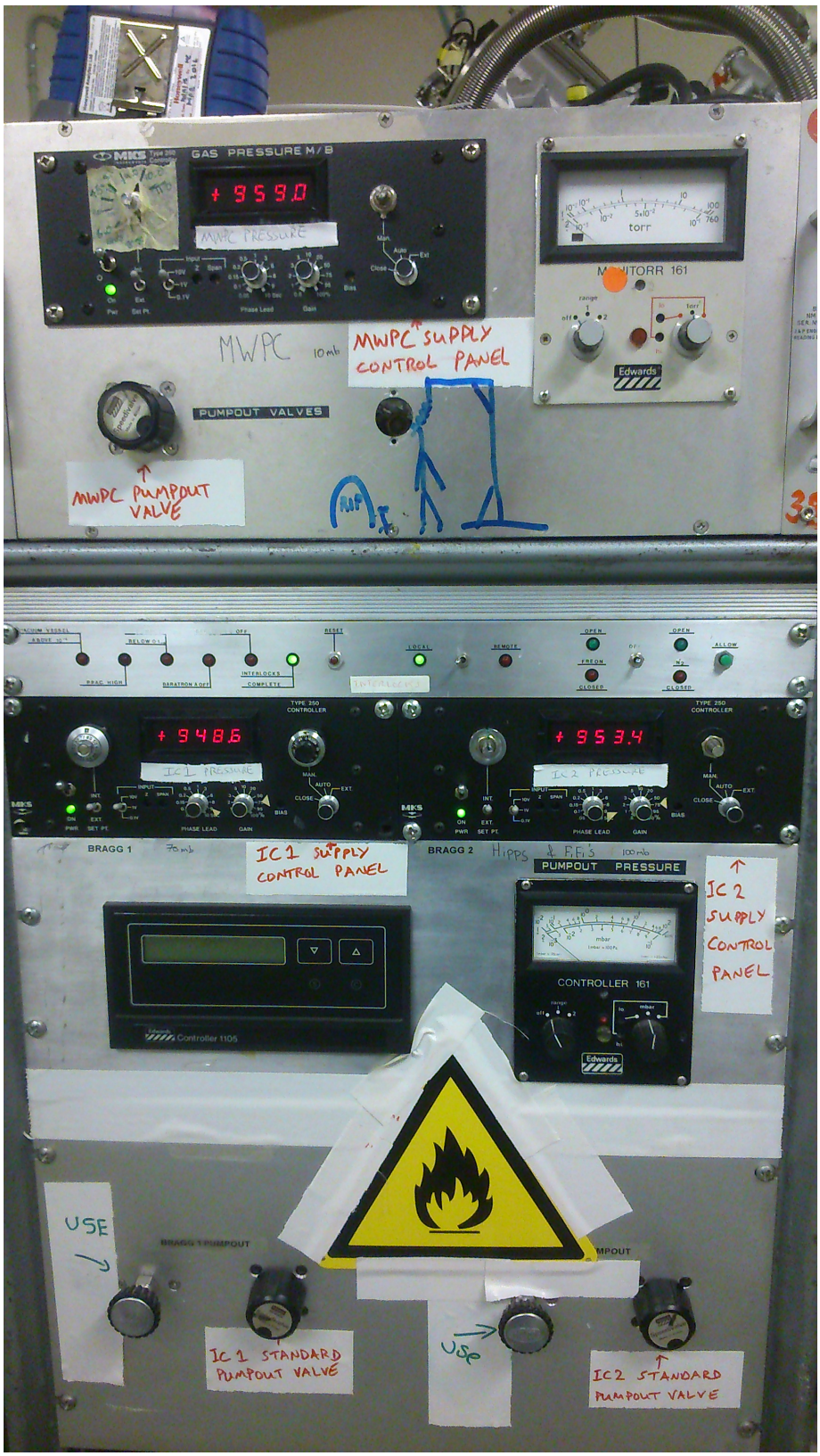

Figure 4.8: Three baratrons connected to STEFF to allow independent control of the flow of isobutane to the Bragg Arm, HIPS Arm and MWPC regions.

Figure 4.9: The vacuum gauge and controller cabinet to maintain and monitor the high vacuum environments within the STEFF detector, along with the non-vacuum gas detector regions.

5

Simulations - NaIs in EAR2

Prior to this experiment STEFF has never been used in a spallation source experimental facility, therefore simulation work has been performed in order to understand how the STEFF spectrometer will behave in the n_TOF EAR2 experimental hall. The aim primarily being to investigate the nature of the background rate that the NaI(Tl) scintillation array may be subjected to, and try to mitigate any potential issues foreseen there. The process and major results of this simulation work will be detailed within this chapter.

5.1 Monte Carlo Simulations

The simulation work and results discussed within this chapter have utilised the Monte Carlo method of simulations. A Monte Carlo simulation involves tracking a particle and determining the interactions of this particle through the use of random number generation and appropriate probability density functions. Repeating this process many times (a single Monte Carlo simulation may repeat this for many millions of starting particles) allows the simulation to determine macroscopic effects from microscopic properties.

The Monte Carlo method, as it applies to neutron transport models such as the ones discussed in this chapter, begins with the "birth" of a neutron with various defined parameters (energy, velocity, position, timestamp, etc.) modelled within a well-defined geometry. These parameters may be selected randomly or be defined, in this case the neutron proper-

ties at birth are defined by sampling from a dataset of known neutron properties supplied by the n_TOF facility. This neutron will continue its path until interacting with another particle within the medium defined according to the similulation. The probability of an interaction taking place (and the nature of the specific interaction) depends on the interaction cross-sections and interaction mechanisms. These interaction cross section are typically supplied by appropriate nuclear data files. This method of particle propagation is continued for the neutron, and any interaction daughter products, until the original neutron and all subsequent daughter products "die" (e.g. are absorbed, escape the system, or in some cases are forcibly removed from the simulation to improve statistical estimators). This process repeats from the particle birth once again, and will do so until reaching a limit specified by the model in question. This actually belies a minor flaw in the Monte Carlo method in that the particles being transported are unable to interact with one another. Nonetheless Monte Carlo is very well suited to solving complex cases of particle transport, capable of achieving results with a low error based on the number of particle histories the modeller elects to run. If sufficient starting particles are simulated the model then follows the Central Limit Theorem (Equation 5.1 [74]), and becomes an accurate representation of the macroscopic properties within the simulation. For a thorough description of Monte Carlo methods see [75].

$$\lim_{N\to\infty} P(S_N) = \frac{1}{\sigma\sqrt{2\pi/N}} e^{-\frac{(x-\mu)^2}{2\sigma^2/N}} \tag{5.1}$$

5.2 Simulation Software - FLUKA

The simulation software used in this investigation was FLUKA [76]. This was partly chosen due to it being the standard choice of simulation package with the EN-STI group at CERN (of which n_TOF is a member). This means the majority of the extremely complex simulation geometry has already been created. FLUKA is a multi-purpose simulation package designed for particle transport along with their interactions with matter, and it is used in a wide range of physics applications. Due to its ability to accurately simulate

neutrons across a large energy range (from 10 μeV up to the TeV range) it is the logical choice for simulating experiments at a neutron producing facility such as n_TOF. A detailed overview of FLUKA can be found online at ***www.fluka.org***.

As mentioned briefly when discussing the Monte Carlo method, such simulations are dependent on datafiles being supplied which have accurate values for interaction cross-sections. Thus the accuracy of a simulation is hugely dependent on the accuracy of these datafiles. The cross section data supplied to the FLUKA package typically come from experimental data collated within ENDF, JEFF, etc. [12, 77], and are usually substantiated with well characterised uncertainties. This, along with well-defined model parameters (e.g. geometry), helps to ensure systematic errors are kept to a minimum. As for statistical errors, FLUKA features several methods of reducing such uncertainties; ranging from simply running more particle superhistories, to employing some of the biasing techniques FLUKA has available.

Another reason for the use of FLUKA is the ability to create custom user routines as FORTRAN scripts which can be used to supplement the main simulation. In particular this simulation campaign has taken advantage of the ability to create custom source routines, in order to replicate the complex neutron beam present at n_TOF (but without having to simulate it from proton pulse impact each time, something which would take an inordinate amount of time). Additionally a custom scoring routine has been used to produce a complete output of the simulation results to enable a thorough and flexible post-processing regime.

For a more detailed description regarding the creation and implementation of a FLUKA simulation please see Appendix A.

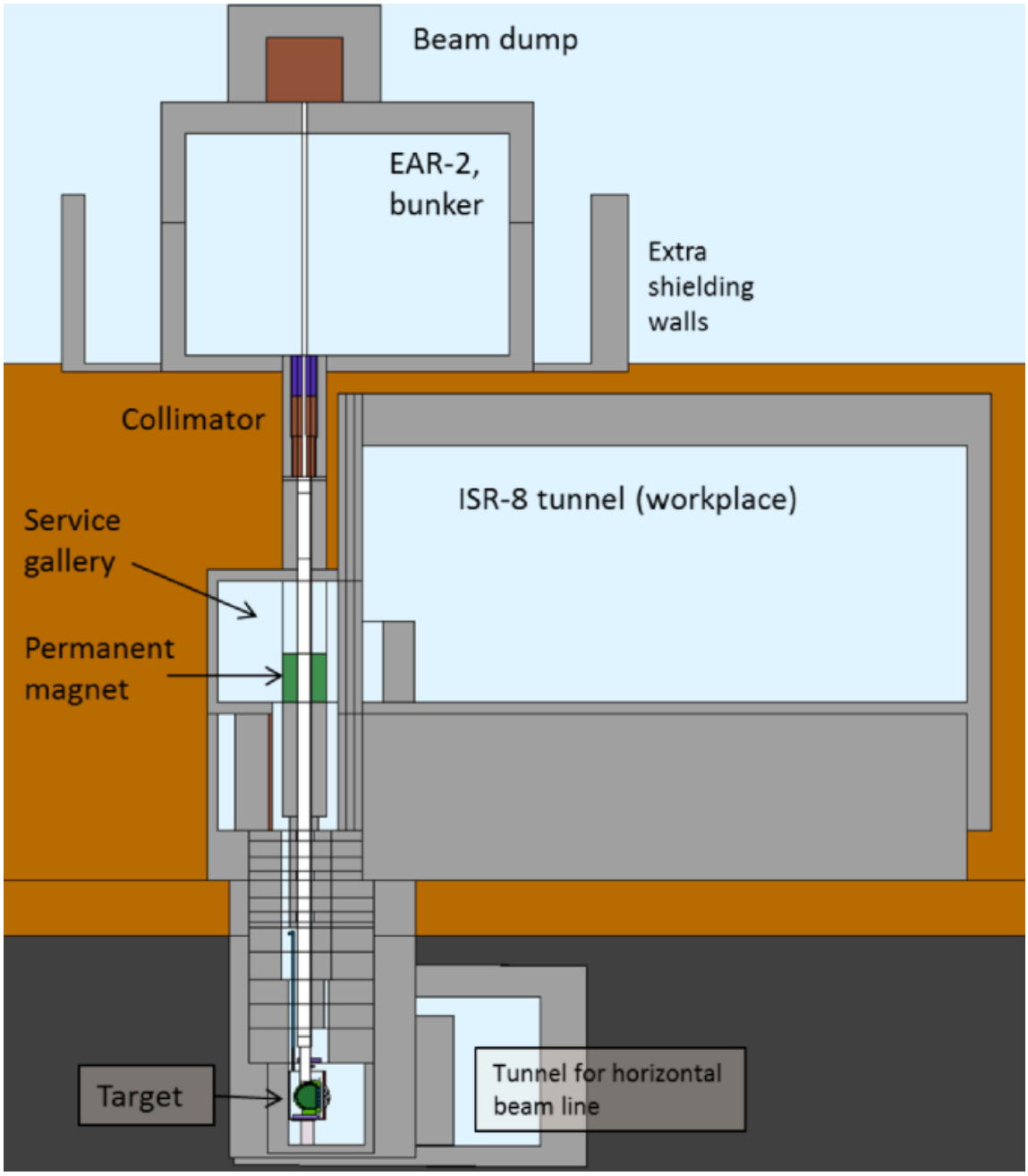

Figure 5.1: A FLUKA geometry snapshot of the EAR2 beamline, as visualised using FLAIR geoviewer [49, 76]

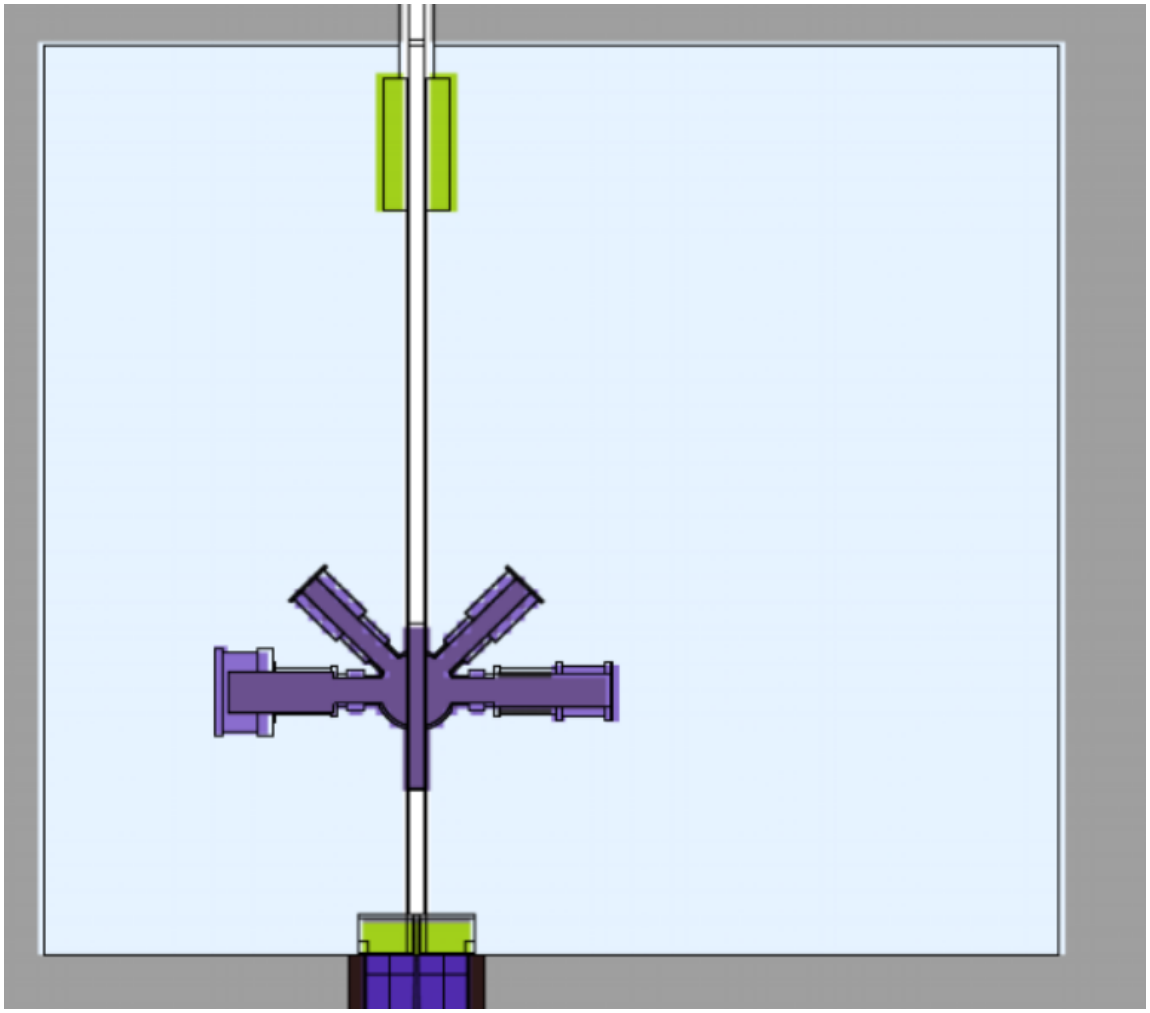

Figure 5.2: A FLUKA geometry representation of the STEFF spectrometer inside the EAR2 experimental hall, as visualised using FLAIR geoviewer [49, 76]

5.3 Simulations

In the run-up to the first experimental campaign, simulation work was undertaken to estimate background levels in the EAR2 facility and, if necessary, come up with a method to mitigate it. A FLUKA geometry file of the n_TOF facility is regularly maintained and updated as the facility evolves (Figure 5.1 shows a snapshot of this geometry file, focusing on EAR2). This base model was then modified to include the STEFF spectrometer within the EAR2 experimental hall, enabling simulations of STEFF within EAR2 (see Figure 5.2).

5.3.1 Background Rate

The primary motivation behind the simulation campaign of STEFF within n_TOF EAR2 was to understand the level of background which would be encountered within the γ-ray detector array, and particularly how this varies with neutron time-of-flight (therefore neutron energy). The coincidence technique employed by the STEFF detector allows for the removal of large swathes of any background data in order to give a clean signal, but if the background level is sufficiently high that the detectors are completely saturated then even such a technique will not be able to achieve any meaningful results. As such it is imperative to investigate the anticipated background level.

The initial simulation performed is what is known as a "sample out" measurement. This replicates the conditions of the eventual experiment except without a sample present in the spectrometer. Performing such a simulation will give some indication of the level of background arising purely from the neutron beam itself. Such measurements are standard at the n_TOF facility and provide key details into background subtraction.

The detector count rate results are achieved by using a custom scoring routine to track particles entering the NaI(Tl) detectors and recording γ rays. Then a correction must be applied to take account of the intrinsic detector efficiency. This correction factor is derived by comparing the results of a simulation to a small experimental result that had already been measured (further details in "Experimental Comparison section below"). Finally the results are then normalised by the time width of the bin, in μs, to achieve a count rate in γ counts μs^{-1}.

As mentioned in Section 4.4.1, a NaI(Tl) detector has a decay constant of 230 ns [72]. This means that count rates above approximately 4 γ counts μs^{-1} will be extremely susceptible to pile-up. This pile-up will need to be corrected for in later analysis in order to achieve meaningful results.

The results in Figure 5.3 suggest that the background count rate will remain above

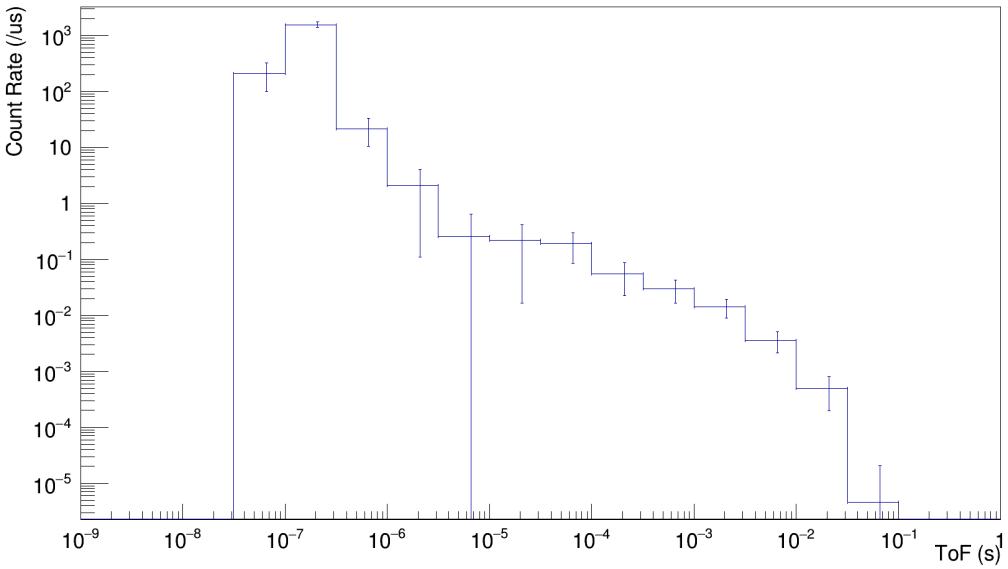

Figure 5.3: The simulated background rate experienced within a NaI detector inside the experimental hall of EAR2, approximately 30 cm from the beam centre - Narrow Collimator setup.

approximately 4 γ counts μs^{-1} up until a time-of-flight of the order of μs. Below this time-of-flight the background count rate is far too high to discern any meaningful information from the NaI(Tl) detectors when using a narrow collimator setup. Initial results suggest that the background rate is in fact higher than the simulation results suggest, likely due to the γ flash. Thus it is expected that the background count rate resulting in the inability to use the NaI(Tl) detectors will extend further in neutron time-of-flight (i.e. to lower neutron energies).

Experimental Validation - Detector Efficiency Correction

The scoring routines which record γ rays entering the NaI(Tl) detector within the simulations do not take any account for the detector efficiency, i.e. for fact that not all of these γ rays will interact within the detector and some will pass straight through undetected. In order to correct for this a simulation was performed in order to cross reference with the experimental results described in Chapter 6.

A model was created featuring a Au-197 target of the same dimensions as that used in

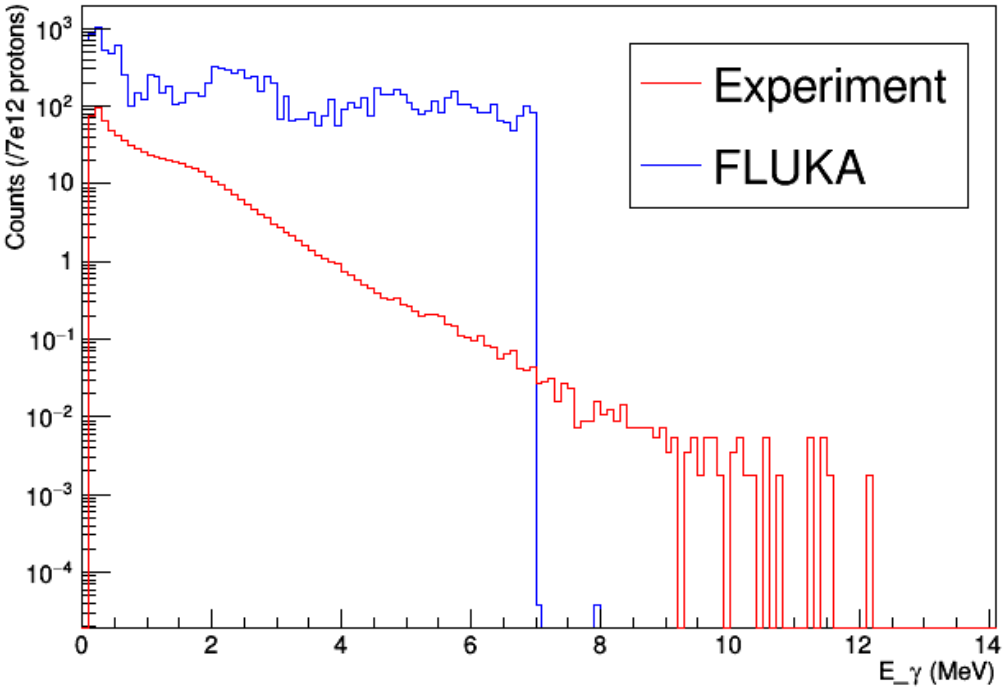

Figure 5.4: A comparison of experimental results of deposited γ-ray energy within a NaI(Tl) detector and the simulated fluence of γ rays entering the same detector. The experiment and simulation in question consider the first capture resonance of the ^{197}Au(n,γ) reaction, in order to minimise the effects of background γ rays. The ratio of these results (experimental / simulation) gives an approximation of the detector response to a given γ-ray fluence, i.e. the efficiency of the detector, plotted in Figure 5.5.

the experiment, and the γ-rays passing through the NaI(Tl) recorded in the same fashion as previously described. Then a comparison of the simulated data (i.e. γ rays crossing the detector boundary) and the experimental data (i.e. the detector response) was made in order to find an approximate detector efficiency. The efficiency of a detector depends upon incident γ-ray energy, therefore this comparison must cover a wide γ-ray energy range (in this case up to approximately 7 MeV). Figure 5.4 compares the deposited energy spectra from the experimental results with the γ-ray fluence entering the simulated detector volumes. These results employ a time cut surrounding the first capture resonance of Au-197 in order to minimise background contributions. The ratio between simulated and experimental (an analogue for detector efficiency) is plotted as a function of γ-ray energy (E_γ) in Figure 5.5. Fitting these data gives a reasonable approximation that can be used for

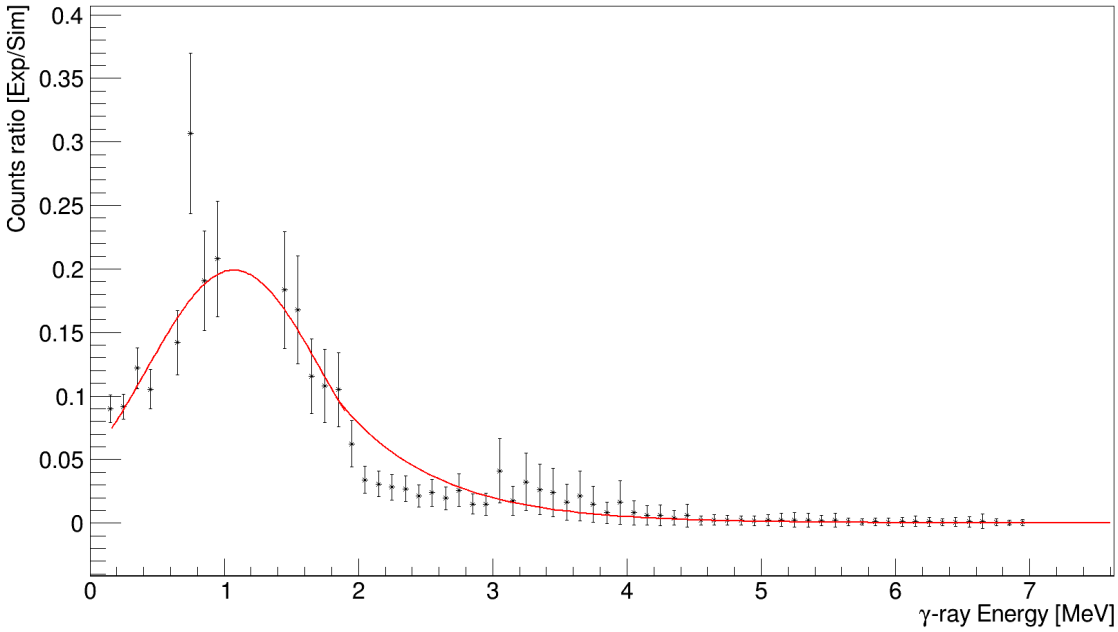

Figure 5.5: Ratio of results for simulated γ fluence passing through NaI(Tl) detector volumes and experimentally measured deposited energy for the ^{197}Au (n,γ) reaction, as depicted in Figure 5.4, an approximate analogue for detector efficiency.

efficiency corrections when analysing simulated data. These data are fit using a Gaussian distribution up to 1.8 MeV and then an exponential distribution for higher energies. It is likely that this fit could be improved, however as only an indicative approximation for the efficiency is required this will suffice. The efficiency of the NaI(Tl) detector array was later calculated experimentally and the results used in the analysis within Chapter 8, the efficiency curve plotted in Figure 5.5 is only used within the analysis discussed in this chapter and not the results discussed later.

Collimator Comparison

The results above are based upon simulations for a narrow aperture collimator, as discussed in Chapter 7 the STEFF spectrometer will be used in two different experimental campaigns, one featuring this simulated narrow collimator and another featuring a wider aperture collimator. This second, wider collimator will result in a greatly increased neutron flux incident upon the target within STEFF, however, it will also result in a much higher

background rate within the NaI(Tl) detectors.

In order to understand the background rate anticipated, a second set of simulations has been performed using this new, wide collimator geometry. Figure 5.6 demonstrates the simulated difference in count rate between the narrow and wide collimators, the simulated collimator geometries are shown earlier in Figure 3.4. It can be seen that the wide collimator setup increases the background count rate by up to a factor of 60, though on average it is closer to a factor of around 20, and reaching as high as 10,000 γ counts μs^{-1} (in the energy region of approximately 20 - 200 MeV).

Figure 5.6 demonstrates that for the wide collimator setup the detection limit for the NaI(Tl) detectors is breached lasting until much higher values for neutron time-of-flight (i.e. measurements are only feasible at much lower neutron energies). This is to be expected as the increased flux through a wider aperture collimator increases the background. The background rate from the wide collimator setup does not fall greatly below the measurable detector limit until time of flights in the order of 10^{-4} to 10^{-3} seconds, corresponding to neutron energies in the region of 2 to 200 eV. This means for the wide collimator it will be difficult to measure for energies above these values.

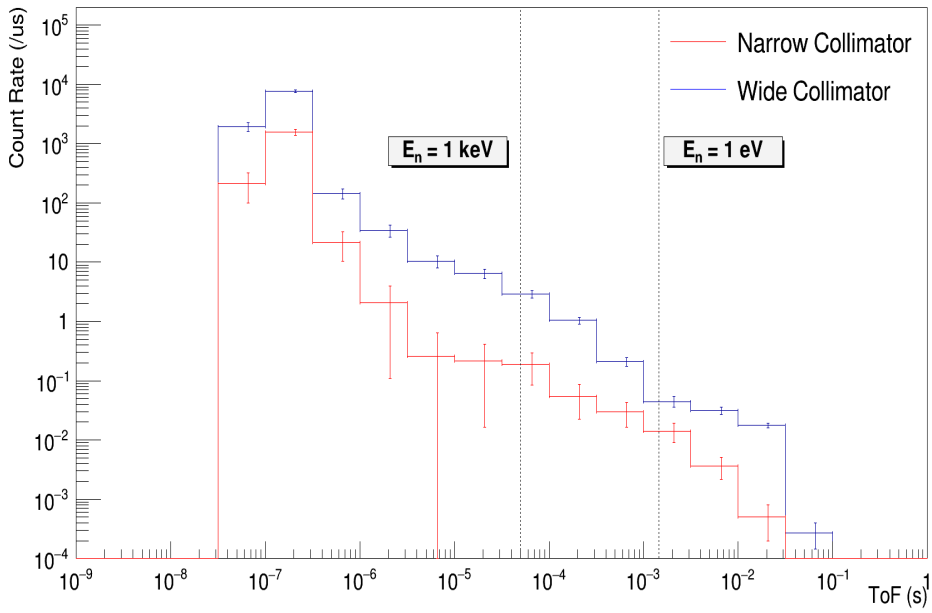

Figure 5.6: Simulated Background rates for both narrow and wide collimators, as they vary for neutron time-of-flight. Markers have been included to show the neutron time-of-flight values corresponding to a neutron energy of 1 eV and 1 keV (an increased time-of-flight means a decreased neutron energy).The ratio of these values has been plotted in Figure 5.7.

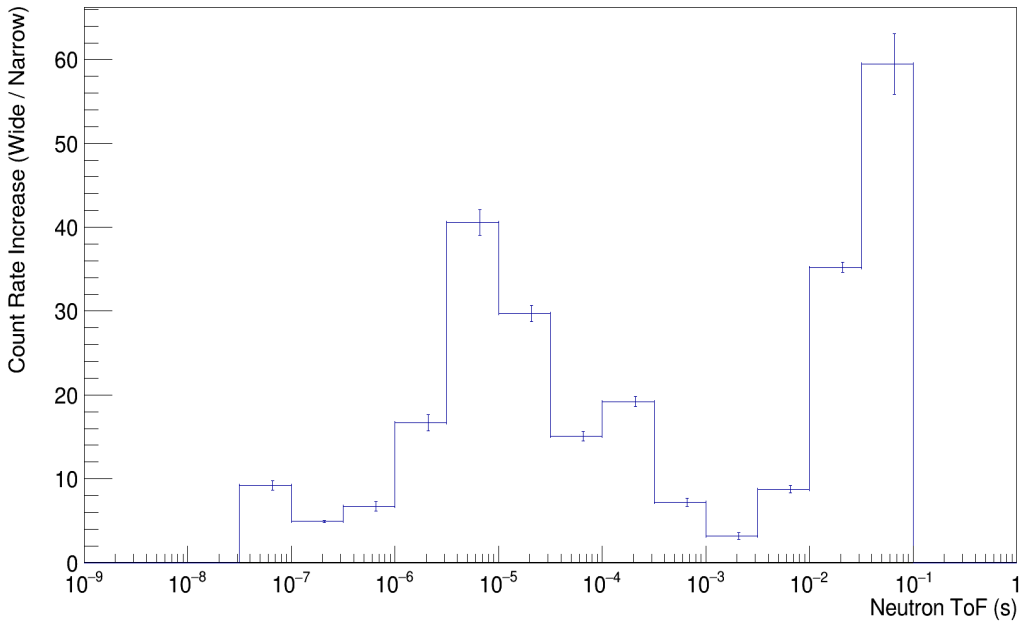

Figure 5.7: Ratios of the background rates experienced with each collimator setup. Data shown in Figure 5.6

5.3.2 Shielding Investigation

As shown above, moving to a wide collimator setup has a large effect on the background rate present within the NaI(Tl) detectors. In order to try and push the detection limit of these detectors to higher neutron energies, by lowering the background experienced, a proposal was made to introduce shielding in a variety of possible setups. The two main proposals were to apply shielding around the lower section of beampipe below STEFF (example in Figure 5.8a) or surround individual NaI(Tl) detectors with their own dedicated shielding (Figure 5.8b); with each of these options further investigated to try and optimise their shielding potential.

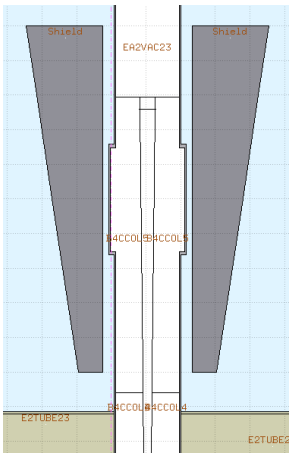

(a) Shielding of central beam pipe.

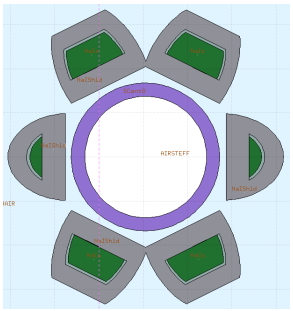

(b) Shielding of NaI detectors directly

Figure 5.8: Two images demonstrating examples of types of shielding investigated. More examples and further results can be found further below.

Beampipe Shielding

Since it is suspected that a substantial portion of any background γ-ray activity is due to interaction between the neutron beam and second beam collimator [47], one of the logical options when shielding is the aforementioned shielding of the lower section of beam pipe below the STEFF detector. This placement should serve to maximise any background degradation by placing shielding material in direct line between the source (i.e. the collimator) and the detectors.

The background is more complex than just being γ rays because there is also a non-negligible proportion of neutrons present; so a shielding setup which mitigates both of these factors is ideal. Due to this the shielding investigation simulated a variety of shielding geometries composed of a mixture of lead, a high-Z material to attenuate γ rays, and borated polyethylene (BPE), a material which used polyethylene to slow down neutrons and boron to subsequently capture the now thermalised neutrons.

The result of this shielding investigation can be seen in Figure 5.10. The effect of shielding depends on the neutron time-of-flight. There is a clear distinction between neutron time-of-flight values $< 10^{-4}$ seconds and above this value. Below 10^{-4} seconds the background rate exceeds 1 γ ray per μs, for all shielding setups - in almost all time-of-flight bins the presence of shielding increases the background rate (likely due to increased material interacting with the neutron beam). Thus in this time-of-flight region there is no benefit to introducing shielding. Above 10^{-4} seconds the background rate is below 1 count per μs, regardless of shielding setup. Therefore within this region there is also insufficient benefit to implement any shielding as investigated here.

Overall the results demonstrate that any potential net benefit of installing such a shielding setup does not justify the time, energy and cost to produce the shielding configuration along with commissioning and installing it. Therefore it was decided that beampipe shielding would not be implemented.

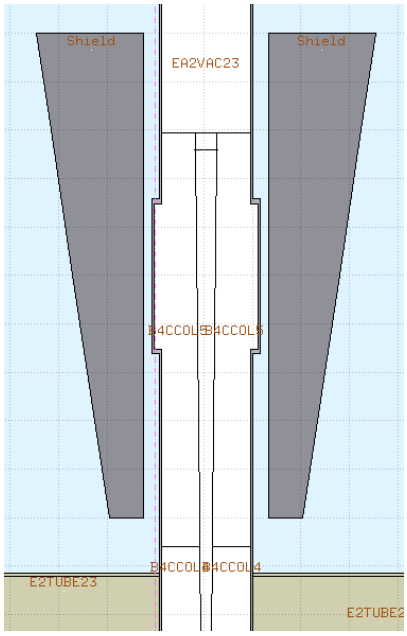

(a) Shielding option 1: Wholly lead

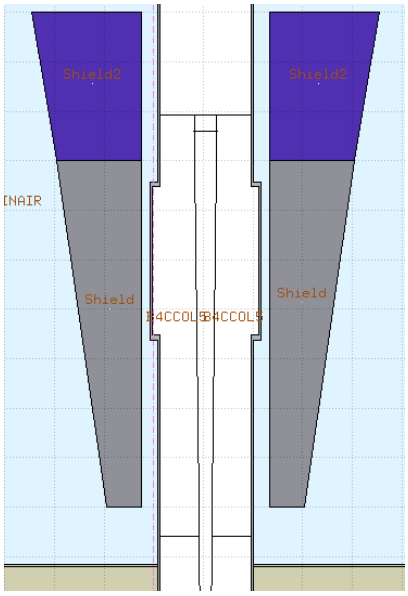

(b) Shielding option 2: Lead for 70cm followed by 30cm of BPE

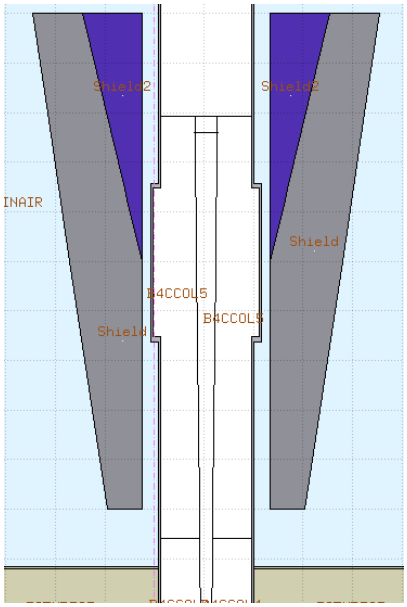

(c) Shielding option 3: 50cm of lead only, follow by 50cm of BPE surrounded by lead

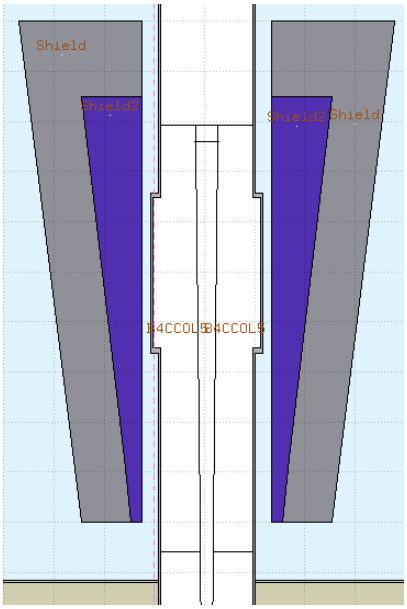

(d) Shielding option 4: BPE centre surrounded by lead for the first 80cm, followed by 20cm of solely lead.

Figure 5.9: A visual comparison in FLAIR geoviewer of the different beampipe shielding options considered (also simulated but not shown was an absence of shielding altogether). The purple zones represent borated polyethylene (BPE) and the grey represents lead. The top of the second beamline collimator can be seen at the base of the images, for reference, and not shown (due to the cut chosen in the vertical axis) are the NaI(Tl) detectors which would be above the shielding between it and the base of STEFF.

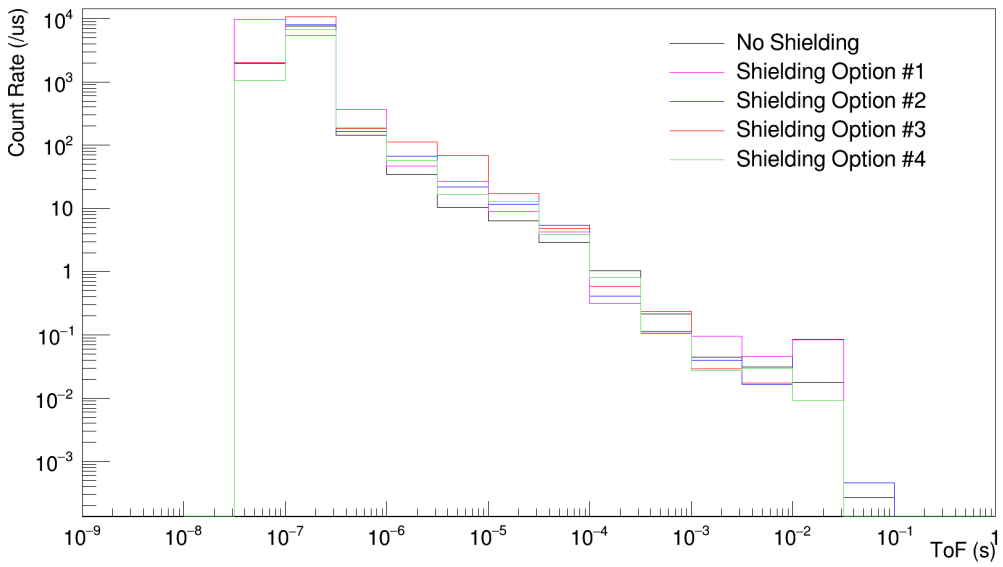

Figure 5.10: Comparison of the simulated background γ rates for each of the shielding options discussed previously (along with the results of simulations with no shielding), as varying for neutron time-of-flight.

NaI Shielding

This investigation was performed for the narrow collimator set up and was performed prior to the efficiency correction being established. The results are thus presented as purely indicative. The investigation into directly shielding the NaI(Tl) detectors consisted of four possible geometries (two of which are shown in Figure 5.12, along with the default 'no shielding' option). The geometries investigated are:

- *Full Shielding* - The entire NaI(Tl) detector is surrounded by several inches of lead.
- *Open Front Shielding* - The rear of the detector and the curved edges are surrounded by lead.
- *Open Back Shielding* - The front of the detector and the curved edges are surrounded by lead.
- *Open Front and Open Back Shielding* - Only the curved edges are surrounded by lead.

All of these shielding setups other than the '*Open Front and Open Back Shielding*' would require a redesign of the NaI(Tl) detector array in order to accommodate these new large quantities of lead. As such, in order to make such a drastic alteration to the experimental setup worthwhile, these shielding setups will need to drastically reduce the background rate encountered within the scintillators.

However, as can be seen in Figure 5.11, the only shielding geometry which reduces the background in any meaningful way is the '*Full Shielding*' setup. Such a setup would also reduce the count rate seen from any measurement, as there is now an appreciable amount of shielding between the sample within the STEFF central chamber and the NaI(Tl) detectors. There would also be a dramatic effect on the spectra of γ rays detected, due to increased scattering interactions with this lead shielding broadening the energy range of detected γ rays. Overall it is demonstrated that directly shielding the NaI(Tl) detectors is not a viable solution to reduce background rates.

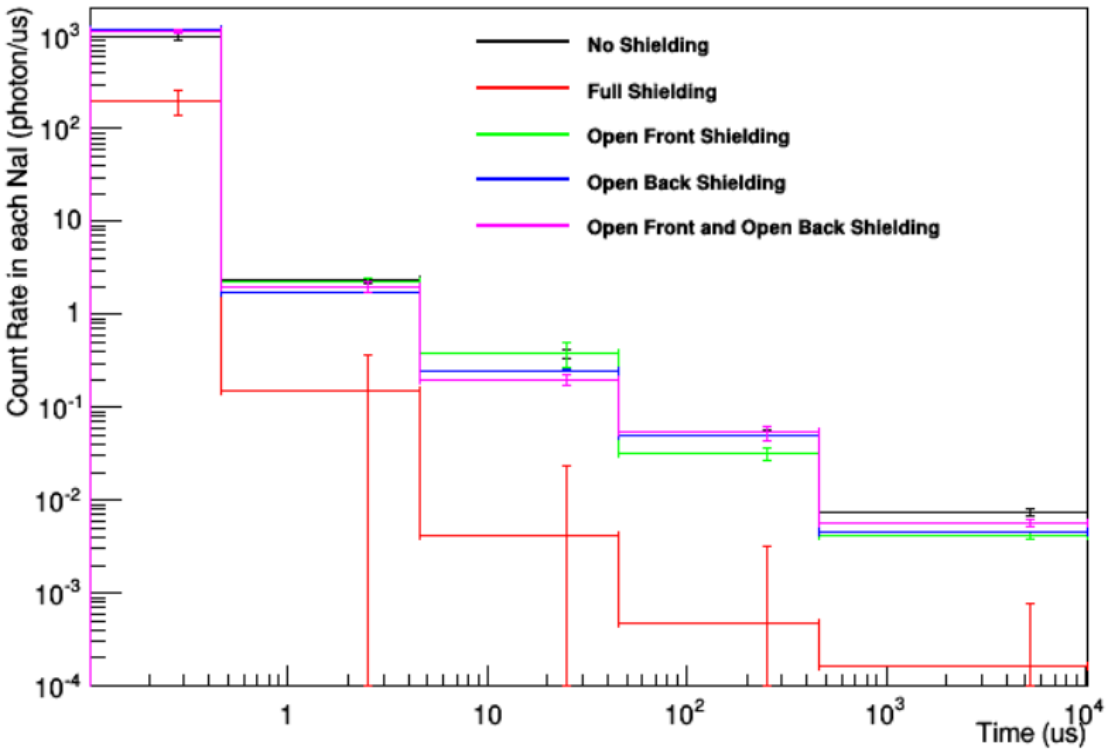

Figure 5.11: Simulated background γ rate results from the simulation investigation into direct shielding of the NaI(Tl) detectors. Rates varying with neutron time-of-flight. The discrete bin structure is consistent with time windows used in [44].

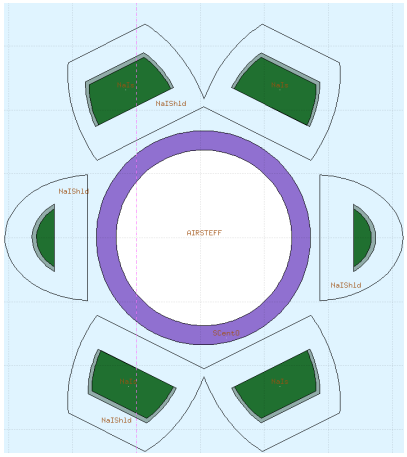

(a) No Shielding around the NaI detectors.

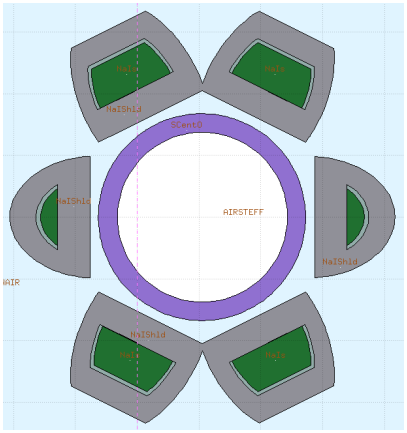

(b) Shielding fully encasing the NaI detectors

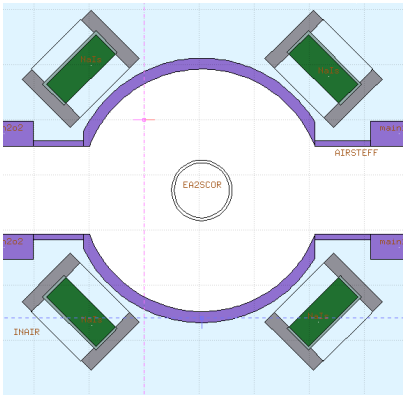

(c) Shielding surrounding the sides of the NaI detectors but not the front and rear. Image taken from a different viewpoint to demonstrate the shielding better.

Figure 5.12: Three examples of the shielding geometries simulated for the direct NaI(Tl) shielding investigation. N.B. There are two further shielding geometries which have been modelled but they do not lend themselves well to being viewed in geoviewer.

6

Detector Development - NaI(Tl) Scintillators

Before proposing experiments at the n_TOF facility it was well understood that the γ-ray background rate encountered would be much higher than those experienced in previous STEFF measurements at the ILL [9]. NaI(Tl) are relatively slow scintillation detectors, with a 230 ns decay constant, thus the detectors are not especially suited for high count-rate applications. Therefore extensive work was done to optimise the available detectors for the measurement at the n_TOF facility.

6.1 Pre-Development Status

In order to investigate the limits of the detectors prior to the experimental runs, a single NaI(Tl) detector was used within EAR2 at n_TOF. In order to maximise the γ-ray count rate present when testing this NaI(Tl) detector, a large gold sample was placed in the neutron beam. The element gold naturally contains a single isotope, Au-197, which has a large resonance for the (n,γ) reaction (as shown in Figure 6.1). This large resonance combined with the large neutron flux present at n_TOF will result in a large reaction rate, and subsequent γ-ray emission. The cross section also varies significantly with neutron energy, thus varies significantly over the duration of a single neutron pulse. Therefore this single measurement affords the opportunity to investigate the response of the NaI(Tl) detectors to various count rates.

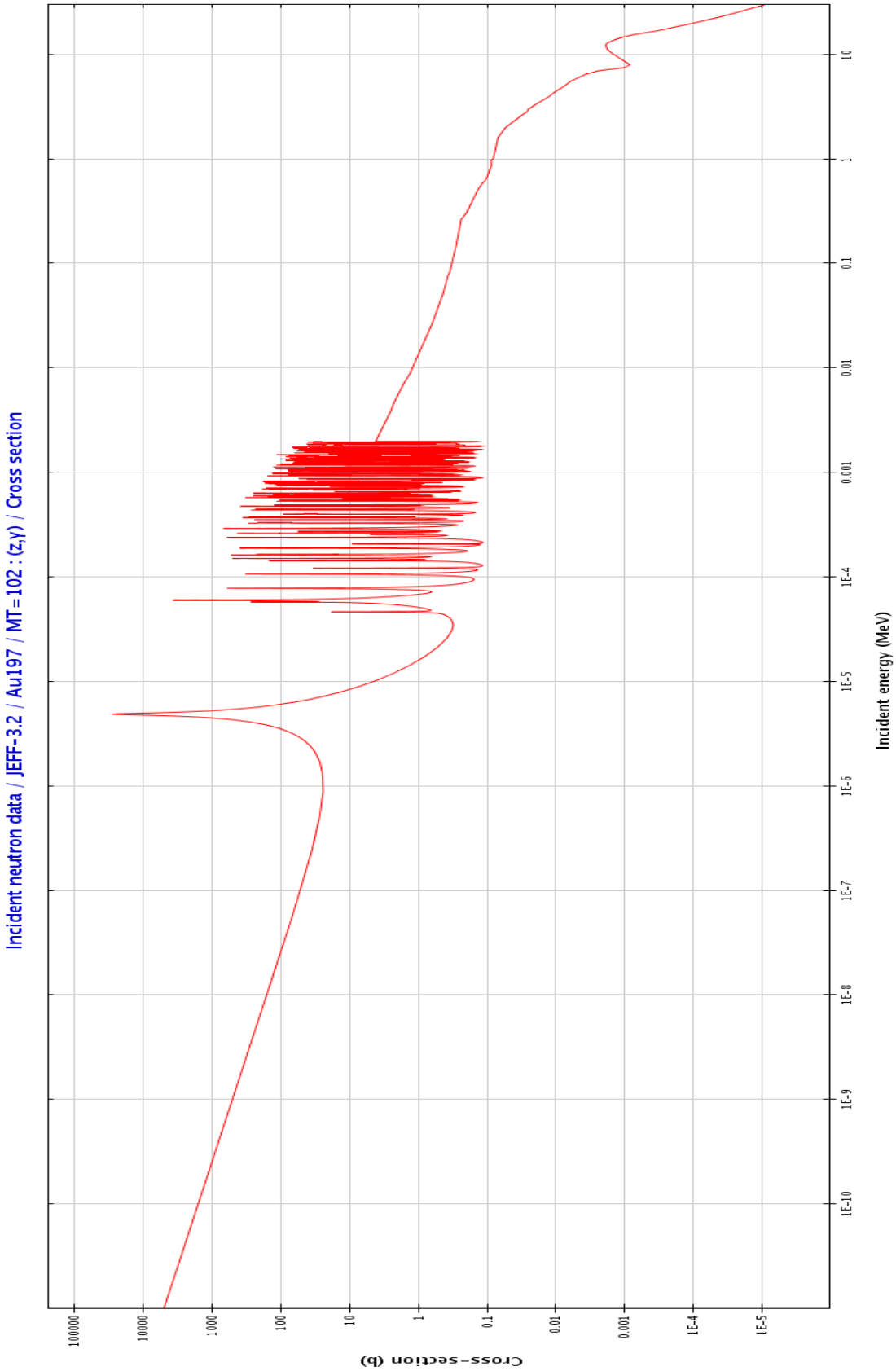

Figure 6.1: Cross-section for the ^{197}Au(n,γ) reaction, taken from JANIS [78] and JEFF-3.2 [77]. This evaluated cross-section is determined by collating the results from multiple experimental measurements and combining these with theoretical predictions.

The result of this initial testing can be seen in Figure 6.2. The limit of the NaI(Tl) detector is readily apparent. The detector fails upon reaching a count rate of approximately 1.5 counts per microsecond, shown by the large dip in the first capture resonance.

Examining the raw signal trace in the time-of-flight region corresponding to this capture resonance gives a clearer indication of what is occurring. Figure 6.3 shows the raw signal within a GUI developed by the n_TOF team. This shows that the detector is failing catastrophically in the centre of the resonance, and a high count rate region can be seen either side of this failure.

The company which manufactured these NaI(Tl) detectors, *Scionix Ltd.*, modified the detector photomultiplier tubes (PMTs) in order to reduce the time it takes for a detector signal to return to the baseline and improve the detector response to a high count rate [79]. The original pre-modified circuitry of the PMTs can be seen in Figure 6.4. Details of the modifications and the results of post-modification testing also follow.

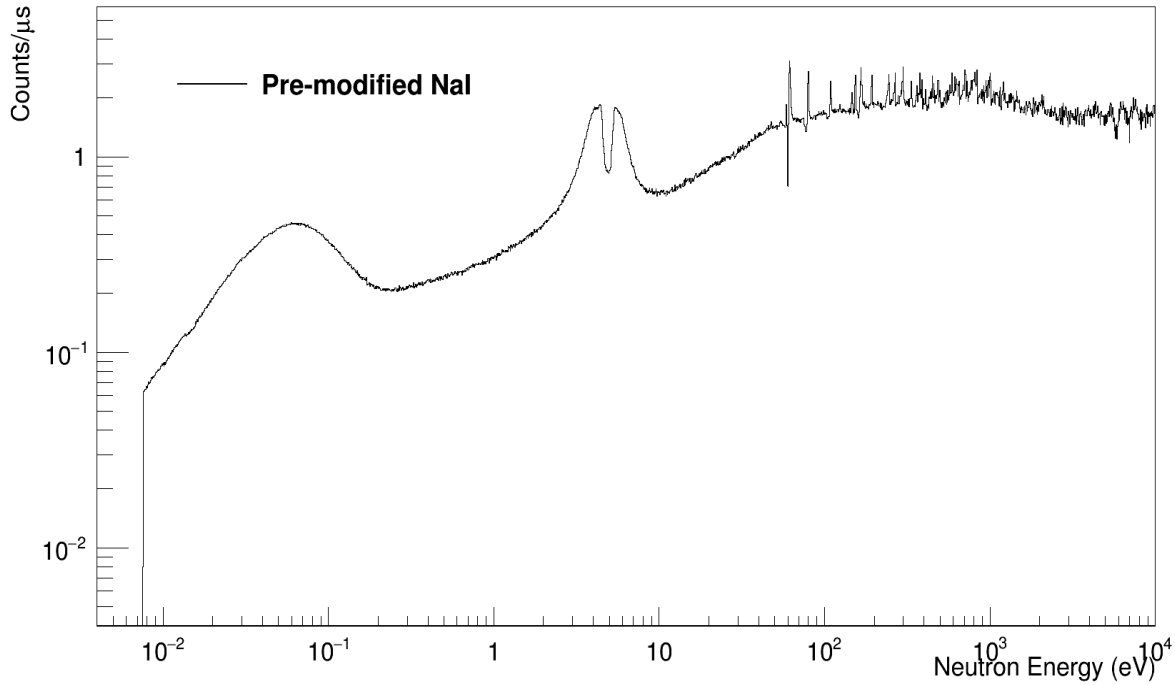

Figure 6.2: Neutron time-of-flight γ-ray spectrum for a Au-197 sample, as measured by a NaI(Tl) detector prior to any modifications. The catastrophic failure of the detector demonstrated in pulse trace in Figure 6.3 can be clearly seen within the first resonance at 5 eV.

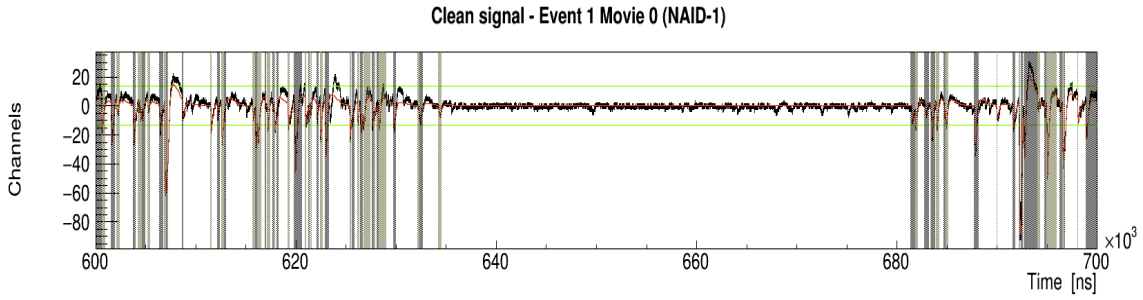

Figure 6.3: The raw signal from the NaI(Tl) detector, prior to any modifications, during Au-197 measurement. The catastrophic failure of the detector can be clearly seen around the 630 μs to 680 μs region, corresponding to a neutron energy of approximately 5 eV, the energy of the first neutron capture resonance in ^{197}Au.

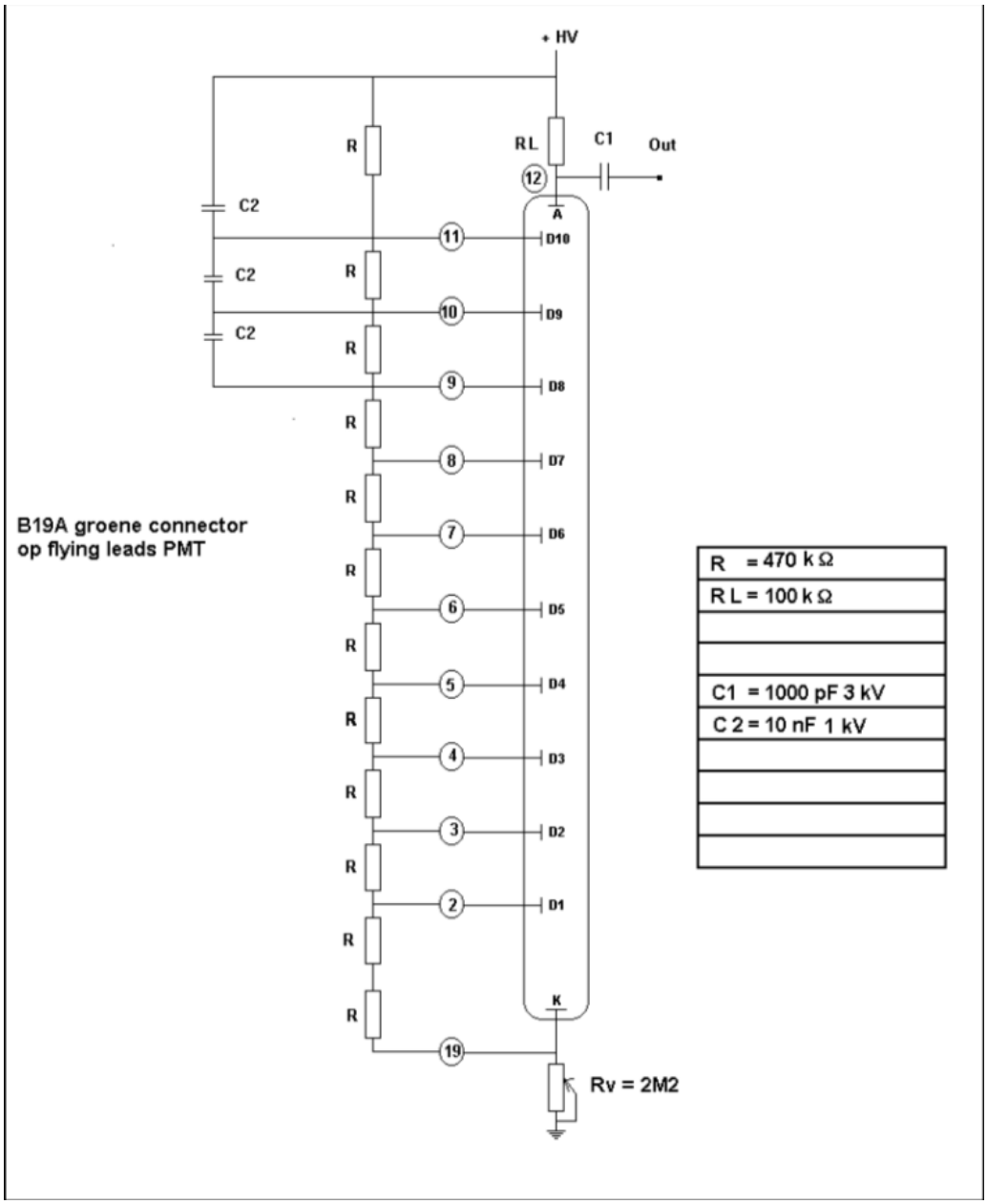

Figure 6.4: Circuit diagram for the photomultiplier tubes attached to the NaI(Tl) detectors, prior to any modifications. The detectors were used in this configuration for any previous STEFF experiments. Diagram courtesy of *Scionix Ltd.*.

6.2 Post-Development Results

Initially a single NaI(Tl) was modified, in order to test how much improvement could be gained before modifying the whole array. The updated circuitry of the photomultiplier tube can be seen in Figure 6.5. The most notable changes in the circuitry are the switching of the voltage from a positive high voltage to a negative high voltage supply, the shortening of the resistor chain, increasing the capacitor chain and the removal of a capacitor from signal out line. These modifications serve to decrease the density of the electron cloud within the photomultiplier tube and removing the capacitor from the signal out line removes the issue with the pulse shape overshooting upon returning to the baseline [79].

Figure 6.6 shows the new pulse shape after these modifications were carried out, compared with the previous pulse shape. Straight away it can be seen that the baseline overshoot present prior to the modifications has disappeared. However, to confirm that detector performance has also improved, another high count rate measurement was performed.

The detector was used for another measurement of a ^{197}Au(n,γ) reaction in order to test the new limits of the modified detector. Figure 6.7 shows the raw signal trace of the modified detector during this measurement, and the improvements can be seen instantly. The detector no longer fails catastrophically in the high count rate region within the capture resonance.

In order to investigate the magnitude of count rate with which the detector can cope, another count rate vs. neutron time of flight plot is shown in Figure 6.8, along with the pre-modified results for comparison. There is no detector failure in the centre of the resonance now, and the count rate reaches as high as several counts per microsecond. The flattened top of the resonance shape in these results signifies that the resonance is “saturated”, i.e. every single neutron of this resonance energy impinging upon the Au-197 sample undergoes an interaction. This means it is possible that the detector is capable of measuring rates higher than those seen here, but with the sample which was measured it is not possible to tell for certain.

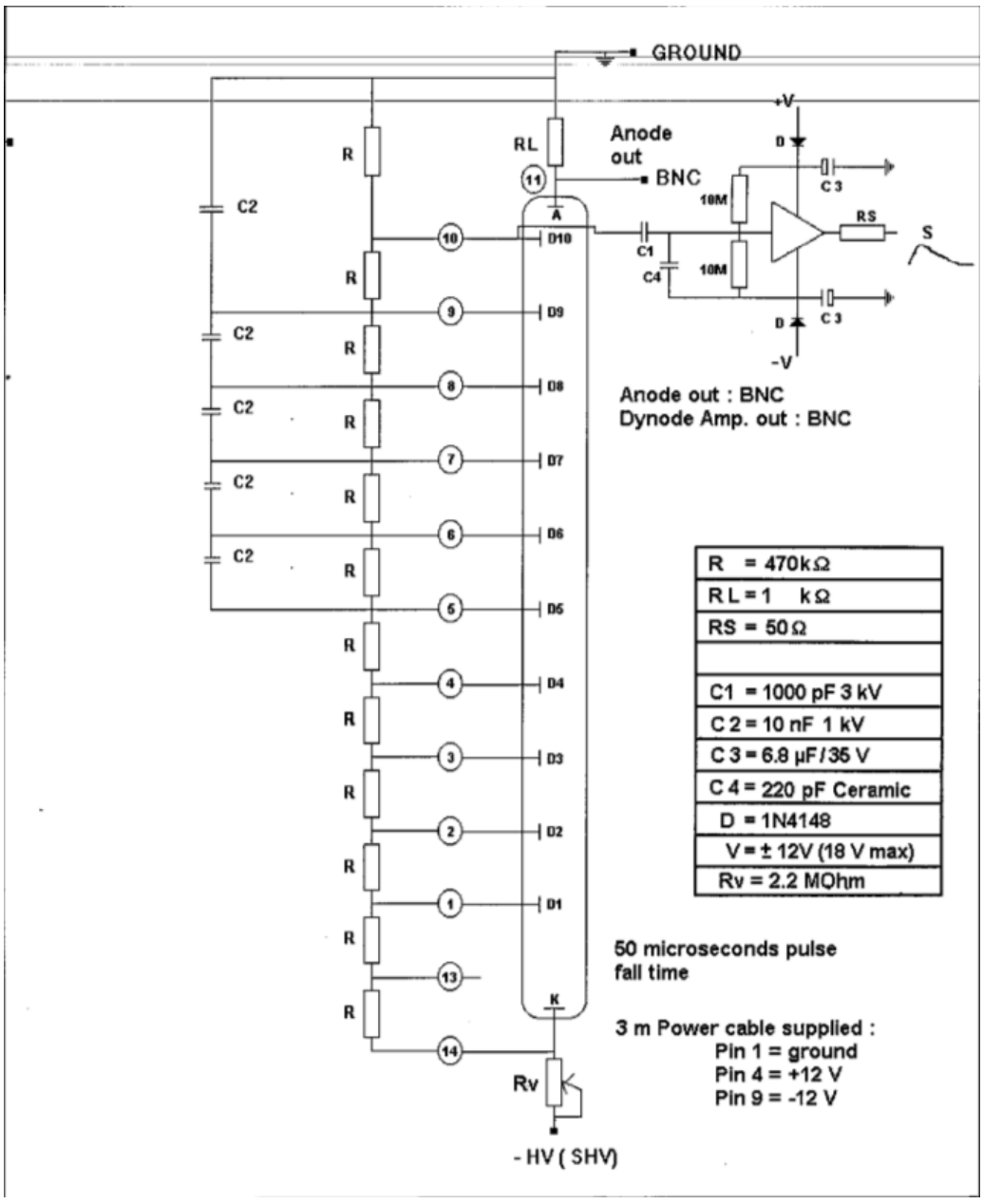

Figure 6.5: Circuit diagram for the NaI(Tl) detectors, after their modification. Diagram courtesy of *Scionix Ltd.*.

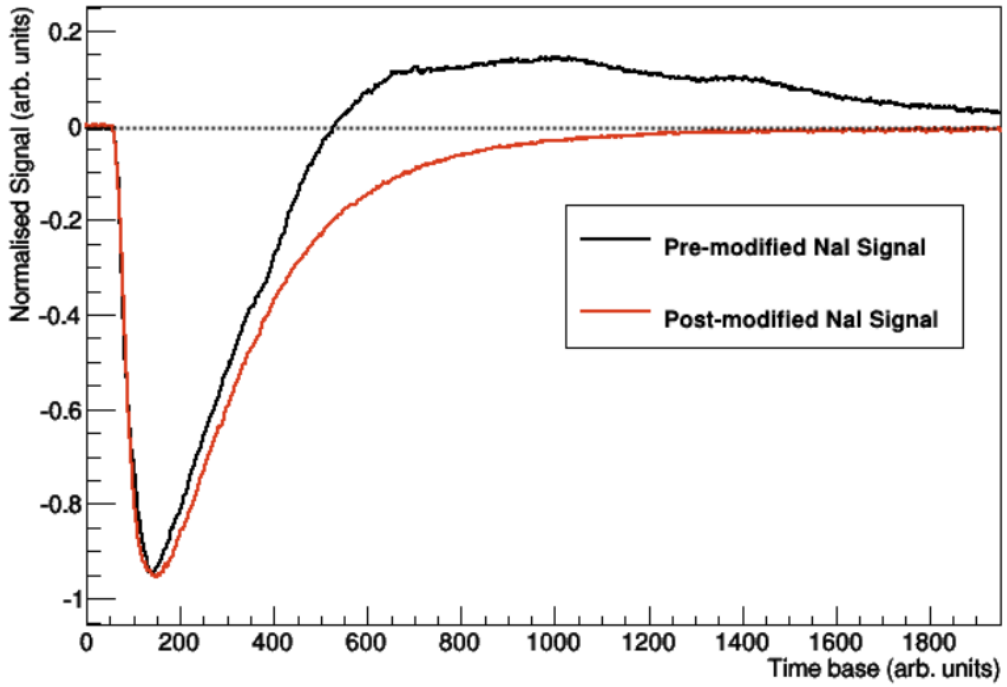

Figure 6.6: Comparison of an average NaI(Tl) detector signal pulse pre-modification and post-modification. Prior to modification work there exists a long baseline overshoot which is removed in the post-modification trace. The x-axis scaling is two units to one nanosecond, i.e. the width of this figure is 1000 nanoseconds.

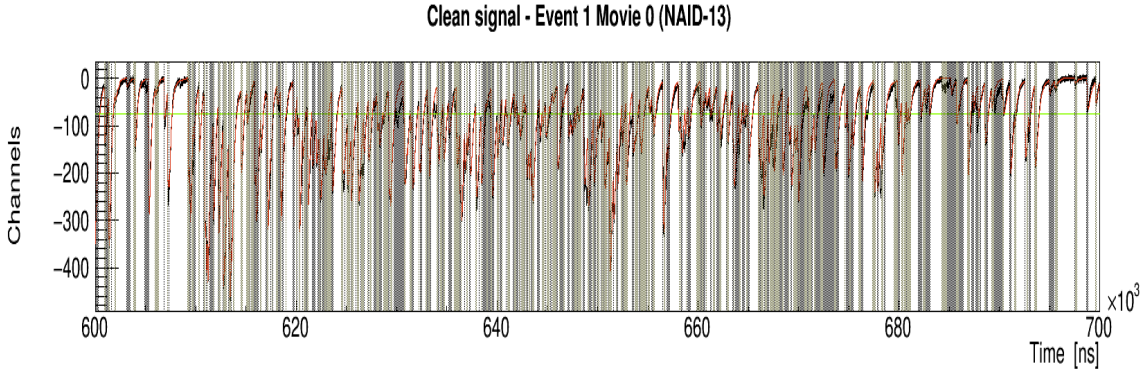

Figure 6.7: Raw signal trace for the same time region as in Figure 6.3, showing how the NaI(Tl) no longer succumbs to total saturation and detector death. The grey vertical stripes represent potential signals identified by the pulse processing software, and the red line represents the softwares attempts at performing a pulse shape analysis routine on the signal trace.

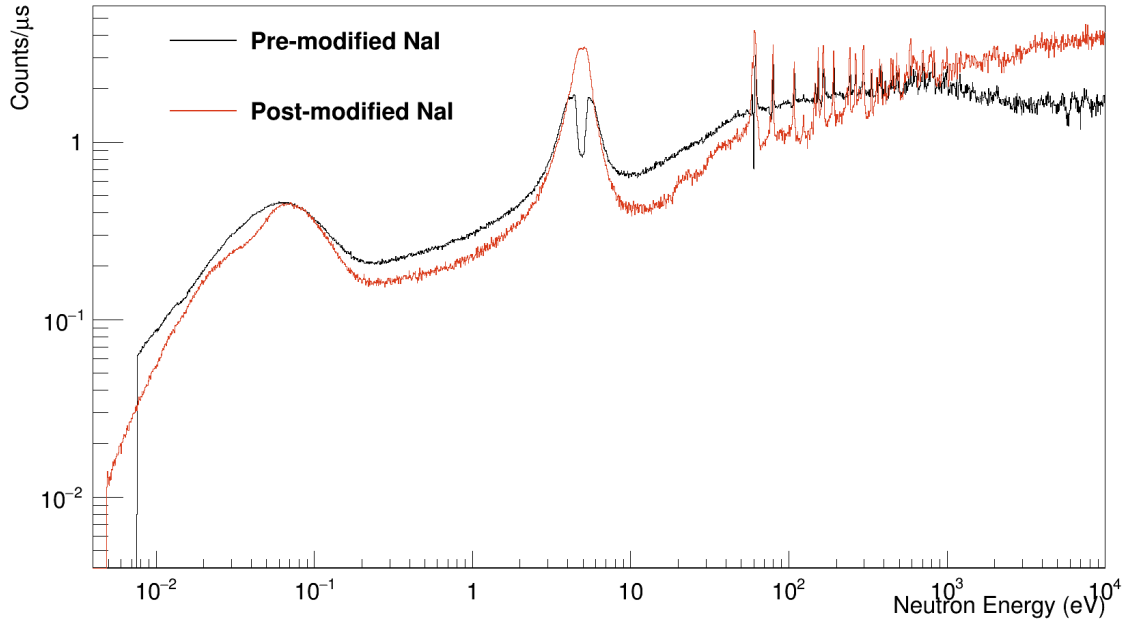

Figure 6.8: Spectra comparing the NaI(Tl) response to ^{197}Au(n,γ) reactions, pre- and post-modifications. The detector post-modification no longer exhibits a failure in the middle of the first capture resonance.

It is important to confirm that the modifications made in order to improve the NaI(Tl) response to a high count rate environment do not detract from the detector performance in the low count rate region, and also that a reasonable energy resolution is maintained. In order to confirm this was the case, a 300 kBq activity ^{88}Y source was used to perform a calibration measurement.

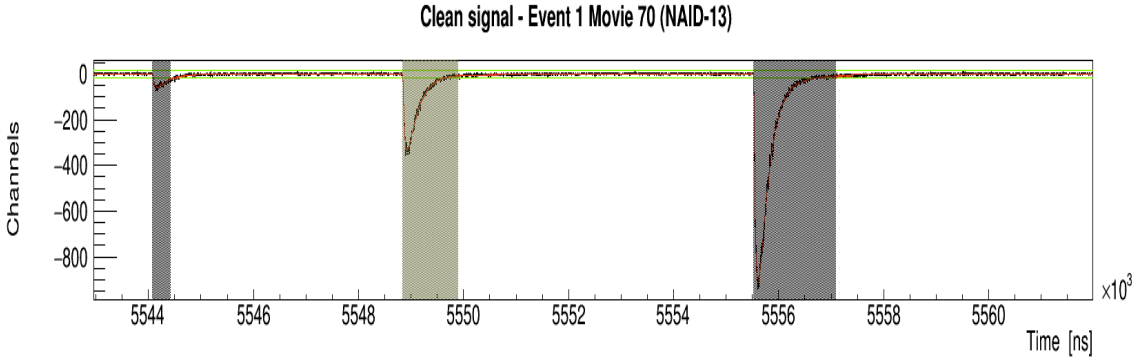

Figure 6.9: Post-modification NaI(Tl) detector raw signal trace in a low count rate environment.

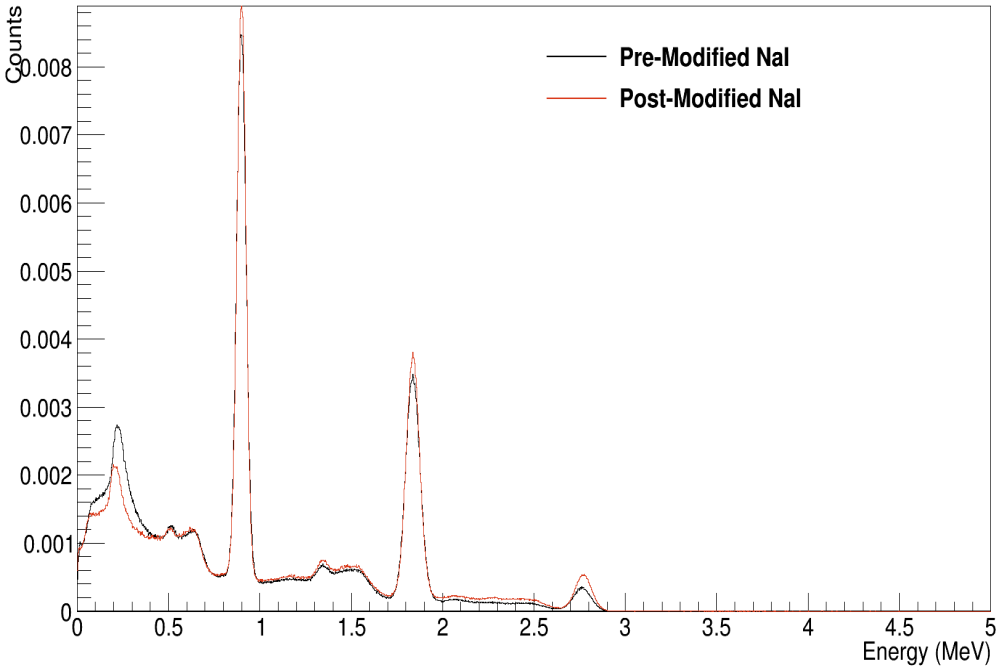

Figure 6.10: Energy resolution comparison between pre- and post-modified NaI(Tl) detector. Measured using a Y-88 calibration source.

Examining the raw signal trace, as shown in Figure 6.9, shows that the signal integrity is maintained. The trace is smooth and the detector exhibits a good signal-to-noise ratio. Figure 6.10 demonstrates the the resolution of the detector has not been compromised, and matches that of the pre-modified detector; i.e. 6.8% resolution at 898 keV and 4.9% resolution at 1836 keV.

6.3 NaI(Tl) Calibration and Testing

The work described in this section occurred between experimental phase one and phase two. However, the work was key to analysing phase one data so this discussion has been included beforehand.

In order to have an accurate picture of what is occuring within the NaI(Tl) a few key steps must be followed. Firstly each NaI(Tl) detector must be calibrated in energy in order to be able to extract energy data from the γ-ray signals. Then also there is a timing

calibration process which must be undertaken, to remove any systematic discrepancies which may occur. Finally it must be confirmed that the detector is indeed maintaining its performance under all environments present within the experiment. In this case this refers to maintaining detector stability across a range of count rates within the detector.

The calibration in time and energy took place immediately after the ^{235}U portion of experimental phase one. This was investigated whilst STEFF remained inside the experimental hall and various calibration sources were placed within the central chamber.

Energy Calibration

Experimental phase one (as described in Section 7.1) consisted of two distinct portions: *Measurement* (^{235}U) and *Calibration* (^{252}Cf, a spontaneous fission source, along with various γ-ray sources).

The *Calibration* portion began immediately after the removal of the ^{235}U source from the STEFF central chamber. A variety of γ-ray calibration sources were then used to cover a wide range of energies in order to calibrate the NaI(Tl) array as accurately as possible. These sources, and their corresponding γ-ray energies are:

- ^{88}Y, $E_\gamma = 898$ keV and $E_\gamma = 1816$ keV
- ^{60}Co, $E_\gamma = 1173$ keV and $E_\gamma = 1333$ keV
- ^{137}Cs, $E_\gamma = 662$ keV
- ^{241}Am-^{9}Be, $E_\gamma = 4439$ keV - ^{9}Be(α,n)^{12}C, followed by a ($2^+ \rightarrow 0^+$) transition.
- ^{244}Cm-^{13}C, $E_\gamma = 6130$ keV - ^{13}C(α,n)^{16}O, followed by a ($3^- \rightarrow 0^+$) transition.

The calibration graphs for each NaI(Tl) detector can be found in Appendix B and the calibration equations in Table 6.1. It can be seen that these detectors are well-calibrated and exhibit a very linear behaviour, particularly in the area of interest for this measurement (the distribution of γ rays expected is around the order of 1-2 MeV energies, as explained in Chapter 2).

NAID #	Calibration Equation
0	Y = 0.0129195 X – 0.00712738
1	Y = 0.0128334 X – 0.00863833
2	Y = 0.0139299 X – 0.0378018
3	Y = 0.0145871 X – 0.024754
4	Y = 0.0145799 X – 0.0237919
5	Y = 0.0122371 X – 0.0314031
6	Y = 0.0149873 X – 0.023302
7	Y = 0.0128142 X – 0.0148963
8	Y = 0.0119709 X + 0.0150405
9	Y = 0.0124871 X + 0.000889994
10	Y = 0.0138741 X – 0.0424987
11	Y = 0.0126345 X – 0.00667535

Table 6.1: Calibration equation for each NaI(Tl) detector. Y represents the γ-ray energy in units of MeV, X represents the signal amplitude in units of detector channels.

Timing Calibration - Detector Offsets

The NaI(Tl) detectors are spread across multiple cards within the data acquisition system. This introduces a slight difference in the timestamps of simultaneous events detected in different NaI(Tl) detectors. This slight difference can have large effects when it comes to applying time gates to the NaI(Tl) data. To correct for this, the timing offset for each detector must be determined, relative to some fixed detector. The detector chosen to be fixed was *NAID #0*.

Using a calibration source which emits multiple γ rays simultaneously it is possible to determine the offset of each individual detector, relative to *NAID #0*. Figure 6.11 shows the distribution of values for this offset, in each detector; the average of each distribution is plotted in red. This method is susceptible to distortion due to outlying values skewing the average result (as is clear from the position of the calculated mean relative to the distribution). This is improved by scanning for a signal energy corresponding to one of the calibration signals in *NAID #0* and then search the other detectors within the array for the nearest signal corresponding to the other γ ray emitted. This is referred to as "*Amplitude Correlation*".The result of this is a narrow set of distributions with a more representative value for the distribution mean, as shown in Figure 6.12. These offset distribution mean values are collated in Figure 6.13 and within Table 6.2, which also contains the card

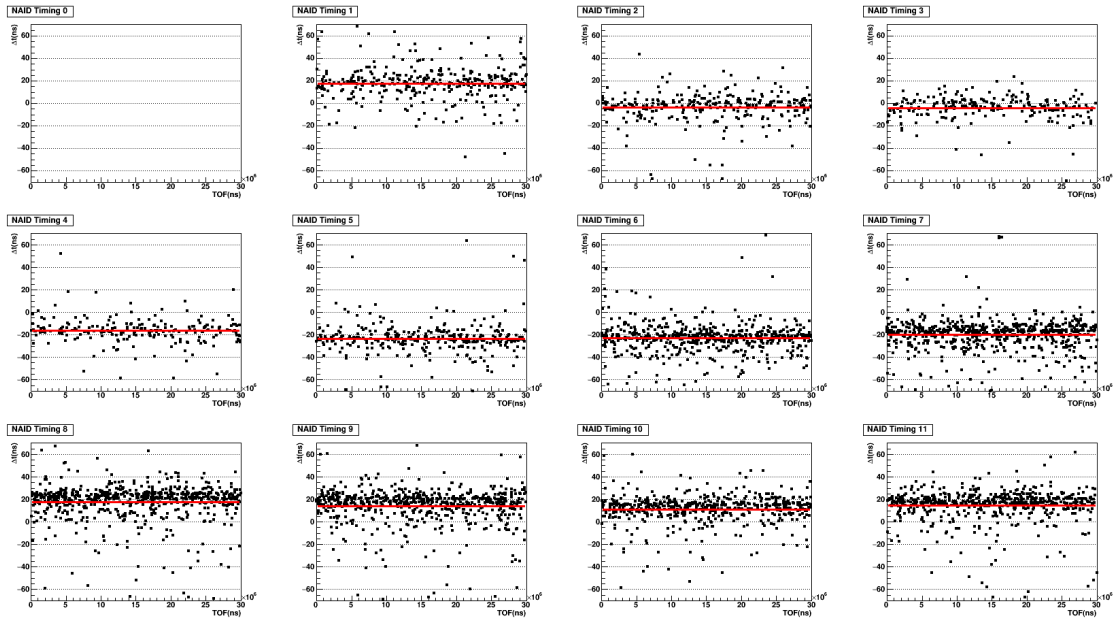

Figure 6.11: NaI(Tl) detector offset distributions (relative to NaI(Tl) #0). Achieved by measuring a γ-ray emission in ^{60}Co in NaI(Tl) #0 and finding the closest timestamp γ ray detected in another detector, the amplitudes of both γ rays detected have not been correlated.

identification for the data acquisition card to which the detector was connected. A clear correlation can be seen between DAQ card and NaI(Tl) timing offsets, with minor fluctuations between detectors on the same card. This makes sense as each card clock is only roughly calibrated to the other, giving rise to these small, but significant, differences. The sources used in this instance were two of the same sources used in the energy calibration procedure, i.e. ^{88}Y , and ^{60}Co.

To demonstrate the effect of these fluctuations Figures 6.14 and 6.15 demonstrate a timing distribution of the NaI(Tl) array before and after this offset correction, respectively. The improvement upon the resolution of the distribution is immediately apparent, as this correction removes the three separate peaks and produces a smoother single peak. This plays a crucial role in the analysis as is shown in the *"Detector Time Spreads"* section of Chapter 8. To the side of the main peak in Figure 6.15 there are features of the timing spread not part of the main peak but above the background level. These are due to neutrons which are scattered by the ^{235}U target rather than fissioned; some of these scattered neutrons will reach a NaI(Tl) detector and generate a signal, causing this effect in the data.

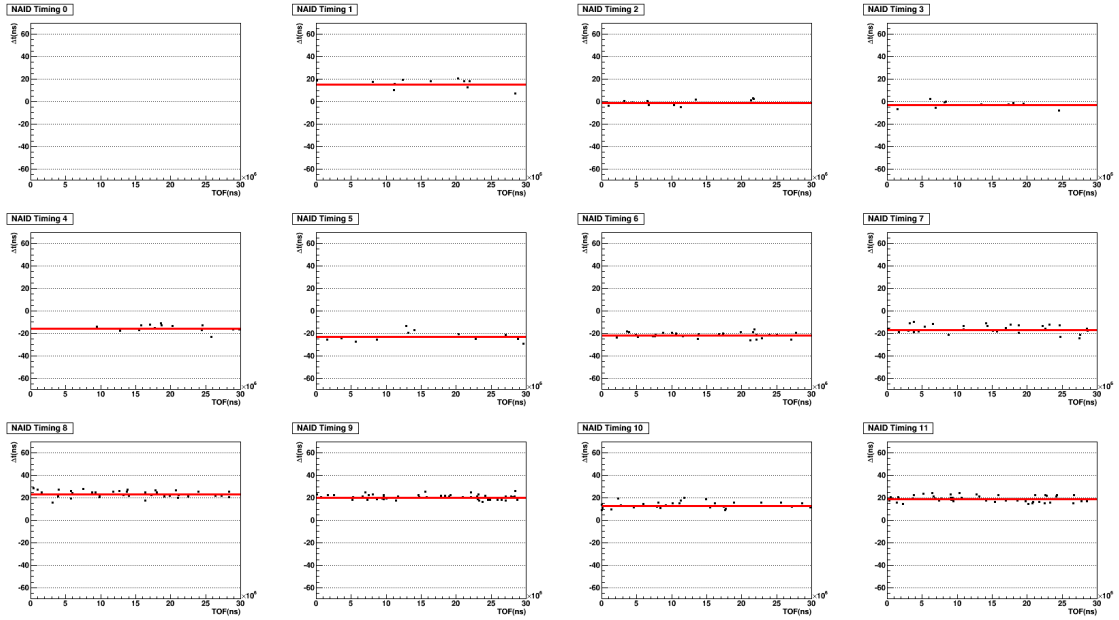

Figure 6.12: NaI(Tl) detector offset distributions (relative to NaI(Tl) #0). Similar to the previous figure this has been achieved by looking for detector signals with adjacent timestamps, however Amplitude Correlation has been performed between the signals, i.e. for ^{60}, if NaI(Tl) #0 detects a γ ray with 1173 keV of energy, a signal with 1333 keV energy is searched for within the other detectors in the array. This is the cause of the dramatically reduced statistics present in the figures.

NAID #	Mean Offset(ns)	DAQ Card
0	0.000 ns	M2 C1
1	17.953 ns	M2 C1
2	-1.956 ns	M2 C2
3	-2.777 ns	M2 C2
4	-15.888 ns	M4 C0
5	-23.399 ns	M4 C0
6	-21.151 ns	M4 C0
7	-16.395 ns	M4 C0
8	22.623 ns	M5 C0
9	19.727 ns	M5 C0
10	13.665 ns	M5 C0
11	18.361 ns	M5 C0

Table 6.2: Mean offset for each detector, taken by averaging the offsets projected onto the time axis. Within the DAQ Card column, M refers to the DAQ machine within which the card sits and C refers to the card ID number in that machine.

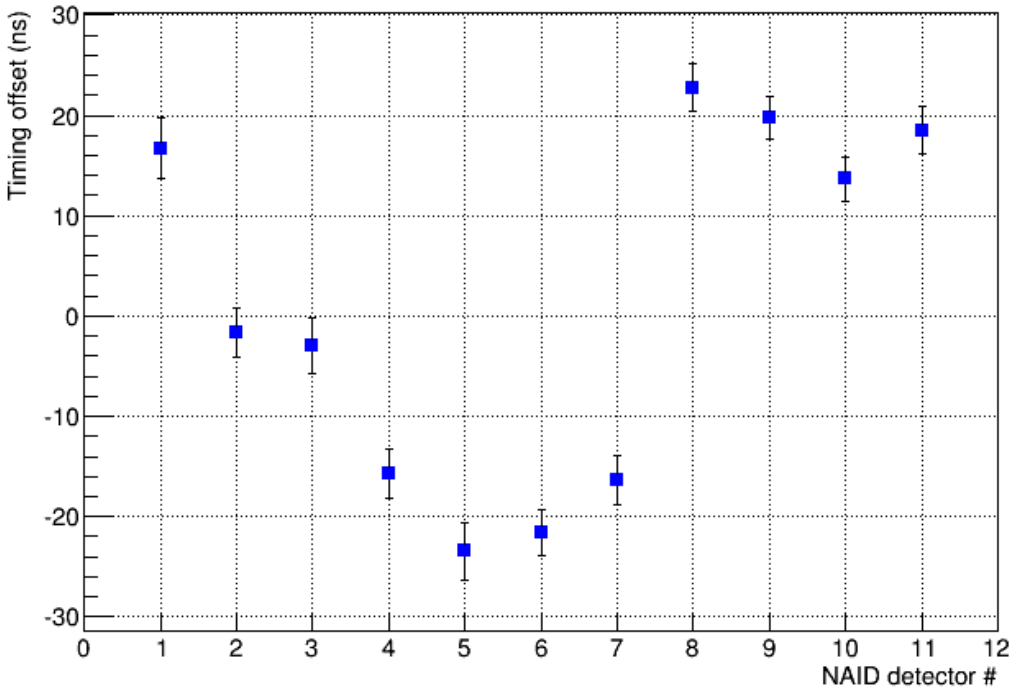

Figure 6.13: Average of offset distribution for each NaI(Tl) detector, for the Amplitude Correlated data. These data are from the average, and standard deviation, determined in Figure 6.12.

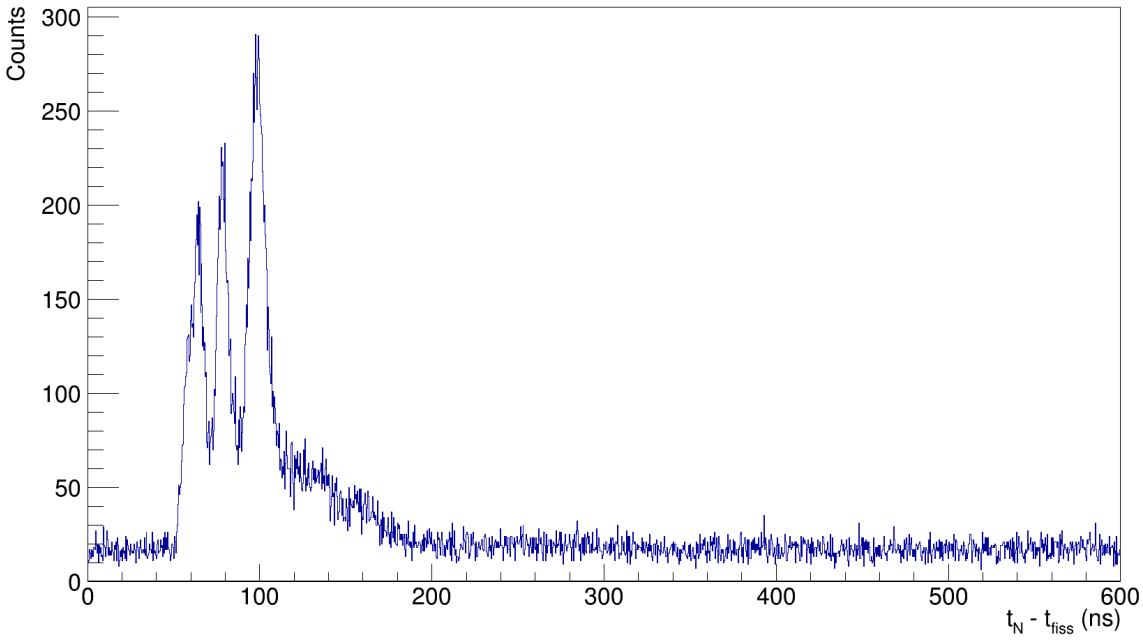

Figure 6.14: Timing spread from NaI(Tl) detector signals to fission timestamps – non-corrected for timing offset. These data are from the measurement of ^{235}U (n,f). This is calculated by subtracting the timestamp of a fission event within STEFF from the timestamp of a γ ray detected in a NaI(Tl) detector. The need for timing calibration is immediately apparent, as there exist three separate peaks instead of the expected single peak.

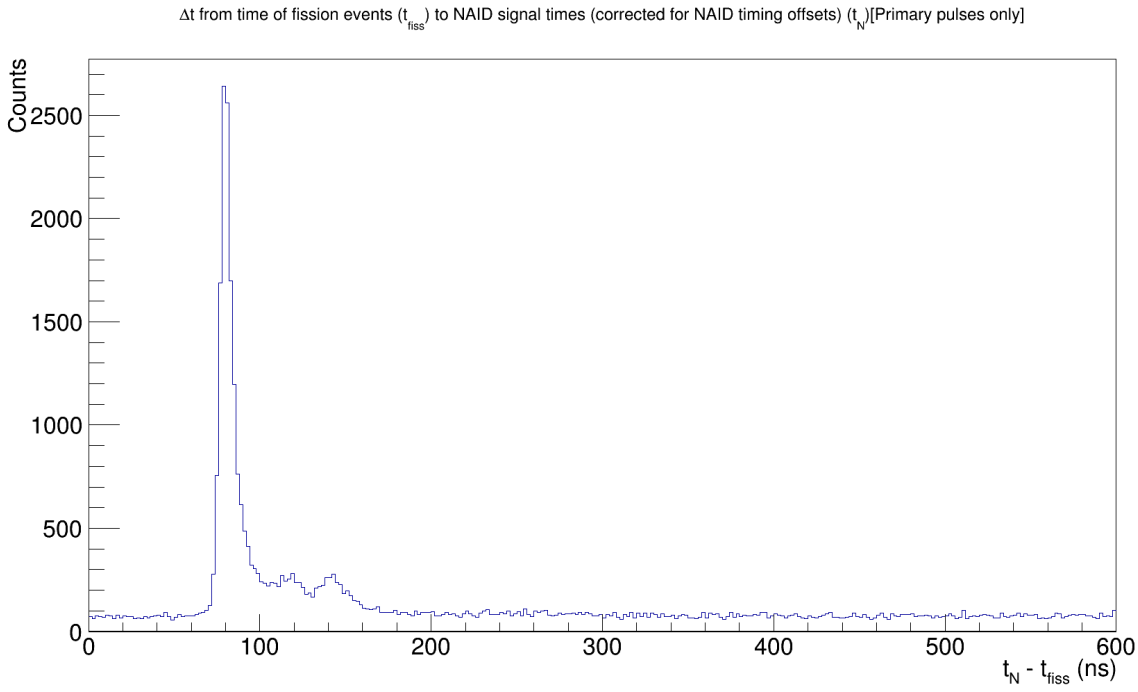

Figure 6.15: Timing spread from NaI(Tl) detector signals to fission timestamps – corrected for timing offset. These data are from the measurement of ^{235}U (n,f). Determined via the same method as the previous figure, with the addition of the NaI(Tl) timing offset correction factor determined in Table 6.2. The expected single peak is now clear, along with a small, above-background, feature to the right of the peak. This can be attributed to neutron scattering from the target sample into the detector.

6.3.1 High Count-Rate Test & $LaBr_3$ Comparison

It must be confirmed that the scintillation detector performance is being maintained whilst experiencing the high count rates present during the experimental campaign. To verify this a high activity γ-ray source (a 3.3 MBq ^{22}Na source, in this instance) was utilised to gradually increase the count rate present within the NaI(Tl) and $LaBr_3$ detectors (by varying the separation distance between the source and detector). This experimental setup can be seen in Figure 6.16.

The effect of increasing the count rate present within the NaI(Tl) and $LaBr_3$ detectors can be seen in Figure 6.18. It can be seen that the resolution within the NaI(Tl) detectors the detection resolution falls slowly, however eventually such a count rate is reached that the photopeaks are no longer distinguishable. The detector can no longer measure deposited energies at such a count rate, as is demonstrated in Figure 6.20. In comparison, this effect is not as dramatic within the $LaBr_3$ detector, which maintains the ability to record a deposited energy spectrum with sufficient resolution as high as 1.4 counts per microsecond (this count rate was the highest achieved in the $LaBr_3$ detector with this experimental testing setup).

This suggests that whilst the NaI(Tl) detector retains the ability to detect that a γ ray has entered the crystal (as supported by the work underpinning Figure 6.8), the signal energy information when measuring at such dramatic count rates is not reliable. This would mean that for the higher count rate portions of the n_TOF experimental campaign (i.e. low time-of-flight region of the neutron beam, where there is still a large background rate) only the γ-ray fold information will be retrievable and the deposited energy cannot be used.

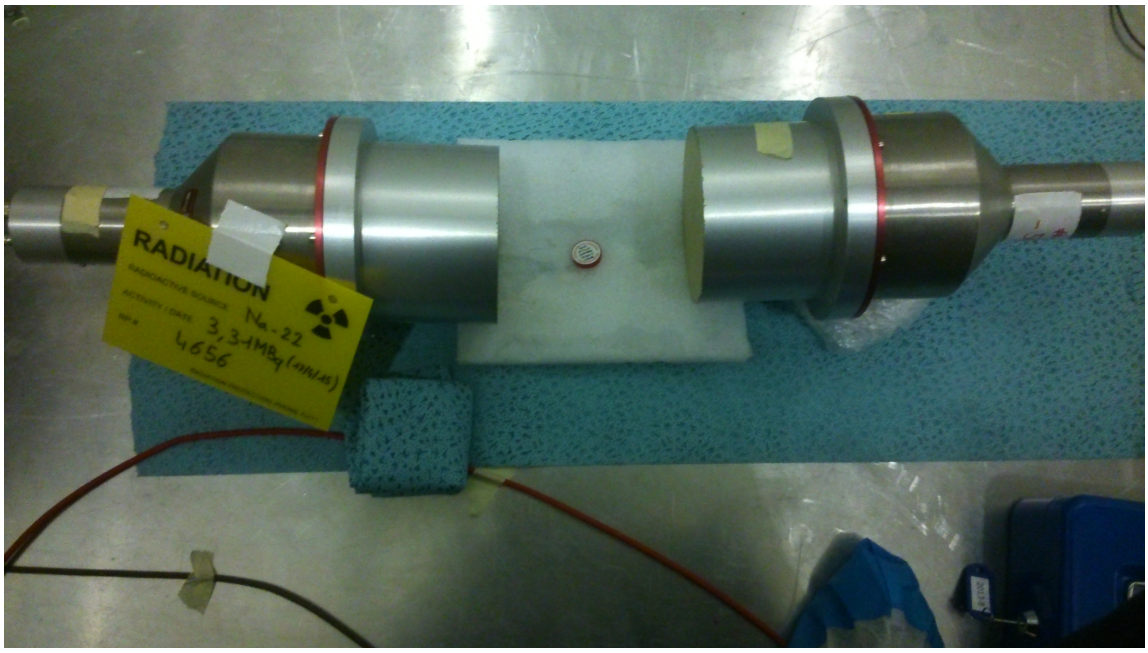

Figure 6.16: Experimental setup for high count-rate investigation into sodium iodide detectors. This setup consisted of two NaI(Tl) detectors measuring a Na-22 γ-ray source. A single $LaBr_3$ scintillator (Figure 6.17) was later added.

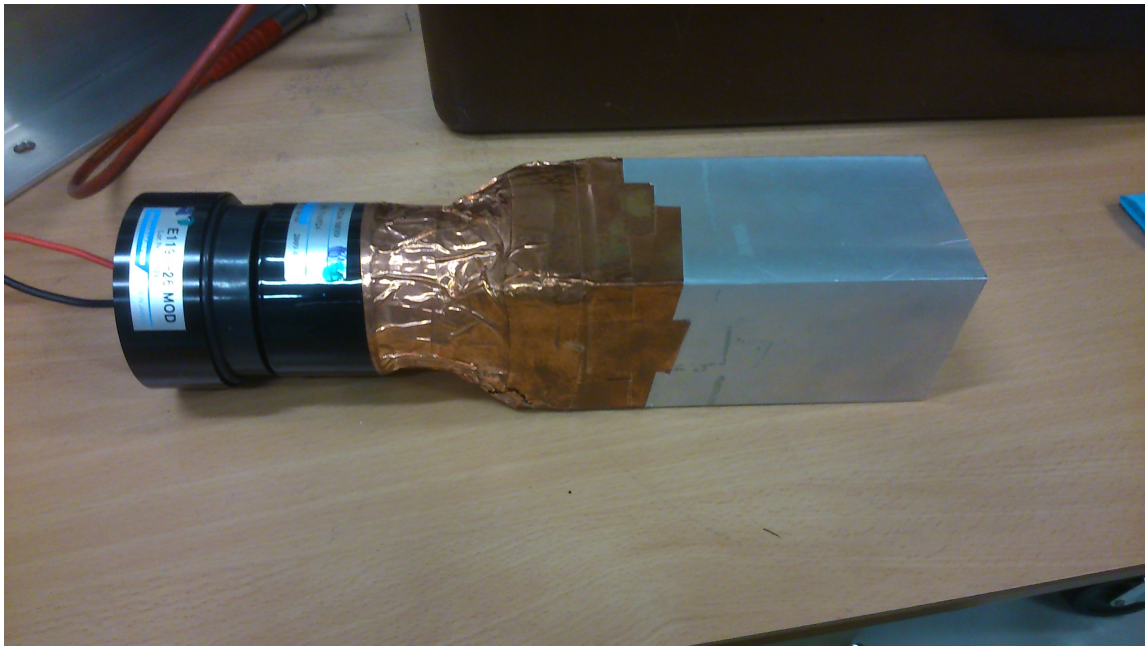

Figure 6.17: The $LaBr_3$ detector used in the high count-rate investigation and phase two of the experimental campaign.

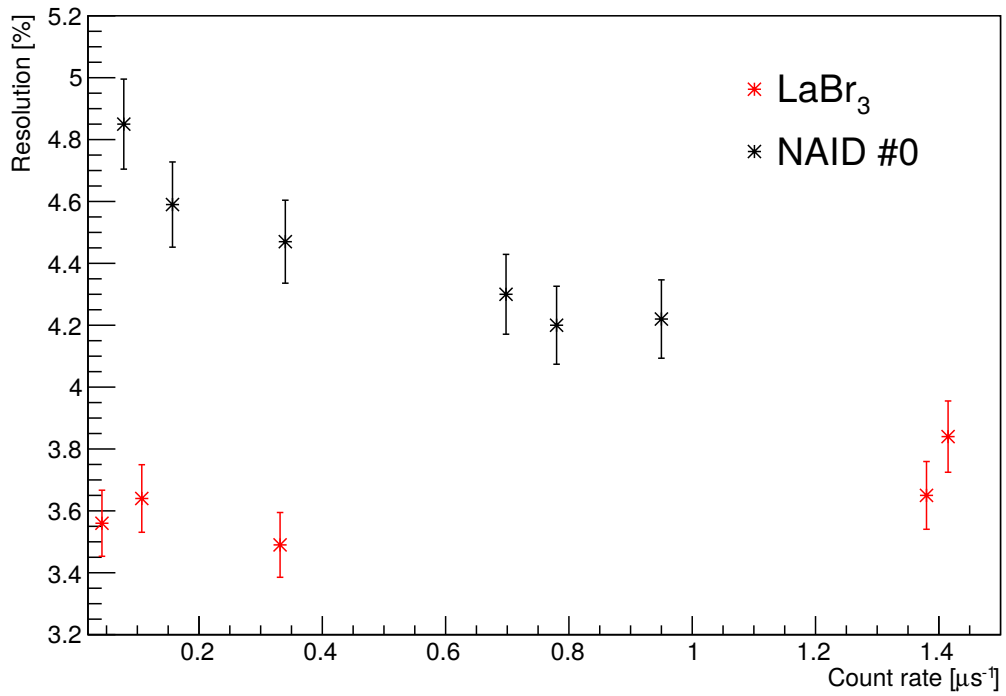

Figure 6.18: Detector resolution dependency upon count rates within one of the NaI(Tl) detectors and the $LaBr_3$ detector. Determined by using a ^{22}Na source and varying the distance from the source to the detector faces, then measuring the resolution of the 1275 keV signal peak. Count rates ranged from 100 kHz to $>$ 1.5 MHz.

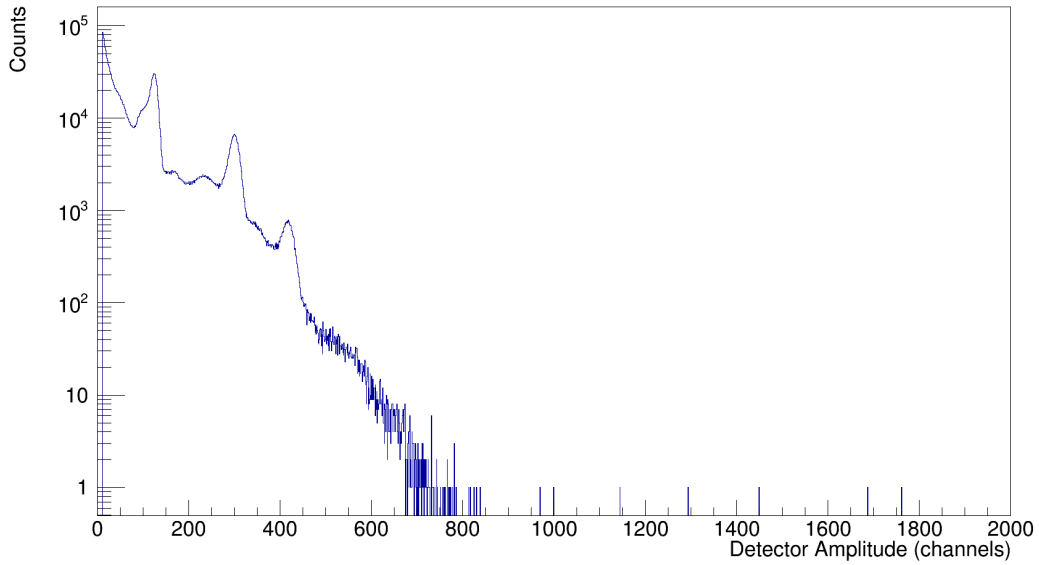

Figure 6.19: The deposited energy spectrum of one of the NaI(Tl) detectors when subjected to a rate of approximately 0.7 counts per microsecond. At this count rate the photopeaks of the ^{22}Na source are still readily discernable.

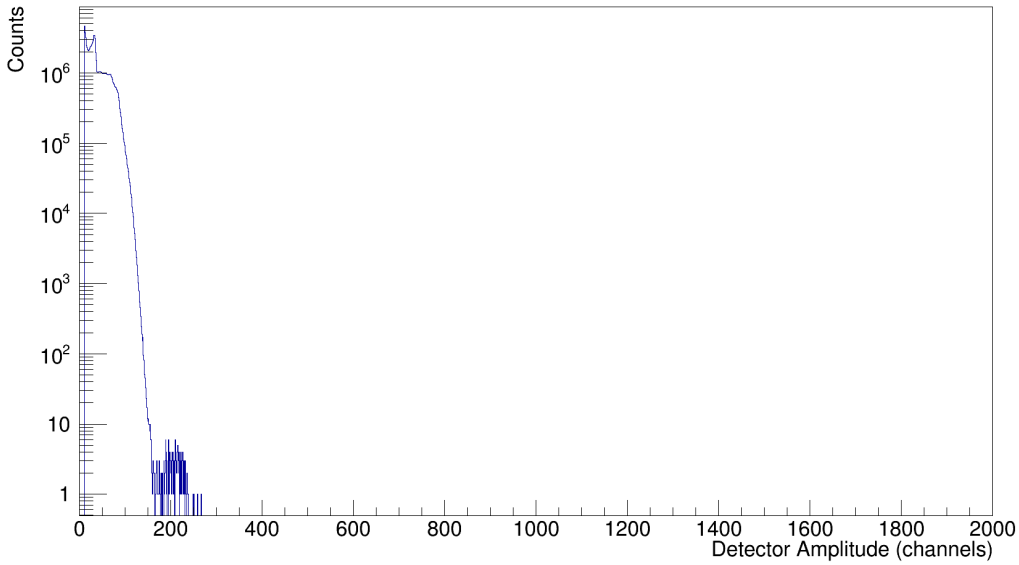

Figure 6.20: The deposited energy spectrum of one of the NaI(Tl) detectors when subjected to a rate of 1.75 counts per microsecond. Compare with the previous spectrum (Figure 6.19) at a lower rate and it can be seen that for higher rates the photopeaks in question are no longer discernable.

7

Experimental Campaign

The experimental campaign is divided into two distinct phases, with some experimental adjustments in between. Experimental Phase 1 began in October 2015 running for approximately 2 months. Phase 2 then began in June 2016, this time for approximately 1 month. Due to the complex nature of STEFF (demonstrated in Figure 7.1) there was also a week required before and after each experiment to transport, set up and calibrate STEFF within the experimental hall.

7.1 Experimental Phase 1 - Winter 2015

Due to the development work required to optimise STEFF for the upcoming experimental campaign (see Chapter 6 and [65]), STEFF arrived at CERN in April 2015 where it was assembled, modified, and tested within a "pre-experiment" area (B272 of CERN). Following these preparations STEFF was moved into the experimental hall of EAR2 in October 2015 and was brought to a suitable experimental condition over the course of a week. Power supply cables, data transmission cables and gaseous pipework needed to be set up appropriately and the vacuum/gas system of STEFF primed accordingly. Additionally, all detectors were brought to the appropriate voltage (voltages listed in Table 7.1).

Correct alignment of STEFF with the neutron beam is essential to prevent/minimise the neutron beam interaction with structural components of STEFF. Such interactions would

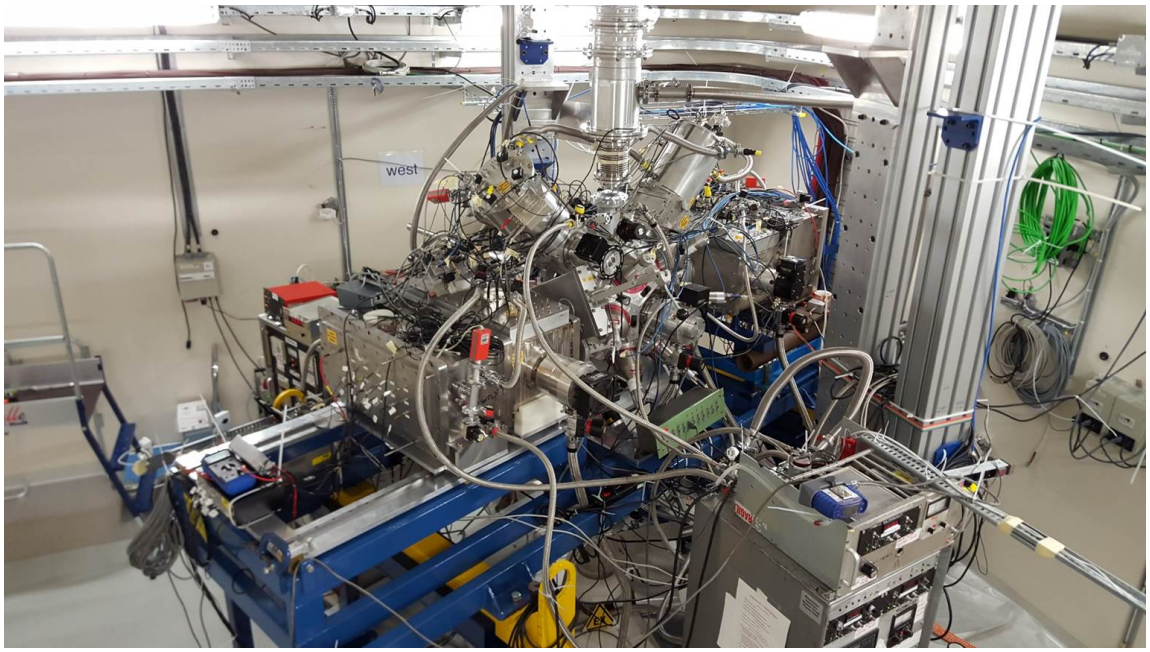

Figure 7.1: Photograph of STEFF setup within the n_TOF EAR2 experimental hall; electronic cabling and gas pipework can be seen surrounding STEFF.

Table 7.1: A list of the operational voltages for the various components of STEFF. Those entries containing "$\sim$" represent operational voltages whose values varied over the course of the experiment or, in the case of NaI(Tl) detectors, on a detector-by-detector basis.

Component	Voltage (V)
NaI(Tl) #0 - #11	-530 $\sim$ -690
Start Detector MCPs	-1800 $\sim$ -2000
Start Detector Mirrors	-4000
MWPC Detectors	+660 $\sim$ +690
BRGG FSRs	+1250
BRGG Anode	+1250
HIPS FSR	+850
HIPS Anode	+850
FiFI Frisch Grids	+1000
FiFI Anodes	+1200
High Voltage Electrostatic Mirrors (STOP detector mirrors)	+18000

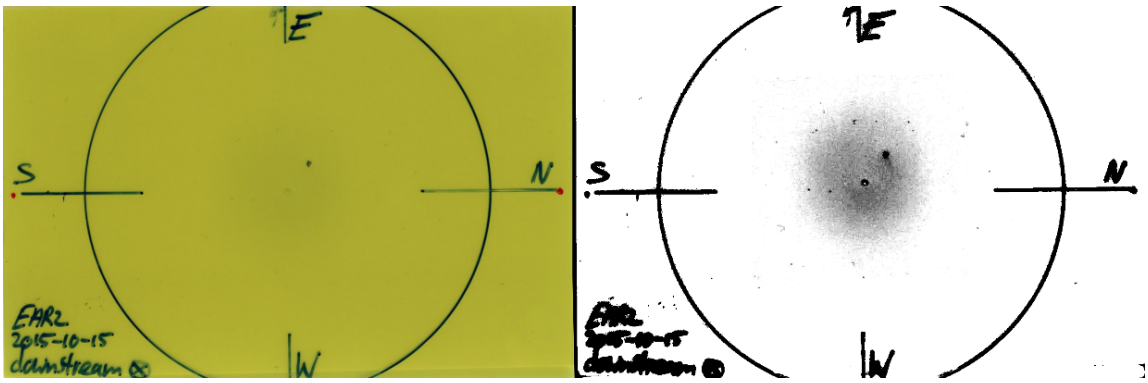

Figure 7.2: An example of a gafchromic film after a single night of beam exposure, along with alignment key drawn upon the surface. The right hand image shows the same film after it has undergone processing using image manipulation software in order to make the irradiated region more apparent [65].

cause a large increase in the background rate experienced within the NaI(Tl) detectors due to γ ray creating processes ((n,γ)) or within other detectors from charged particle creating reactions ((n,p), etc.). STEFF was initially coarsely aligned by sight and subsequently several sheets of gafchromic film were used to check this alignment. Gafchromic film is a radiation sensitive film coated on a polyester base, this film darkens upon impingement of large deposits of radiation (but does not react to room-light, as such could be utilised easily without requiring a dark room or other special measures) [80]. These films were placed in three locations: after the exit window of the neutron beam at the base of EAR2 (post second collimator), the STEFF entrance window at the underside of the detector and the STEFF exit window on top of the STEFF detector. By inspecting and comparing the three films (an example of an irradiated gafchromic film can be seen in Figure 7.2) a fine adjustment in the alignment of STEFF in both the X-Y plane and the Z-axis was carried out.

Data Acquisition Setup

Each of the detectors within STEFF outputs a signal to the n_TOF DAQ (see Section 3.1.2), a summary of the DAQ settings for each detector can be found in Table 7.2. The time window for data taking for all channels was 30 ms. A short time into phase one of the experiment there arose severe problems with several of the DAQ cards and this re-

Table 7.2: The channel configuration for the n_TOF DAQ at the beginning of Experimental Campaign Phase One. Where two values are quoted for sampling rate that is due to the detectors in question being split over multiple DAQ cards, with some cards at different sampling rates than others.

Detector and Detector ID	Sample Rate (MS/s)
NaI(Tl) Detectors (NAID #0-11)	450.0 / 1800.0
Start Detector (STRT)	1800.0
MWPC/Stop Detectors (MWPC #1-5 & #11-15)	900.0 / 1800.0
HIPS Anodes (HIPS #1-15)	112.5
Bragg Anodes (BRGG #1-15)	112.5
FiFI Brgg Anode (FIAB)	225.0
FiFI Brgg Frisch Grid (FIFB)	225.0
FiFI Hips Anode (FIAH)	225.0
FiFI Hips Frisch Grid (FIFH)	225.0
FiFI Brgg Start Detector (FISB)	1800.0
FiFI Hips Start Detector (FISH)	1800.0
Beampickup detector (PKUP)	1800.0

quired a reconfiguration of the DAQ. However, the parameters stipulated within Table 7.2 still apply after the reconfiguration. Details of the nature of the DAQ issues are discussed in Section 7.1.1.

Experimental Phase 1 Target

During phase one of the experimental campaign the narrow collimator setup of EAR2 allowed the use of a small diameter target (see Figure 7.3). This target consisted of a 33 mm diameter sample of 99.9% enriched ^{235}U with a surface density of 300 μg cm^{-2}. This sample was provided courtesy of the n_TOF team. This sample was placed within the central chamber of STEFF and oriented at an angle (to the horizontal axis of STEFF) of $\phi_{target} = 21^{\circ} \pm 2^{\circ}$. This angle was carefully chosen as a balance between maximisimg the target-beam coincident surface area and minimising the distance any fission fragments must pass through the target structure before reaching the detectors within STEFF (a phenomenon known as 'straggling' which lowers the energy and timing resolution achievable by STEFF). Care must also be taken with such a small target such that the target holding material remains out of the majority of the beam flux, as this would produce a lot of unwanted background signals.

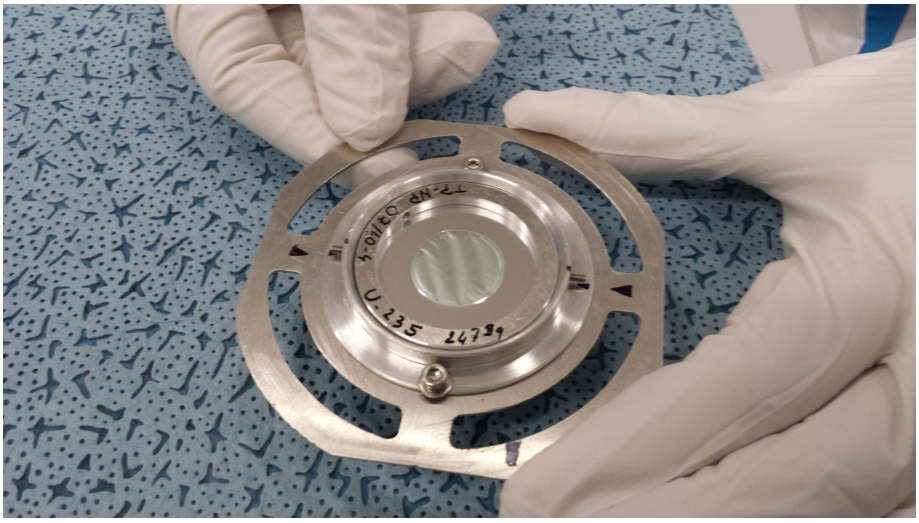

Figure 7.3: The U-235 target used in phase 1 of the experimental campaign. The uranium is the green tinted material in the centre of the target holder. This is a 33 mm diameter sample with a surface density of 300 μg cm^{-2}. The uranium is in metal form with a 99.9% U-235 enrichment.

7.1.1 Experimental Challenges Encountered

During phase one of the experimental campaign, several unexpected challenges were encountered. These challenges did not entirely compromise the experiment but did reduce the effectiveness. The most severe of these problems were those surrounding the n_TOF data acquisition system. Twelve of the sixty DAQ channels available in EAR2 failed due to issues with memory buffers within the data cards. These twelve channels were on three older, less robust data cards which meant that only the twelve channels were affected. In the original DAQ configuration these channels were connected to the twelve NaI(Tl) detectors, however upon the DAQ failure being revealed the NaI(Tl) detectors were switched onto other data cards and twelve channels from the BRGG and HIPS ion chambers removed from the DAQ (six from each). The six channels removed were the left-most and right-most columns of three from each detector. These anodes subtend the smallest solid angle against the uranium target and so should affect the rate less than removing the more central anodes. This reduced the rates and efficacy of the ion chambers a minor amount but was necessary as without the NaI(Tl) detectors there is no method of detecting γ rays.

A further issue with the DAQ was due to the volume of data which was produced by the STEFF experiment. STEFF utilises a large number of channels and for many of these channels there is no possibility to perform zero-suppression on the data (see Section 3.1.2). The reason for this is twofold; firstly, the ion chamber anodes need to be sensitive to the smallest signals in order to fully characterise the energy of a fission fragment (due to induced signals in neighbouring anodes) and thus rejection of small signals is impossible. Secondly, many of the detectors were exhibiting a lot of noise (mainly a 50 Hz induced oscillation, along with a $\sim$1.1 kHz noise in some detectors) and this meant that assigning a suitable signal threshold would be impossible. Due to this inability to reduce the amount of data being taken the DAQ was put under great strain and it resulted in persistent crashing and complete DAQ resets were often required. The volume of these data also greatly increased the processing time between raw data signals and usable data outputs.

A physical issue was also encountered with the use of isobutane gas within STEFF. The gas supply cabinet for n_TOF is housed outside of the experimental hall, and outdoor temperatures reached a sufficiently low level such that the isobutane began to condense within the gas lines leading to a lack of functioning within any of the gas detectors of STEFF. To remedy this problem the entirety of STEFF and the gas lines leading up to STEFF had to be flushed of liquid isobutane and the pressure of the gas lines adjusted such that a phase change from gas to liquid would no longer occur at the temperatures being reached. This operation took several days and in that time CERN went into its winter shutdown, which meant that no more proton pulses would be received at n_TOF and the ^{235}U portion of phase one had to end.

The combination of these issues resulted in approximately a $\sim$38% reduction in usable statistics from this measurement (1.36×10^{18} usable protons on target out of a total of 2.2×10^{18} protons on target).

Calibration

Once the ^{235}U portion of phase one was complete, several calibration measurements were performed whilst STEFF remained in the experimental area and the n_TOF DAQ was still accessible. The calibration sources used were ^{252}Cf as a fission source for calibrating the fission fragment detectors and several γ-ray sources used to calibrate the NaI(Tl) detectors (see Section 6.3). The conditions of the ^{252}Cf calibration were sub-optimal. As there is no way to trigger the n_TOF DAQ upon detection of a fission fragment, the only option is to use the beam trigger (as is used within the ^{235}U portion of the experiment) or calibration trigger, which automatically triggers every 2.4 seconds. Since the DAQ time window is finite (30 ms) this results in an up-time efficiency of approximately 1.25%, thus drastically reducing the usable activity of the fission fragment source. The californium source in question was a 200 kBq source. The branching ratio for spontaneous fission of this source is 3.09% [81], thus as a fission source the activity is 6180 fissions per second. Combining this with the geometric efficiencies and detector efficiencies within STEFF, then a further reduction due to this up-time efficiency the calculated rate of fission fragment detection during californium calibration is approximately 5 fissions per calibration trigger ($\sim$1.25 per ion chamber).

7.2 Experimental Phase 2 - Summer 2016

During the winter shutdown of CERN and the months prior to experimental phase two the STOP detectors of STEFF were subject to an upgrade, as detailed in [65]. Additionally, prior to phase two of the experimental campaign, the narrow second collimator previously used at n_TOF was replaced for the duration of this experimental phase by a wider aperture collimator (see Section 3.1.1). This wider aperture collimator resulted in a much wider beam profile and subsequently more neutron flux integrated across the X-Y plane. Due to this, the target used in phase one was no longer suitable, as it would have resulted in far too much unwanted material within the path of the neutron beam. Thus a wider target was

used.

Another change in the setup of STEFF was the replacement of a single NaI(Tl) with a Lanthanum Bromide ($LaBr_3$) scintillation detector. This $LaBr_3$ detector is a much faster detector, the decay constant is of the order 20 ns for $LaBr_3$ compared to the order of 250 ns for NaI(Tl) scintillators [82]. The $LaBr_3$ unit used is also much smaller and thus less susceptible to the γ ray and neutron background within the experimental hall. This smaller detector however does also lower the geometric efficiency of the detector when it comes to measuring the desired γ rays emitted from the experimental target. A comparison of this $LaBr_3$ detector with a NaI(Tl) is discussed in Section 6.3.1.

Experimental Phase 2 Target

The target used in phase two (see Figure 7.4) was especially commissioned for use in this experiment with STEFF. The properties of this second target are much more suitable than the target used in the previous phase. This second target is 81 mm in diameter, composed of 93% enriched UO_2 with a surface density of 100 μg cm^2. This is much thinner than the previous target and therefore the straggling phenomenon is less of an issue. The sample is deposited upon a 0.7 μm thick aluminium foil backing, which is also much thinner than the previous target. The 7% impurity is primarily due to the presence of uranium-238 [83], which, due to its substantially lower fission cross-section, does not pose too great an issue at energies below $\sim$1 MeV and remains an order of magnitude lower above this energy. At lower energies, uranium-238 has a large capture cross-section, however this will not present an issue as such an interaction will not trigger the required coincidence detection of fission fragment and γ-ray detection.

Due to the larger target and larger target holding apparatus, the target was able to be held at a more favourable angle (45°) to minimise fission fragment straggling. Once again the uranium-deposited side was positioned facing the BRGG detector arm. This positioning, however, drastically reduces the efficiency of one of the FiFI arms. Due to issues with the FiFI HIPS arm in Phase 1 of the experimental campaign this was the arm

chosen to see a reduction in efficiency. Using this more favourable angle again required

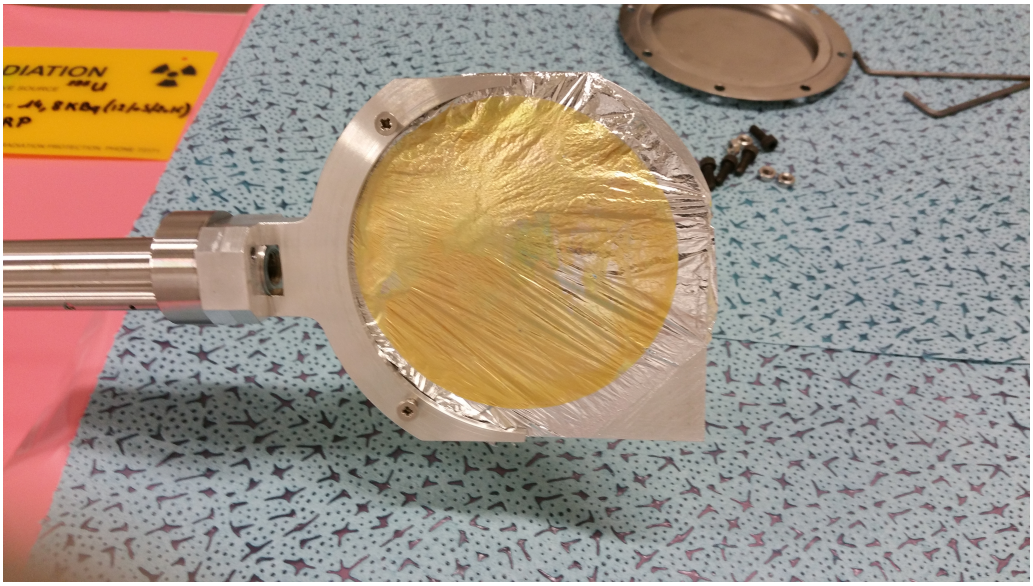

Figure 7.4: The U-235 target used in phase 2 of the experimental campaign, situated within the arm of the target holding mechanism of STEFF. This is a 81 mm diameter target with a surface density of 100 μg cm^2. It is composed of uranium dioxide (UO_2), with the uranium enriched to 93% U-235 content.

precise alignment of STEFF with respect to the neutron beam in order to maximise the target-beam intersection area. This was again carried out using an initial visual coarse alignment followed by fine adjustment in response to gafchromic film measurements.

7.2.1 Phase 2 DAQ Modifications

One of the major differences between the two experimental phases is not a change with regards to STEFF but a change in how the n_TOF DAQ operates. During the winter shutdown and the months prior to experimental phase two, a concerted effort was carried out in order to better optimise the DAQ so as to avoid the errors encountered previously (namely the overly large data size). For these experiments the only data of interest are those data related to fission events, but during these events it is vital to record all data from all detectors to ensure a complete picture. Thus the standard n_TOF zero suppression algorithm is not suited to such a task. Instead a so-called "*second level trigger*" system was implemented. This consisted of a master-slave relationship being established between the

detectors of STEFF, and if any master channel was triggered all other channels (i.e. slaves) would begin recording for the specified duration. This is made slightly more complicated in the case of STEFF as it is required that should any of the fission fragment detectors (i.e. BRGG/HIPS/FiFI BRGG/FiFI HIPS) detect a signal then all detectors are required to commence reading data. Fortunately it was not necessary to have every single BRGG and HIPS anode become master channels, as the presence of the Frisch Grid means that a signal will be generated on the Frisch channel whenever a fission fragment enters the respective ion chamber. There were four master channels on STEFF, corresponding to the four Frisch Grids present: BRFR, HIFR, FIFH, and FIFB.

Figures 7.5 and 7.6 show the set-up of the second level trigger circuit. The circuit is relatively straight forward and can be summarised in stages:

1. Signal – The signal out from the appropriate master channels (i.e. the Frisch Grid signals) are diverted from the DAQ into a linear FIFO.

2. Linear FIFO – A Linear Fan In/Fan Out splits the original signal into two identical signals, rerouting one back to the DAQ (so as to maintain the detection of the Frisch Grid signal) and the other one into the Spectroscopic Amplifier.

3. Spectroscopic Amplifier – This amplifies and shapes the Frisch Grid signals (typically slow signals with microsecond rise times) to create a usable trigger output for the later elements of the second level trigger circuitry. This shaped signal then proceeds to a Leading Edge Discriminator.

4. Leading Edge Discriminator – This discriminator enables the production of a single pulsed signal whenever the incoming signal is above the user-defined threshold, enabling later boolean logic.

5. Multiplicity Logic Unit – This unit will allow production of a signal under certain boolean trigger conditions. Due to the idiosyncracies of this particular unit the threshold is set at $N > 1$ (i.e. the unit triggers an output upon receipt of at least two signals). Because of this, a Coincidence Unit is employed to feed into the MLU a

constant single signal (and therefore any single Frisch Grid trigger would render the N > 1 condition true). The outgoing signal from the MLU then is routed to an Octal Gated Delay Generator.

6. Octal Gated Delay Generator – This unit enables the incoming signal to be copied multiple times over, as is necessary due to the requirement of four simultaneous master triggers.

7. Master trigger(s) – Four master triggers are sent from the Second Level Trigger circuit to the n_TOF DAQ, one to each individual DAQ computer.

This alteration necessitated a new DAQ setup to accommodate the newly devised master-slave relationship. Tables 7.3 through 7.6 outline the DAQ settings used throughout Phase 2 of the experimental campaign, as laid out on each individual DAQ machine. These updated configurations and master-slave detector suppression setups reduced the raw data volume from approximately 800 MB per pulse in experimental phase one to c. 80 MB per pulse in phase two. This represents a drastic reduction in data volume, despite the approximately tenfold increased fission rate anticipated from a larger target and larger neutron beam, demonstrating the great success of the second level trigger implementation.

Phase 2 Calibration

Once again STEFF was required to undergo calibration. Due to the issues outlined previously regarding using a californium source for calibration, this time a fission source was not used. The NaI(Tl) (and $LaBr_3$) detectors were calibrated using the sources ^{88}Y, ^{60}Co, and ^{137}Cs. Due to time constraints the AmBe and CmC sources used in the calibration during phase one were not able to used. However the previous calibration results (see Section 6.3) indicate that the NaI(Tl) detectors remain linear up to the high energies corresponding to γ rays from these two additional sources and thus extrapolation from the three γ-ray sources used in phase two calibration should not represent a problem.

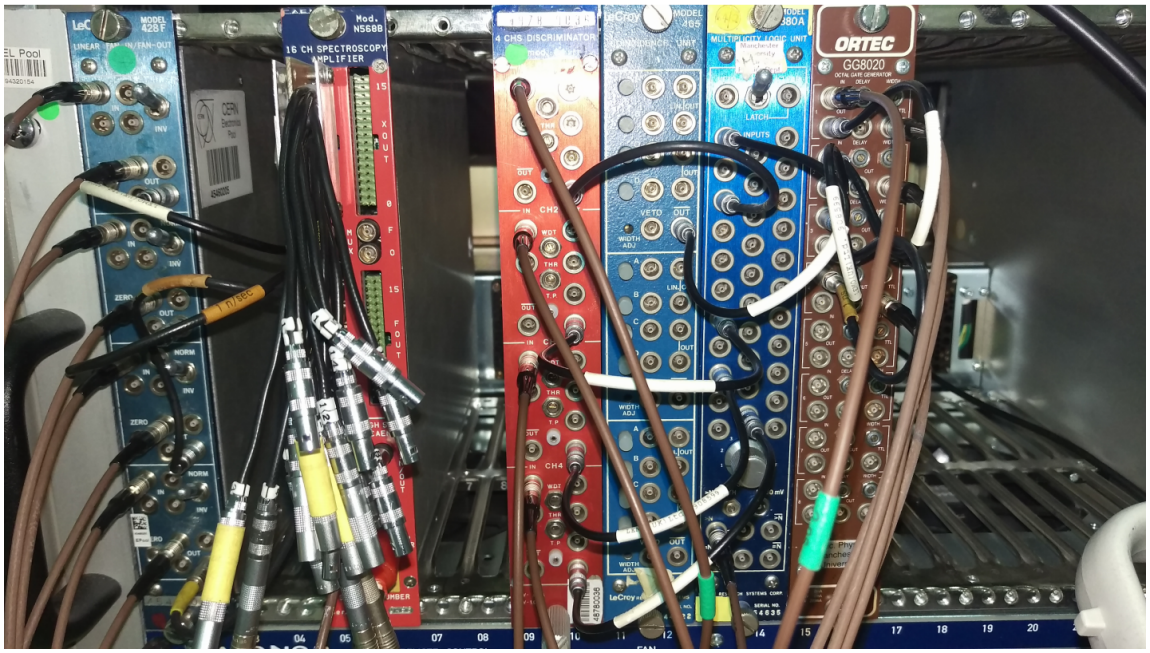

Figure 7.5: The analogue electronics setup within EAR2 DAQ rack area, designed to take input from several detectors and inject a logic pulse to several DAQ channels, prompting the system to record. From left to right: Linear Fan-in/Fan-out, Spectroscopy Amplifier, Linear Discriminator, Coincidence Unit, Multiplicity Logic Unit and an Octal Gate Generator. See Figure 7.6 for the circuitry schematic.

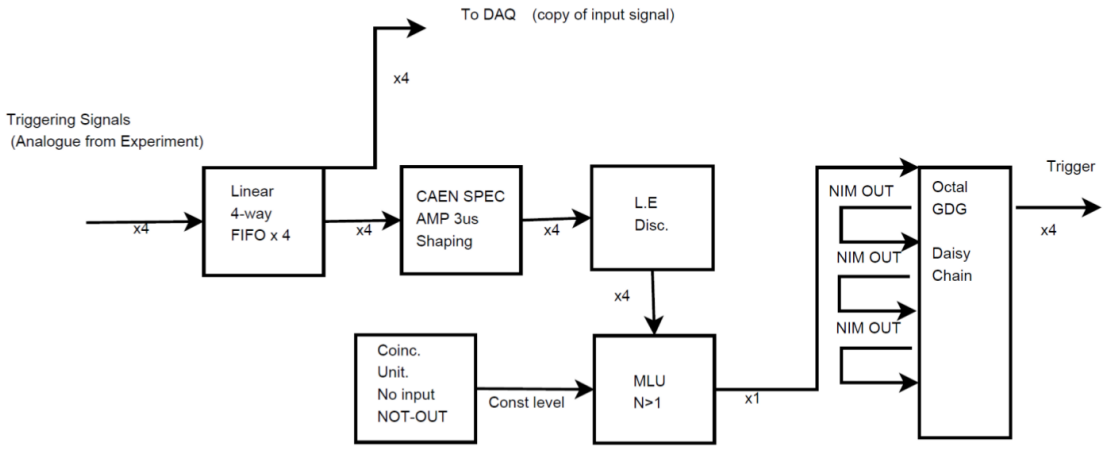

Figure 7.6: Schematic diagram of the '2nd level trigger' analogue circuit used to reduce data size in experimental phase two. This setup takes a trigger signal from the experiment, then duplicates it and sends one copy of the original signal into the data acquisition and another into the trigger generating circuit. The trigger circuit consists of a shaping amplifier, a leading edge discriminator and a pair of logic units which will produce a digital "ON" pulse to the data acquisition system upon receipt of the original trigger.

Table 7.3: The DAQ Configuration for Machine 1 during Experimental Phase Two.

Detector Name & ID	Sampling Rate (MS/s)
Master Trigger (MSTR #1)	1800.0
Start Detector (STRT)	1800.0
MWPC Detectors (MWPC #1-5 & #11-15)	1800.0
HIPS Ion Chamber Anodes (HIPS #28-30)	112.5
HIPS Frisch Grid Signal (HIPF)	112.5

Table 7.4: The DAQ Configuration for Machine 2 during Experimental Phase Two.

Detector Name & ID	Sampling Rate (MS/s)
Master Trigger (MSTR #2)	1800.0
FiFI BRGG Start Detector (FISB)	1800.0
HIPS Ion Chamber Anodes (HIPS #16-27)	112.5

Table 7.5: The DAQ Configuration for Machine 3 during Experimental Phase Two.

Detector Name & ID	Sampling Rate (MS/s)
Master Trigger (MSTR #3)	1800.0
FiFI BRGG Ion Chamber Anode (FIAB)	1800.0
Pickup Detector (PKUP)	1800.0
NaI(Tl) Detectors (NAID #0-2 & #3-11)	450.0
$LaBr_3$ Detector (LABR)	450.0

Table 7.6: The DAQ Configuration for Machine 4 during Experimental Phase Two.

Detector Name & ID	Sampling Rate (MS/s)
Master Trigger (MSTR #4)	1000.0
FiFI BRGG Frisch Grid (FIAB)	1000.0
BRGG Ion Chamber Anodes (BRGG #2-14)	125.0
BRGG Frisch Grid (BRFR)	125.0

8

Results & Discussion

This chapter focuses primarily on discussing the experimental analysis and subsequent results of experimental phase one, as described in Chapter 7.

8.1 Data Processing

The work performed to go from raw experimental data to meaningful results consisted of two major steps - *Processing* and *Analysing*. The reason for this distinction, and the important need for this *Processing* step, is made clear below.

Due to the high count rates of the scintillation detectors, and the fact that no zero-suppression could be used on the gas detectors (see Section 7.1.1 for details), the data files outputted are very large. For example, a run consisting of just under 1200 pulses (*run203720*, a relatively small run which was considered just large enough to use as a test bed to develop analysis routines) contained data trees of up to approximately 6e7 entries in length, with an overall file size of 2.3 Gb.

This presents an issue when trying to interface these files with analysis routines, as many parts of the routines used when analysing this data involve nested loops across the whole of the datafiles. When using nested loops with large numbers of data entries, it quickly becomes extremely time consuming – an attempt to apply this nested loop logic on one unprocessed run datafile (approx. 5000 pulses in size) was allowed to run for over

12 hours before it was forcibly interrupted and new methods sought.

Figure 8.1 shows the distribution of run lengths in terms of number of proton pulses, with a snapshot of those runs highlighted in Table 8.1. As can be seen the majority of these runs are actually much greater than *run203720* in length (the overall average being 3661 pulses). These runs will prove even more cumbersome to analyse unless further processed beforehand.

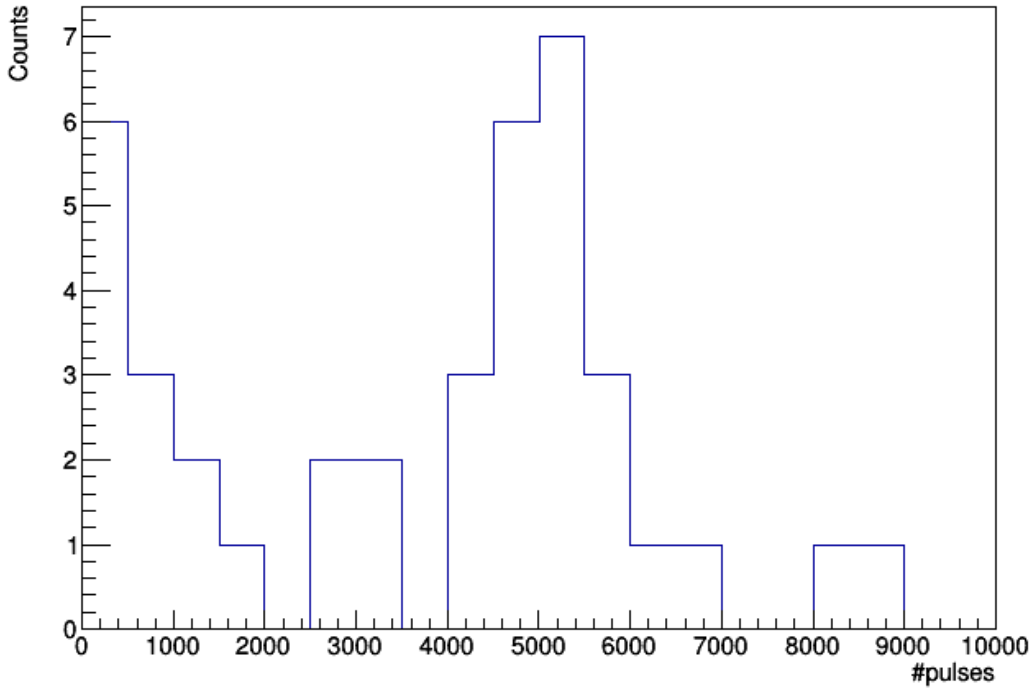

Figure 8.1: Distribution of number of proton pulses impinging upon the n_TOF lead target, in an individual experimental run in EAR2. Data as measured across Campaign Phase 1. Some runs detailed further in Table 8.1.

Run Number	**Number of Pulses**
203719	8467
203720	1189
203725	2505
203739	4871
203742	8513
203767	491

Table 8.1: Further details on a few of the results mentioned above. Note the wide range in run sizes that have to be considered.

The method for dealing with this (hereafter referred to as *Processing*), was to try and emulate on a software level the second-level trigger described in Section 7.2. This consisted of combing through the data trees corresponding to the ion chambers of STEFF and identifying signals large enough to be fission fragments. The timestamps of these signals were then stored in a two-dimensional array, with one dimension corresponding to the proton bunch number of the signals, this was in order to speed up processing time. At this point there exists a data bank of fission fragment detections (one 2D array per ion chamber data tree, four in all) ordered by their proton bunch number and their detection time. It is then relatively simple to cycle through the other detector data trees and find the difference in time between each signal and the closest fission event.

Then it is possible to apply a time cut on these data, and reject those entries which do not meet the selected criteria. Figure 8.2 demonstrates that the time between events in the *Start* detector and the *Bragg* detector ranges from approximately 3 to 6 microseconds. Since a fission event begins with the *Start* detector and ends with an ion chamber detector (e.g. the *Bragg* detector), this can be used as an appropriate time window. Note that this 3 to 6 microseconds does not correspond to the physical time of flight of a fission fragment traversing the length of a STEFF arm, which is much shorter, but is largely due to the slow rising signals generated within the fission ion chambers.

Applying this time cut reduces the data by up to a factor of approximately 500. The previously described data tree of close to 6e7 entries in *run203720*, after processing, was reduced to 7e4 entries; and from 2.3 Gb in size to 4.2 Mb. This means that the analysis routines used on these data can run on the order of minutes, rather than hours or even days.

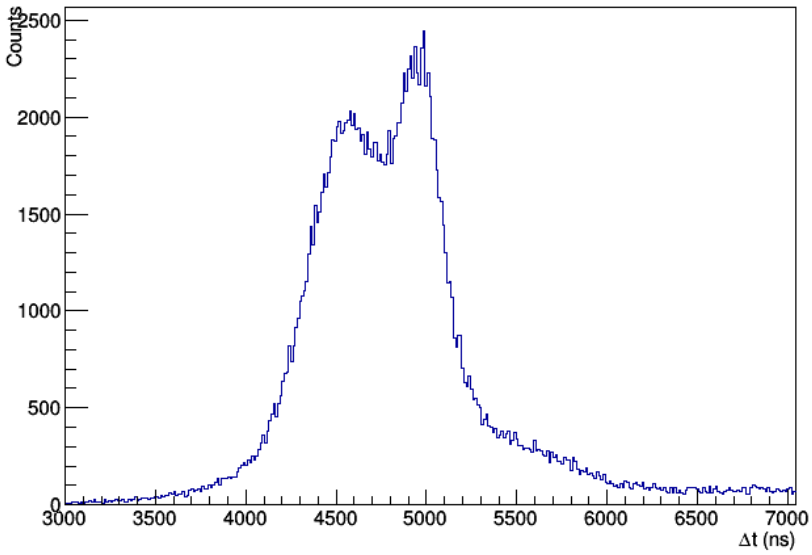

Figure 8.2: The time spread between signals detected in the STEFF *Start* detector and those in the STEFF *Bragg* detector. This covers the timespan of an event being detected within the *Start* detector (i.e. shortly after the time of fission) to the fission fragment being wholly deposited within the *Bragg* detector. Applying cuts which span the majority of the range of this distribution should capture the whole event for almost all fissions detected.

The *Start* and *Stop* detectors also exhibit a type of "echo" effect in their signals (see Figure 8.3 for an example). This is a characteristic effect of these detectors, and the routines which create the data trees from the raw signal traces identify each of these as separate signals (when in reality they are due to a single event). This must be compensated for, and the *Processing* routine has subroutines to clean these signals appropriately in order to further condense the datafiles and speed up later analysis. The way the subroutines achieve this is by looping through the data (after the trimming described previously has been applied), then isolating any signal groups consisting of a large initial signal followed by numerous smaller signals within a set "dead time", which the code user may vary at will. The largest signal within this group is then used as the true *Stop* detector signal.

Figure 8.3: Example of a single *Start* detector event, noting the main, large detection signal and subsequent rebounds.

An additional side-effect of the processing step is the introduction of a minimum γ-ray energy threshold for measurement. Due to the routines used at n_TOF, lower energy γ rays could not be accurate resolved from background signals and therefore a minimum γ-ray energy cut of 160 keV had to be applied to the measurements.

8.2 Gamma-ray Energies & Multiplicities

Once the data have been processed into a reasonable size format, following the description above, it is then a matter of extracting the appropriate information from them – in this case, the prompt fission γ-ray information. Ascertaining this information followed a multistep process which has been outlined via a flowchart in Figure 8.4. These are the steps referred to previous as *Analysing*. Each of these steps is described in further detail below.

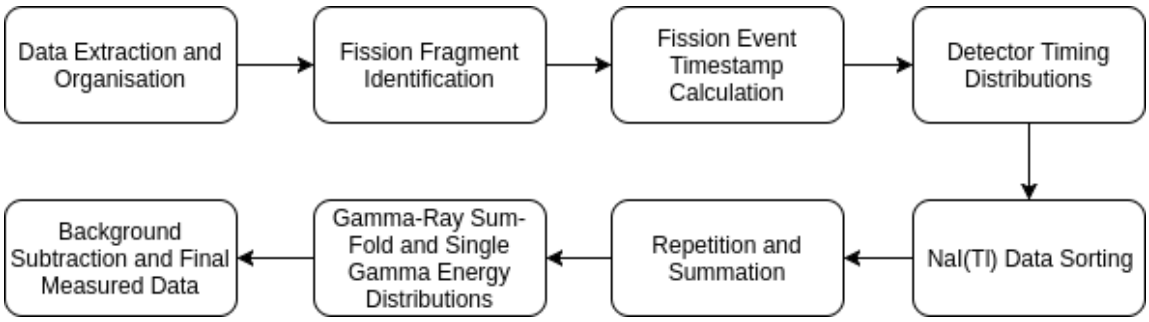

Figure 8.4: Flowchart outlining the major steps in the analysis routine to extract fission γ-ray information. These steps are described in further detail within the text.

8.2.1 Acquiring Detected Data

Data Extraction and Organisation

The initial step of organising data into two-dimensional vectors (similar to the method used for the *processing* routine described in Section 8.1) is a key step that drastically speeds up the analysis procedure by preventing inefficient looping over data which is not relevant to the proton bunch that is under analysis. Amplitude cuts are also applied at this stage to discriminate between false events (such as α particles, or spontaneous detector firing as described briefly in Section 4.2.2) and true potential fission fragment events.

Fission Fragment Identification

Once this data extraction and organisation has been carried out the code begins to look for coincident signals which may be fission fragment detections. There are four combinations of detector signals which could result from a single fission fragment, correlating to each fission detection arm, these are:

1. *Bragg arm - Start, Stop (Bragg side) and Bragg.*

2. *HIPS arm - Start, Stop (HIPS side) and HIPS.*

3. *FIFI Bragg - FIFI Start detector and FIFI ion chamber (both Bragg side).*

4. *FIFI HIPS - FIFI Start detector and FIFI ion chamber (both HIPS side).*

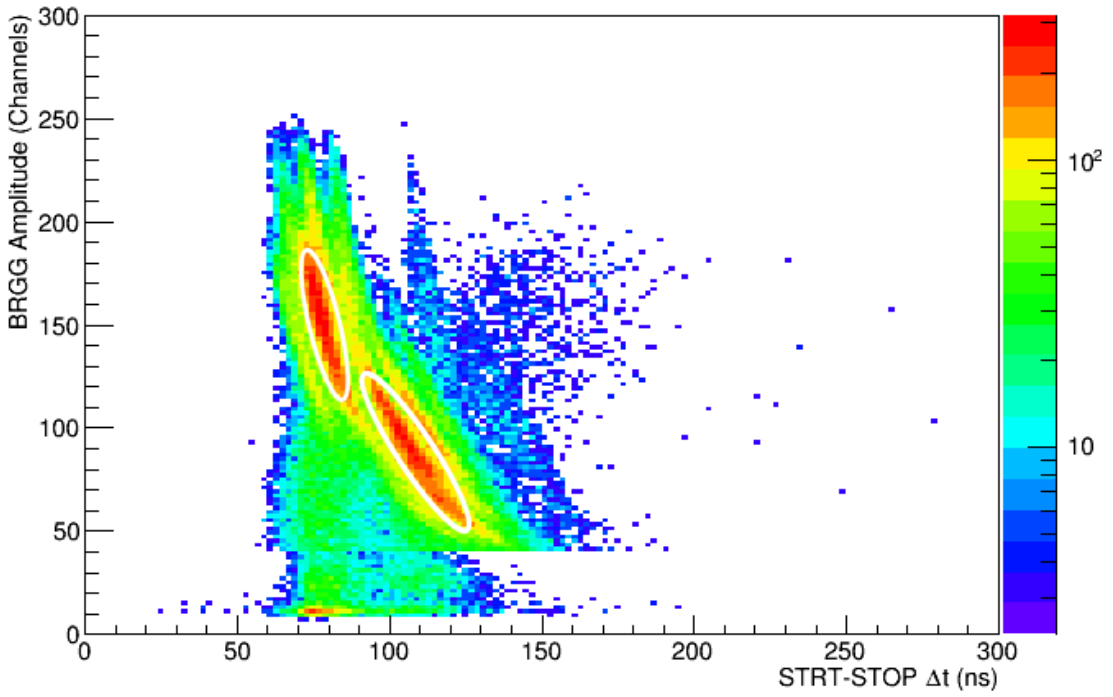

Figure 8.5: Distribution of the fission fragment energies and variation in inverse fragment velocities. Energies are measured by taking the amplitude of ion chamber signals and inverse velocities are determined using STRT-STOP timing results. Two main curves can be seen, along with "shadow" curves. These additional curves are due to the lack of gain matching between ion chamber anodes. Each ion chamber anode has a slightly different response to a fission fragment of the same energy, gain matching applies a correction to normalise these responses. As fission fragment information was not the primary focus of this analysis, this gain matching procedure was not carried out. The main curves are used as elliptical gates to determine fission events, the gates are shown as white ellipses in the figure.

Due to ongoing issues during the experiment regarding persistent signal noise and failure of detectors on the HIPS side, options 2 and 4 were both disregarded within this analysis as no meaningful data could be extracted from them. Only potential coincidences within the *Bragg* arm and the *FIFI Bragg* arm were considered for further analysis.

Once potential fission fragments have been located it is then a matter of identifying real fission fragments and false coincidences. Figure 8.5 shows the distribution of fission fragment time-of-flight data (which is an analogue for fragment velocity, calculated by measuring the difference in timestamps for the *Start* and *Stop* signals) along with the corresponding fragment signal amplitude in the *Bragg* ionisation chamber. The *FIFI Bragg*

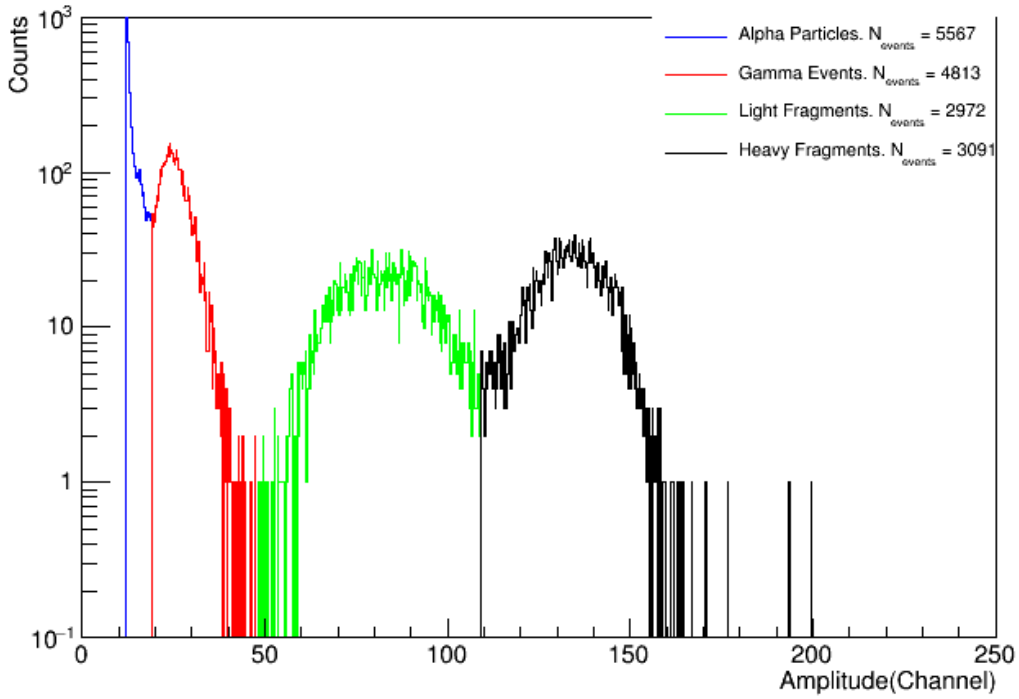

Figure 8.6: Amplitude distribution for *FIFI Bragg* signals, colour-coded by inducing particle. These results are taken from experimental phase one. The number of events listed in the upper-right corner are estimates, particularly for the heavy and light fragments as the amplitude distribution of each fragment overlaps one another. However the number of events for the heavy and light fragment are approximately equal and follow the distribution expected (as discussed in Chapter 2).

data have not been plotted in a similar fashion as there is no *Stop* detector equivalent within that arm so a reasonable time resolution is not achievable for the fission fragment time-of-flight; however the signal amplitude spread has been plotted in Figure 8.6. The distribution has been colour coded to represent different particles which have induced these signals. Any α particles entering the ionisation chamber will have low energy and only deposit small signals, the γ rays are due to the γ flash and when a time cut is applied which removes the γ flash these signals disappear. This leaves the light and heavy fragments which give a characteristic "double-hump" distribution.

The data for Figure 8.5 could be projected onto the amplitude axis in order to create a similar distribution for the main *Bragg* arm. However, the amplitude data for the *Bragg* detector are a combination of up to 15 different detector anodes, each of these anodes has

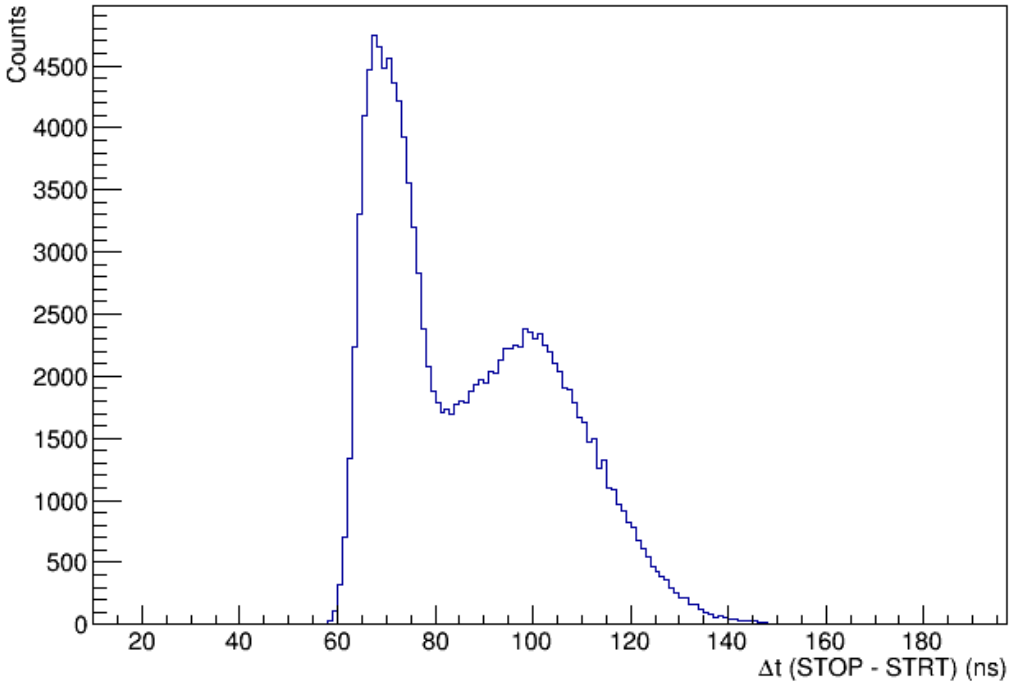

Figure 8.7: Time-of-flight distribution for *Bragg* arm events, measured by finding the difference between *Start* and *Stop* signals.

a characteristic impedance and each anode must be "gain-matched" in order to produce meaningful results. The investigation of the properties of the fission fragments is beyond the scope of this thesis (they are purely being used as markers for fission events), and was not performed. These data were projected onto the time-of-flight axis however, as this should produce a similar double-humped distribution and identify the true fission fragments from the false coincidences. This projection can be seen in Figure 8.7, the double hump is clear to see and aids in identification of true fission events.

Fission Event Timestamp Calculation

Once the real fission fragment events have been correctly identified from the false ones, they can be used in order to create a databank of time stamps relating to the actual time of fission itself. By taking the relative distance between the *Start* and *Stop* detectors compared to the distance between the ^{235}U target and the *Start* detector, combined with the time-of-flight data for the fission fragment in question, it is possible to retrace the flight

path of any fission fragment and determine at what time the fragment left the target. These timestamps were then collated and stored in a *"Fissions datafile"* in order to be used later in the analysis routines.

Plotting the distribution of these timestamps and comparing to an expected distribution will serve to verify that the timestamps recorded are indeed accurate. The expected distribution was calculated by multiplying the flux of the neutron beam by the fission cross section of ^{235}U, and factoring in the efficiencies of the various STEFF detectors. This comparison can be seen in Figure 8.8.

For the *FIFI Bragg* arm, due to the lack of a *Stop* detector, the timestamp for the *FIFI Start* signal was taken as an analogue for the fission time (this will be accurate to within the spread of fission times-of-flight). Due to this lack of resolution, however, a comparison was not drawn between measured and expected results.

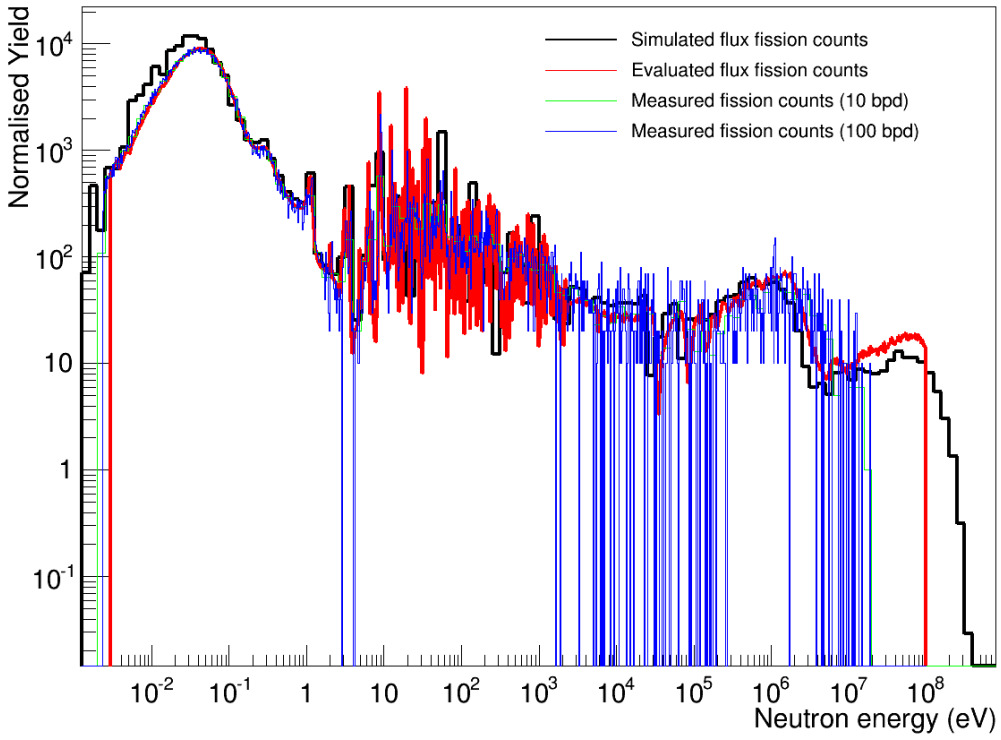

Figure 8.8: Comparison of the fission events distribution recorded by STEFF and the distribution expected from calculations, includes calculation results from both simulated neutron flux (prior to facility commencing operations) and evaluated neutron flux [84]. These two neutron flux datasets feature different binnings, which have been compared accordingly. Good agreement can be seen up to the keV region, after which statistical fluctuations begin to dominate.

Detector Timing Distributions

Using the fissions timestamps datafile it is possible to see how individual detector responses vary in their time distribution after the fission event. This is especially important for the NaI(Tl) as it will enable the determination of those NaI(Tl) signals which correspond to the prompt fission γ rays and those which are due to background or other effects. An important correction to this is due to the timing offset between different cards of the data acquisition system, for the details of this as it relates to the NaI(Tl) detector array see Section 6.3.

The distribution of time responses for NaI(Tl) detectors is shown in Figure 8.9. Here there is a clear peak corresponding to the γ rays produced from fission, and there is a roughly constant background throughout the distribution. Additionally there is a further feature in the distribution just after the prompt γ-ray peak; this small "hump" is thought to be due to prompt neutrons that have been created in the fission process and then captured within a NaI(Tl) detector - producing a signal. Further GEANT4 simulations may confirm this in the future.

Using this distribution, combined with the fissions datafile derived previously, it is possible to apply suitable time cuts (either side of the prompt peak) to the NaI(Tl) data in order to extract only that related to prompt fission spectra. These time cuts have been selected so as to sufficiently encompass the fission peak but reduce the amount of unwanted background that is selected. The width of this time selection was 30 nanoseconds, and signals detected within these 30 nanosecond windows after fission can be considered to have come from the same event (further details in the *"γ-ray Sum-Fold and Single γ Distributions"* section below). These time windows have been illustrated on Figure 8.9.

It is possible to perform the same operation for the *FIFI Bragg* fission events. However this is made more complicated by the lack of *Stop* detector, resulting in a less precise knowledge of the time of any fission event. For expediency, only the *Bragg* arm events have been considered further in this investigation. By developing a method to compensate for the aforementioned imprecision, future analysis may also consider *FIFI Bragg* fission

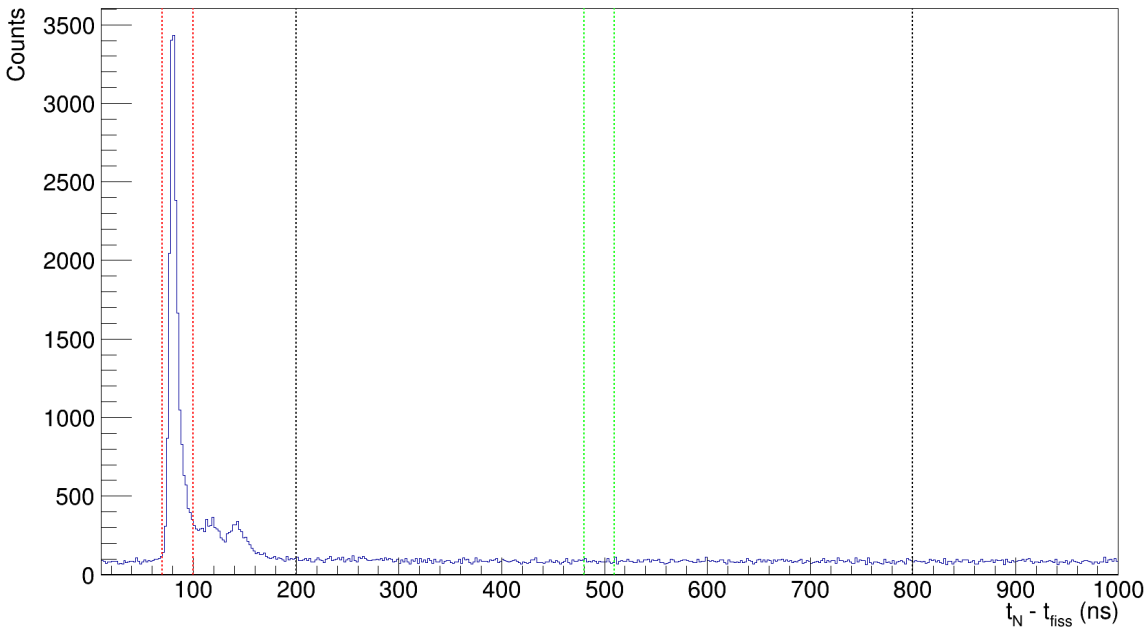

Figure 8.9: Distribution of NaI(Tl) array signals compared to the fission datafile timestamps. Dashed lines demonstrate where later time cuts are utilised. The red lines show the timing cuts used for γ rays assigned to prompt fission (for the single γ, the sum-energy and the fold distributions), the black lines show where the background single γ distribution time cuts are placed, and the green lines show where the background sum-energy and multiplicity distributions time cuts are placed.

events.

NaI Data Sorting

Now that the appropriate time cuts have been established they need to be applied to the NaI(Tl) data. However, due to the way the data acquisition collects data, the data trees containing the NaI(Tl) data are stored in such an order that would make applying these time cuts non-trivial. The trees are ordered hierarchically; first by proton bunch number, then by detector number (0-11 in the case of the NaI(Tl) array) and finally by time. When applying the time cuts derived previously the detector number is not relevant, so re-ordering the data in terms of bunch number followed by time (then finally by detector number, if there are any signals detected with the same timestamp), will make further analysis much smoother.

This step is carried out by a dedicated sorting code which imports the data trees and exports sorted textfiles for the NaI(Tl) array, doing so for each individual run.

Repetition and Summation

The routines above are repeated for all n_TOF runs requested by the code user, and then the data histograms are summed where appropriate (i.e. histograms are created to show fission fragment time-of-flight and energy data for the entire experimental campaign).

γ-ray Sum-Fold and Single γ Distributions

Now that the time cuts have been determined, the NaI(Tl) data sorted and these operations repeated for the whole dataset, it is time to actually extract the prompt fission γ-ray information.

Three measured distributions are required from the data in order to build up a picture of the true distribution. These measured distributions are:

- *Single γ-ray spectrum* – This is the distribution of individual γ-ray energies, with no

correlation between one another.

- *Fold distribution* – By applying the time window derived in the *"Detector Time Spreads"* section, signals detected within the same time window can be grouped together so as to be classed as a single "event". The fold distribution shows the distribution of the number of γ rays detected within each single event.

- *Sum-Energy γ-ray spectrum* – Similar to the fold distribution above, this is however the sum of those γ rays determined to have resulted from the same event.

The same routine is capable of deriving all three distributions simultaneously. This routine takes as its input the fissions datafile and corresponding NaI(Tl) sorted datafile. It then produces two datafile outputs – a single γ-ray spectrum datafile and a sum-fold datafile. The routine takes a fission event from the fissions datafile input, which has recorded several properties of the fission fragment – namely its time-of-flight between *Start* and *Stop* detectors and the amplitude of the signal in the *Bragg* detector (i.e. an analogue for fission fragment energy) – this information is then supplied directly to the output datafiles in order to enable cuts to be applied later if need be.

Once this fission event has been selected and written the routine then loops through the sorted NaI(Tl) datafile input, checking each entry to see if it meets the time criteria derived in the *"Detector Time Spreads"* section. If a data entry matches the requisite criteria then the NaI(Tl) signal information is passed to the single γ-ray spectrum datafile and simultaneously tallied separately. Once this time window closes the tallied information (i.e. number of signals and total energy of those signals) is passed to the sum-fold datafile.

The next fission event is then selected from the fissions datafile and this process is then repeated. This continues until the end of the fissions datafile and the result is two output datafiles. One datafile contains the distribution of measured folds (up to fold=10) and the other contains the sum-energy distribution.

Background Subtraction and Final Measured Data

As seen in Figure 8.9, there is an underlying background rate for the detection of γ rays within the NaI(Tl) array. In order to get an accurate picture of the prompt fission γ-ray distribution this background rate must be characterised and subtracted appropriately.

Fortunately the characterisation can be performed alongside the characterisation of the distributions mentioned in the previous section. A random spectrum is projected using a 200 - 800 ns window to produce a non-correlated γ-ray spectrum, normalised appropriately. A 30 ns window (480 - 510 ns) was used in order to produce sum-energy and fold spectra to compare with the previous measured data.

Once the background distributions have been suitably characterised, the background distribution needs to be subtracted from the measured total distribution in order to discern the "fission" distribution. This background subtraction is not as simple as taking the total and straight subtracting the background. A relative probabilistic background subtraction method must be used. This is due to the fact that, for example, a "fold = 2" event can actually be one of three situations, which would all result in a total fold of two:

- Two fission γ rays
- One fission γ ray and one background γ ray
- Two background γ rays

The same logic applies for any fold > 0 (a fold of zero can only be a combination of zero fission γ rays and zero background γ rays). This can be expressed generally by the equation

$$P_T(k) = \sum_{i,j}^{k} \delta_{kl} \cdot P_F(i) \cdot P_B(j); \tag{8.1}$$

where $P_T(k)$ represents the probability of an event measured to have a fold of k, $P_B(j)$ represents the probability that j of those are from background γ rays, $P_F(i)$ represents the

probability that i of them are prompt fission γ rays. The summation runs over i and j, each up to k, and the δ factor will remove any terms where $i+j \neq k$ (since $l = i+j$).

However, the terms $P_T(k \leq N)$ and $P_B(j \leq N)$ are the known terms and the values of $P_F(i \leq N)$ are the unknown values. This equation must be rearranged so as to calculate P_F. Rearranging Equation 8.1 gives the following result for fission fold probabilities,

$$P_F(k) = \frac{P_T(k)}{P_B(0)} - \frac{1}{P_B(0)} \cdot \sum_{j}^{k} \sum_{i}^{k-1} \delta_{kl} \cdot P_F(i) \cdot P_B(j), \tag{8.2}$$

where the terms of this equation are the same as that previous. This is an iterative calculation, as each $P_F(k)$ term depends upon the value of $P_F(k-1)$.

Due to the combinations of multiplications, divisions, subtractions etc. the uncertainty propagation for this relationship is complex. The propagation is discussed more fully in Appendix C but, in summary, the resulting equation is

$$\sigma_F(k)^2 = \frac{P_T(k)}{P_B(0)} \left[\frac{1}{N_T(k)} + \frac{1}{N_B(0)} + \frac{1}{N_B} + \frac{1}{N_T} \right] + \sum_{i}^{k} M_{i(k-i)} \left(\frac{1}{N_B(0)} + \frac{1}{N_F(i)} + \frac{1}{N_B(k-i)} + \frac{1}{N_F} + \frac{1}{N_B} + \frac{1}{N_B} \right), \tag{8.3}$$

where the coefficients given by M are

$$M_{ij} = \frac{P_F(i) \cdot P_B(j)}{P_B(0)}. \tag{8.4}$$

This formula can thus propagate the uncertainties of the measured total and background fold distributions (taken as $\sqrt{N}$) and give the total uncertainty on the fission fold value.

Thus the analysis has calculated the detected prompt γ-ray distribution, in terms of fold, single energies and sum energies. The sum energy and fold distributions can be

found on the left hand side of Figure 8.11.

8.2.2 Conversion to Emitted Spectra - Multiple Hit Subtraction and Deconvolution

The analysis thus far has determined the γ-ray distribution as it is detected by the NaI(Tl) array of STEFF. To account for factors inherent within the STEFF γ-ray detection setup (geometric efficiencies, multiple hit subtraction, scattering within the array, etc.) a routine to convert from detected to emitted data is required. The STEFF team at Manchester have a dedicated code to perform this conversion, *ansem.C*.

Multiple Hit Subtraction

It is possible that two distinct γ rays may enter the same detector within a small enough timeframe so as to make them indistinguishable from one another (this timeframe is typically of the same order as the rise time of the detector signal). If this occurs then the data output from the detector will be a single higher-energy γ ray, i.e. a summation of the two γ rays. These multiple hit events are therefore indistinguishable from a single high energy event and the contribution of this phenomenon must be considered.

In order to understand the effect of multiple hits, a GEANT4 [85] simulation of γ rays interacting with STEFF was created for the previous experimental run at the Institute Langue-Levin (ILL). The results of this simulation are used again here. A range of monoenergetic γ rays were simulated, with a probabilistic energy distribution based on previous experimental γ-ray spectra. From these simulated γ-ray inputs a range of response functions are produced, quantifying the level of energy deposited in each detector for each γ ray initiated. It is then possible to calculate the probability of a multiple-hit event occurring.

The methodology of this is discussed in [9]. The resulting probablility of an event being composed of multiple hits is dependent on the deposited energy of the event. This relationship for the STEFF spectrometer is shown in Figure 8.10 [9].

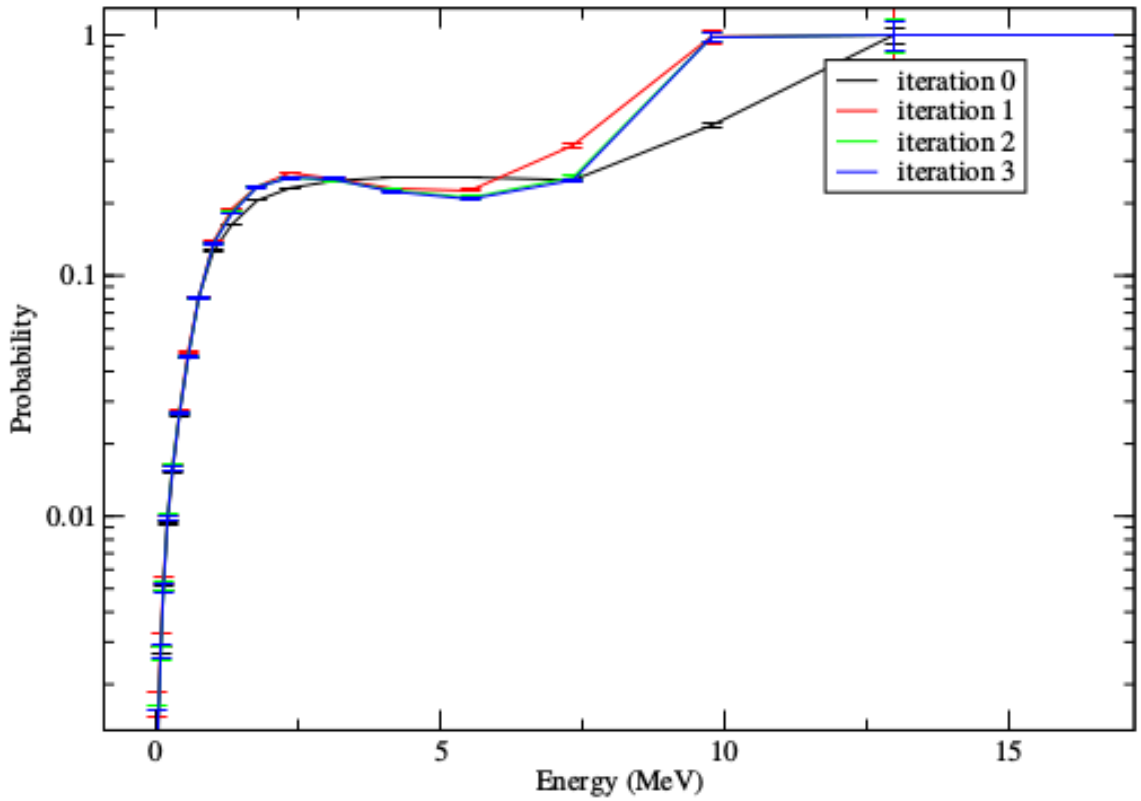

Figure 8.10: Fraction of events in STEFF γ-ray detector array which are composed of multiple hits, as discussed and calculated in [9].

Deconvolution

Deconvolution is required to correct the detected γ-ray energy distribution in order to account for any γ-ray energy loss prior to detection, for instance by Compton scattering in surrounding material. Once again Geant4 was used to simulate a range of γ-ray energies up to 20 MeV and generate response functions containing the proportion of energy deposited within each NaI(Tl) detector. By converting these response functions into a 2D matrix, γ-ray energy distribution against absolute total efficiency for the NaI(Tl) array as a function of energy, the detected energy spectrum can be expressed as the emitted spectrum multiplied by this 2D matrix. This matrix is then inverted utilising a Gauss-Jordan elimination [86]. This inverted matrix may then be used to deconvolve the detected single γ-ray data to determine the emitted single γ-ray spectrum. This process is described in more detail in [9].

Multiplicity and Sum-Energy Simulation

Monte Carlo simulations have been used to model the prompt γ-decay process of fission fragments to generate a total multiplicity (including both *statistical* and *yrast* γ rays). Based on the statistical probability distribution of yrast γ rays used by Huizenga and Vandenbosch [35] (described in Equation 2.5), a Monte Carlo simulation creates a fission event sampled from this distribution. The relationship between the spin quantum number and the yrast multiplicity is assumed to be linear, as it is these yrast γ rays which remove the majority of the spin of the fission fragment. For each fragment a number of statistical γ rays (N_{S1} and N_{S2}) are generated using independent geometrical probability distributions.

A second Monte Carlo simulation then determines the NaI(Tl) detectors responses to a given prompt fission multiplicity. This requires an understanding of the total overall efficiency of the detector array (measured to be $7.4\% \pm 0.2\%$), the peak-to-total ratios of the detectors and the scattering properties of the detectors [87]. The parameters underpinning this second Monte Carlo model (namely the value for the root-mean-square spin of a fission fragment, B in Equation 2.5, and the average number of statistical γ rays, $\bar{N}_S$) are

repeatedly adjusted until the result best matches the measured fold data. This adjustment is carried out using a simulated annealing algorithm to minimise the value of χ^2 for the fit. This process is described in detail in [88].

Utilising this method, the resulting value for prompt γ-ray multiplicity from the preliminary analysis of the Phase One data is $M_\gamma = 6.3 \pm 0.2$. To determine the sum-energy of the prompt fission γ rays the previously mentioned Geant4 generated library of response functions have been used. Optimising the parameters of a skewed Gaussian distribution (via the same simulated annealing method as previous) gives a sum-energy result of $E_{S,\gamma} = 9.0 \pm 0.1$ MeV. These results are inconsistent with those from previous experiments (see Table 1.1). Further analysis, along with consideration of the data achieved in phase two of the experiment may help to correct any systematic issues present, or provide confidence in these measured results.

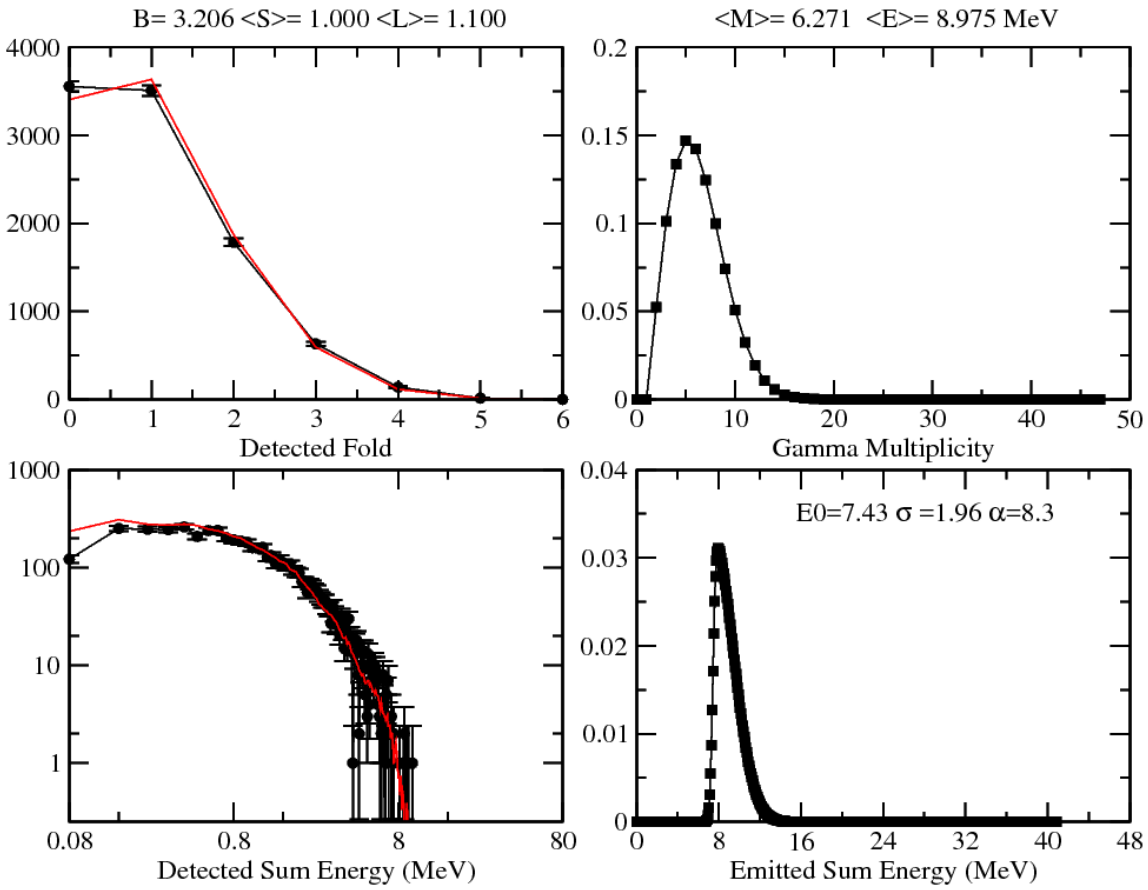

Figure 8.11: A comparison of the detected and emitted distributions for fold and sum energy for U-235 prompt fission γ-rays. The incoming neutron energy ranges from 0.025 eV to 1 eV. The y-axis of the left side graphs represents "Counts", the right side "Probability". The red lines on the left hand sub-figures represent the closest fitting results for fission γ ray multiplicities and energies from a range of Monte Carlo models of fission events.

Comparison with Previous Measurements

Table 8.2 summarises previous results and adds the result found within this thesis for comparison. It can be seen that this latest measurement is inconsistent with previous results, other than multiplicity results achieved by Verbinski and Pleasonton and the results for total γ-ray energy achieved by Wu and the previous STEFF measurement.

Table 8.2: Collection of results for measurements for average γ-ray multiplicity and energy, per fission of ^{235}U.

Cited Work	Average Multiplicity, $\bar{\nu}_\gamma$	Average γ-ray Energy, (ε_γ) (MeV)	Total Emitted Energy, $E_{\gamma,total}$ (MeV)	Neutron Energy Range
Verbinski (1973) [5]	6.70 ± 0.30	0.97 ± 0.05	6.51 ± 0.30	Thermal (0.025 eV)
Pleasonton (1972) [4]	6.51 ± 0.30	0.99 ± 0.07	6.43 ± 0.30	Thermal
Peelle (1971) [3]	7.45 ± 0.35	0.96	7.18 ± 0.26	Thermal
Obserstedt (2014) [13]	8.19 ± 0.11	0.85 ± 0.02	6.92 ± 0.09	Thermal
DANCE (2015) [14]	7.35 ± 0.35	N/A	8.35 ± 0.40	Thermal - 100 keV
ENDF/B-VII [12]	6.86	0.96	6.58	Thermal
STEFF (2015) [9]	7.74 ± 0.12	1.08 ± 0.03	8.40 ± 0.26	Thermal
STEFF (2017)	6.30 ± 0.20	1.42 ± 0.05	9.00 ± 0.10	Thermal - 1 eV

The first major difference between this new measurement and the majority of the previous measurements is that most previous measurements have considered only fission induced by thermal neutrons, whereas this measurement considers up to neutron energies exceeding 1 MeV (though the analysis in this thesis considers only up to 1 eV). An unavoidable by-product of producing neutrons up to such high energies is a huge amount of background radiation which is not present to the same degree within any of the previous measurements. Correcting for this background is paticularly challenging as the rate varies drastically with neutron time-of-flight (and therefore neutron energy). The work currently being performed to develop a bespoke processing and analysis code for STEFF experiments at n_TOF is expected to improve this background correction substantially and may bring results more in line with what has been seen previously.

There may also be a small contribution from the differences in targets between this experiment and those previous. Though most have used highly enriched metal targets (as has been used for Phase One of this experiment, and those results discussed here), Pleasonton has used an oxide target. This may have had an effect, though it is expected to be small. Once the data from Phase Two of this experiment are analysed it will be possible

to compare the effects of metallic and oxide targets to investigate if there is a systematic difference between the reasults for the two target types. Finally each measurement has applied a different lower threshold for γ-ray energy, ranging from 10 keV to 150 keV. The threshold for the results achieved by this measurement is 160 keV, this may account for a small discrepancy in measured fold distributions but it is not expected to have a large effect. This threshold should be able to be reduced by the bespoke processing and analysis code previously discussed.

As it has used the same experimental apparatus, it is sensible to draw a comparison with the previous STEFF result achieved by Murray [9]. The measurement results for total energy are consistent with one another, however the multiplicity values achieved are substantially different. The work performed by Murray only measured using a thermal neutron spectrum, the work discussed here is a continuation of that experiment to commissioning the STEFF detector at the n_TOF facility and begin measurements at higher neutron energies. Thus the key difference between the work discussed by Murray and the work discussed here is the neutron production method and subsequent background contribution, along with the effect on count rates to which STEFF detectors have been subjected to. The experiment described by Murray utilised thermal neutrons from a reactor source, with little γ-ray background contribution. Therefore the only background subtraction required is the removal of contribution from prompt neutrons, which was achieved through the use of the appropriate time gate (as has been done in this measurement, discussed earlier). Furthermore the count rate experienced in the NaI(Tl) scintillation array was vastly lower than has been seen in this latest measurement, for which the count rate varied dramatically across a single neutron pulse. As the current n_TOF processing routines only allow a single detector trace analysis for any single detector across an entire experimental run, there is the possibility of introducing a systematic issue whereby γ-ray signals are not being processed appropriately. This is a problem which will be resolved in the future once the bespoke n_TOF processing routine for STEFF has been fully implemented, as this allows a much greater flexibility in the detector trace analysis routines.

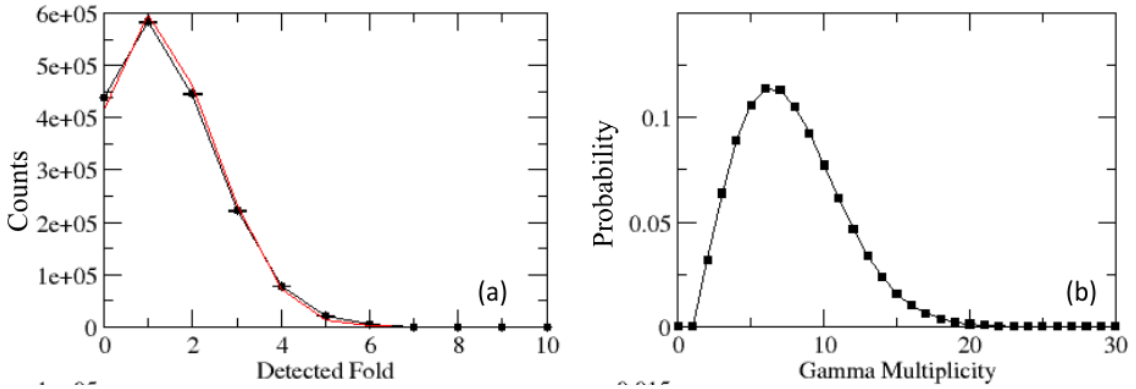

Figure 8.12: Fold distribution results from the previous STEFF experiment [9].

One apparent issue which suggests the potential of missing γ rays is a perceived over-abundance of "fold = 0" events in the detected data. When comparing the fold distribution measured for this experiment (top left graph of Figure 8.11) with that of the previous STEFF experiment (left graph of Figure 8.12) the ratios between "fold = 0" and "fold = 1" events does not align. In this experiment the ratio is approximately 1, whereas previous experimental results find a ratio of approximately 1.3 in favour of "fold = 1" events.

There are two potential reasons for this: 1) the processing routines are not recording some of the γ rays, as mentioned above or 2) the analysis routines are recording a number of extra fission events occuring. If a proportion of the γ rays are not recorded then fewer events will be recorded at a higher fold. The detected fold distribution will then shift towards a lower mean value and result in a ratio change similar to what has been seen. If this were occurring the effect would be much more dramatic at higher fold values. This is because measuring each γ ray in coincidence with a fission event is an independent (or near-independent) event, thus if there is a fixed probability of a γ ray going unrecorded this probability will compound itself when considering more γ rays. The small amount of data available suggests this may be the case, however, the small data set means this is not wholly reliable. Comparing the detected fold distributions suggests this may be the case, as the ratios between higher fold values does differ between experiments.

The other option is that extra fission events are being recorded, or non-fission events are being mistakenly categorised as fissions. Once again a review of the analysis routines

does not suggest that this is occurring. Strict cuts are placed on the fission identification portion of the analysis, preventing, for instance, alpha particles being assigned incorrectly as fissions.

A further consideration was that this issue may be dead time related. However as these data come from the thermal region of the neutron beam (< 1 eV) the count rate is not sufficiently high to cause such a dramatic effect (as shown in Figure 8.13). This is something which will require consideration as the higher neutron energy data are analysed.

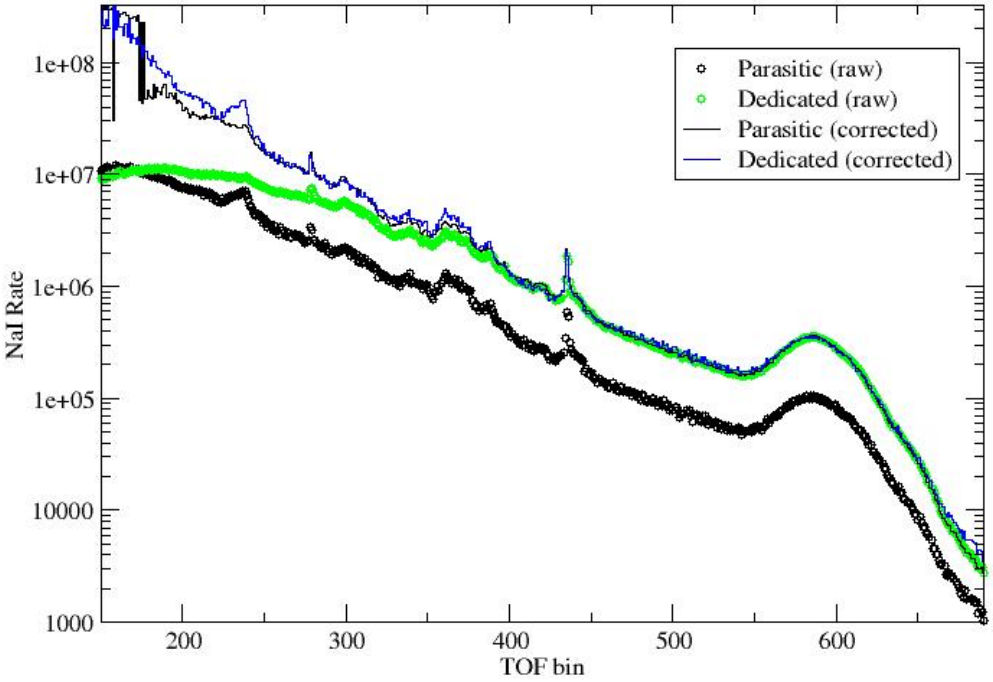

Figure 8.13: Results from an investigation into the effect of detector dead time in the NaI(Tl) detectors. It can be seen that dead time has no impact on the high time-of-flight (low neutron energy) region that has been analysed within this thesis. Image courtesy of A.G. Smith [89].

9

Conclusions and Future Work

This work describes the inaugural experiment of STEFF within a white neutron source facility, the Experimental Area 2 (EAR2) at n_TOF, CERN, measuring the ^{235}U(n,f) reaction. The analysis has focused on the γ-ray production aspect of the fission process and the detection of those γ rays within the STEFF spectrometer. The experiment itself was divided into two phases; the initial phase featuring a narrow aperture beam collimator installed in EAR2 and the second phase with a wide aperture collimator.

The background γ-ray rate within EAR2 is much higher than STEFF has previously been exposed to, and a simulation campaign was undertaken to investigate the feasibility of using shielding material to try and reduce the count rate experienced within the NaI(Tl) detector array, described in Chapter 5. The results of this investigation suggested that any feasible shielding setups did not make a significant enough difference to warrant the inclusion of shielding within the experiment.

As shielding was then not an option, the background count rate in EAR2 was anticipated to be high. Therefore detector development work was performed prior to the experiment in order to better optimise STEFF for this harsh environment. As discussed in Chapter 6, this consisted of reconfiguring the NaI(Tl) scintillation detectors in order for them to better cope with the higher count-rates expected. After these upgrades the NaI(Tl) detectors were demonstrated to count at a rate $> 3\ \mu s^{-1}$ (as exhibited in Figure 6.8), whereas previously the detectors were failing upon reaching any rate above $1\ \mu s^{-1}$. How-

ever at a count rate of 1.75 μs^{-1} the energy resolution of the NaI(Tl) scintillators failed. This means that sum-energy measurements would not be possible at such high count rates using these detectors, however multiplicity information may still be achieved.

The improved detectors were then used to perform a measurement of prompt fission γ rays from ^{235}U at n_TOF, CERN. After the development of many bespoke processing and analysis routines, discussed in Chapter 8, results for the sum-energy and the multiplicity of these prompt γ rays were achieved. Within the low count-rate environment (up to a maximum neutron energy of c. 1 eV), the preliminary analysis within this report suggest an average multiplicity and average sum-energy of $M_\gamma = 6.3 \pm 0.2$ and $E_{S,\gamma} = 9.0 \pm 0.1$, respectively.

There exists a discrepancy between the results achieved by the analysis within this document and previous results achieved. This has been discussed and comparisons drawn between previous measurements to attempt to understand the potential cause of this difference. Further understanding shall be gained once the current work ongoing within the STEFF team at Manchester is dedicated to the analysis of the remainder of the data garnered within this experiment is completed. This includes the development of a bespoke, CERN-integrated, set of processing routines which will focus on an event building approach. This is the current work of another PhD student and is expected to improve the Phase One results and commence analysis of Phase Two results in order to verify or improve the results found here.

9.1 Future of STEFF

STEFF has currently been dissassembled and returned to the University of Manchester for repairs and improvements to be carried out.

Ongoing improvements

Work is currently ongoing to improve the *Start* detector of STEFF, in order to prevent the ringing signals as seen in Figure 8.3. Figure 9.1 shows the current status of the *Start*

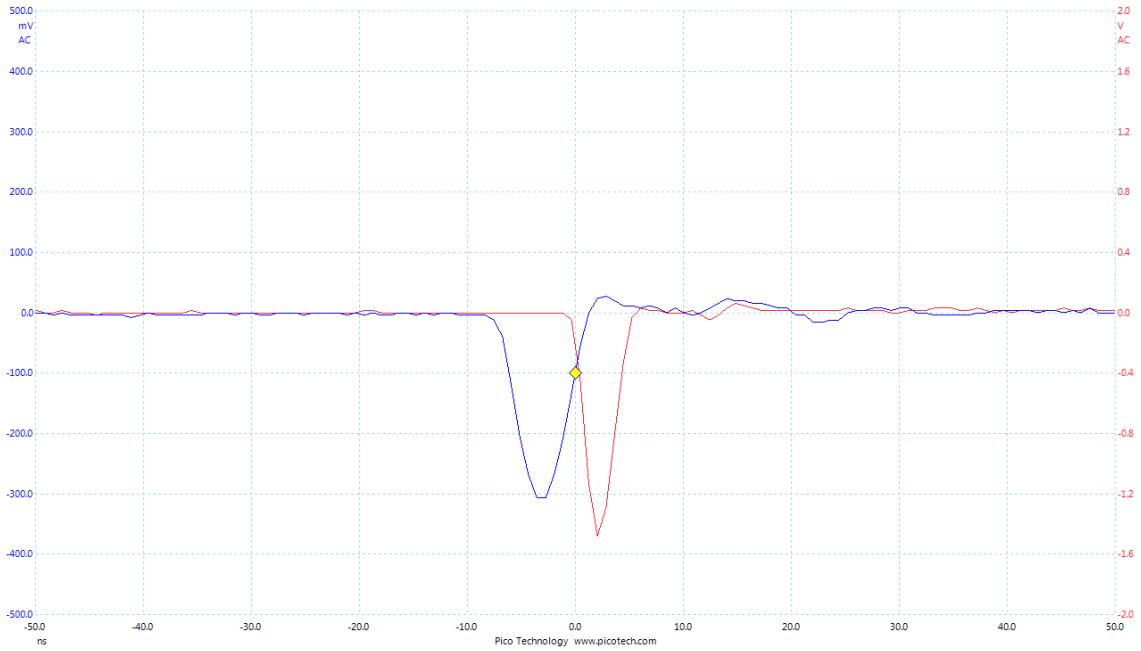

Figure 9.1: The latest tests of the improvements to the STEFF *Start* detector. The absence of large ringing signals (as shown in Figure 8.3) will improve the timing resolution of fission fragments in future measurements.

detector signal as improvements are underway.

Improvements to the analytical algorithms are also being carried out. As mentioned above a bespoke analysis package is being developed in order to achieve the best data possible from this experiment and all future CERN-based STEFF experiments. This package will be integrated into the currently existing CERN processing routines which convert the raw n_TOF data into a usable ROOT format. Instead of creating streams of data based on detectors, as is currently the case, the new routines will focus on building events which may consist of multiple signals in multiple detectors. Applying this at processing time rather than attempting to backfit data from the detector-stream format will improve the efficiency of analysis greatly.

Finally the STEFF team is currently investigating the possibility of acquiring several Lanthanum Bromide detectors from the Japanese Atomic Energy Agency (JAEA) to perform future experiments with. The collaboration of the JAEA will enable STEFF to utilise these $LaBr_3$ detectors to improve the response of STEFF to even higher count rate environments than those discussed in this investigation.

Future Work

STEFF is intended return to the n_TOF facility where a proposal will be submitted to measure the reaction ^{239}Pu(n,f), once again with a focus to investigating the prompt γ-ray emissions from the fission process. In addition to this further experiment there remains a wealth of data acquired within the experiments described here which will require rigorous analysis in order to refine the results.

STEFF has now been used within a thermal reactor system and also within a white neutron source facility, demonstrating the versatility of the STEFF spectrometer in measuring in a variety of environments. It is expected that STEFF will continue to be utilised in further experiments contributing towards nuclear data research.

References

[1] NEA High Priority Request List. *http://www.oecd-nea.org/dbdata/hprl/*. Retrieved 20.08.14.

[2] G. Rimpault, A. Courcelle & D. Blanchet. *Needs for accurate measurements of spectrum and multiplicity of prompt γ emitted in Fission*, 2006. HPRL, NEA.

[3] R.W. Peelle & F.C. Maienschein. Spectrum of Photons Emitted in Coincidence with Fission of ^{235}U by Thermal Neutrons. *Phys. Rev. C*, 3, Jan. 1971.

[4] F. Pleasonton et al. Prompt Gamma Rays Emitted in the Thermal-Neutron-Induced Fission of ^{235}U. *Phys. Rev. C*, 6, 1972.

[5] V.V. Verbinski et al. Prompt Gamma Rays from ^{235}U(n,f), ^{239}Pu(n,f) and Spontaneous Fission of ^{252}Cf. *Phys. Rev. C*, 7, Mar 1973.

[6] G. Rimpault et al. Needs of accurate prompt and delayed γ-spectrum and multiplicity for Nuclear Reactor Designs. *Physics Procedia*, 31:3 – 12, 2012.

[7] Generation IV International Forum. *Technology Roadmap Update for Generation IV Nuclear Energy Systems*. Technical report, January 2014.

[8] D. Iracane et al. Jules Horowitz Reactor: a high performance material testing reactor.

[9] E.S. Murray. *Measurement of the prompt gamma-ray energy distribution and multiplicity of ^{235}U following thermal fission using STEFF*. PhD thesis, University of Manchester, 2015.

[10] A.J. Pollitt. *Measurements of the total gamma-ray energy and multiplicity from the Fission of ^{252}Cf using STEFF*. PhD thesis, University of Manchester, 2013.

[11] J. Dare. *The Development of the Spectrometer for Exotic Fission Fragments*. PhD thesis, University of Manchester, 2009.

[12] M.B. Chadwick et al. ENDF/B-VII.1 Nuclear Data for Science and Technology: Cross Sections, Covariances, Fission Product Yields and Decay Data. *Nuclear Data Sheets*, 112(12):2887 – 2996, 2011.

[13] A. Oberstedt et al. Improved values for Characteristics of prompt-fission γ-ray spectra from the reaction ^{235}U(n,f). *Phys Rev C.*, 2013. 87(5):05 1602.

[14] C.Y. Wu et al. Total prompt γ-ray emission in fission of ^{235}U,^{239,241}Pu and ^{252}Cf. In *5th International Workshop on Compound-Nuclear Reaction and Related Topics*. Lawrence Livermore National Laboratory, 2015.

[15] Nobel Media AB. *Marie Curie - Other Resources*. http://www.nobelprize.org/nobel_prizes/physics/laureates/1903/marie-curie-or.html. Retrieved 11.07.2017.

[16] B.C. Reed. *The History and Science of the Manhattan Project*. Undergraduate Lecture Notes in Physics. 2014. ISBN 978-3-642-40296-8.

[17] World Nuclear Association. History of nuclear energy, *http://www.world-nuclear.org/information-library/current-and-future-generation/outline-history-of-nuclear-energy.aspx*. Retrieved 23.11.2016.

[18] K.S. Krane. *Introductory Nuclear Physics*. Wiley, 1987.

[19] Atomic Mass Data Center. Atomic Mass Adjustments, 2012. *http://amdc.in2p3.fr/masstables/Ame2012/mass.mas12*, Retrieved 19/11/2016.

[20] S.S.M. Wong. *Introductory Nuclear Physics*. A Wiley-Interscience publication. Wiley, 1998.

[21] J.W. Rohlf. *Modern Physics from* α *to* Z^0. John Wiley & Sons, Inc., 1994.

[22] D.J. Bennet and J.R. Thomson. *The Elements of Nuclear Power*. Longman Scientific & Technical, 1989.

[23] W.E. Burcham. *Nuclear Physics: An Introduction*. McGraw-Hill, 1963.

[24] W.M. Stacey. *Nuclear Reactor Physics*. Wiley-VCH, 2007. Second Edition.

[25] Frances Pleasonton. Prompt γ-rays emitted in the thermal-neutron induced fission of ^{233}U and ^{239}Pu. *Nuclear Physics A*, 213(2):413 – 425, 1973.

[26] M.E. Gooden et al. Energy Dependence of Fission Product Yields from ^{235}U, ^{238}U and ^{239}Pu for Indicent Neutron Energies Between 0.5 and 14.8 MeV. *Nuclear Data Sheets*, 131:319–356, 2016.

[27] J.S. Lilley. *Nuclear Physics: Principles and Applications*. Manchester Physics Series. J. Wiley, 2001.

[28] U.S. Department of Energy. *DOE Fundamentals Handbook: Nuclear Physics and Reactor Theory*, volume 1. US DOE, 1993. DOE-HDBK-1019/1-93.

[29] I. Ahmad and W.R. Phillips. Gamma rays from fission fragments. *Rep. Prog. Phys.*, 58:1415, 1995.

[30] D.G. Madland. Total prompt energy release in the neutron-induced fission of ^{235}U, ^{238}U, and ^{239}Pu. *Nuclear Physics A*, 2006.

[31] N. Kornilov, F.J. Hambsch, I. Fabry, S. Oberstedt, et al. The ^{235}U (n,f) Prompt Fission Neutron Spectrum at 100 K Input Neutron Energy. *Nuclear Science and Engineering*, 2010.

[32] Thierry Ethvignot, Matt Devlin, Thierry Granier, Robert C Haight, Ronald O Nelson, John M O Donnell, and Dimitri Rochman. Measurement of the Average Multiplicity of Prompt-Fission Neutrons from ^{238}U(n,f) and ^{235}U(n,f) from 0.7 to 200

MeV. In *AIP Conference Proceedings*, volume 769, page 656. IOP INSTITUTE OF PHYSICS PUBLISHING LTD, 2005.

[33] M Aziz, MO Shaker, A Aboanber, E Massoud, and M Slama. Improved formula for prompt fission neutron spectrum. *Journal of Nuclear and Radiation Physics*, 6 (1&2):31–41.

[34] D. Frenne. *The Nuclear Fission Process*. CRC Press, 1991.

[35] J. R. Huizenga and R. Vandenbosch. Interpretation of isomeric cross-section ratios for (n,γ) and (γ,n) reactions. *Phys. Rev.*, 1960.

[36] K. Skarsvåg. Angular Correlation of Fission Fragments and Prompt γ-rays from Slow Neutron Fission of ^{235}U. *Nuclear Physics A*, 96.

[37] C. Weiss. Present and Future of Fission at n_TOF. In *Nuclear Fission and Structure of Exotic Nuclei*. 16th ASRC International Workshop.

[38] C. Rubbia et al. *A high resolution spallation driven facility at the CERN-PS to measure neutron cross sections in the interval from 1 eV to 250. MeV*. Technical report.

[39] E. Chiaveri. The CERN n_TOF Facility: Neutron Beams Performances for Cross Section Measurements. *Nuclear Data Sheets*, 119:1–4, 2014.

[40] M. Calviani et al. The n_TOF Facility at CERN: Present Status and Future Upgrades. In *ICANS XIX - 19th meeting on Collaboration of Advanced Neutron Sources*, 2010.

[41] E. Chiaveri et al. Past, Present and Future of the n_TOF Facility at CERN. *Journal of the Korean Physical Society*, 59(2):1620 – 1623, 2011.

[42] C. Guerrero et al. Performance of the neutron time-of-flight facility n_TOF at CERN. *Eur. Phys. J A*, 49:27, 2013.

[43] CERN Research Board. *http://committees.web.cern.ch/committees/rb/*. Retrieved 14.08.14.

[44] E. Chiaveri et al. (the n_TOF Collaboration). Proposal for the n_TOF Experimental Area 2 (EAR-2). *Proposal to the ISOLDE committee*, 2012.

[45] C. Carrapiço et al. (the n_TOF Collaboration). Design study for a new spallation target of the n_TOF facility at CERN. In *International Conference on Nuclear Data for Science and Technology*, 2007.

[46] F. Gunsing. n_TOF one year after - First Results, 2015. Retrieved from *https://ep-news.web.cern.ch/content/ntof-one-year-after-first-results* on 17.04.2017.

[47] I. Bergstrom. Minimizing the background radiation in the new neutron time-of-flight facility at CERN. Master's thesis, Luleå University of Technology, 2013.

[48] C. Weiß et al. The New Vertical Neutron Beam Line at the CERN n_TOF Facility Design and Outlook on the Performance. *Nucl. Instrum. Meth. A*, 799:90 – 98, 2015.

[49] V. Vlachoudis. FLAIR: FLUKA Advanced Interface. *http://www.fluka.org/flair/index.html*.

[50] E. Chiaveri. n_TOF Experimental Area 2 (EAR2) Preliminary Feasibility Study. INTC July 2011 Meeting, 2011.

[51] A.D. Carlson et al. International Evaluation of Neutron Cross Section Standards. *Nuclear Data Sheets*, 2009.

[52] T. Wright. *High Accuracy Measurement of the ^{238}U(n,γ) Cross Section at the CERN n_TOF Facility*. PhD thesis, University of Manchester, 2014.

[53] A. Musumarra et al. (the n_TOF Collaboration. Silicon detectors for the neutron flux and beam profile measurements of the n_TOF facility at CERN. *Review of Scientific Instruments*, 86(7), 2015.

[54] F. Belloni et al. (the n_TOF Collaboration. Neutron beam imaging with an XY-micromegas detector at n_TOF, CERN. *Phys. Scr.*, 2012:014004, 2012.

[55] S. Barros et al. Optimization of n_TOF-EAR2 using FLUKA. *Journal of Instrumentation*, 10(09):P09003, 2015. URL http://stacks.iop.org/1748-0221/10/i=09/a=P09003.

[56] L. Cosentino, A. Musumarra, M. Barbagallo, N. Colonna, L. Damone, A. Pappalardo, M. Piscopo, and P. Finocchiaro. Silicon detectors for monitoring neutron beams in n-tof beamlines. *Review of Scientific Instruments*, 86(7):073509, 2015.

[57] C. Borcea et al. Results from the Commissioning of the n_TOF Spallation Neutron Source at CERN. *Nucl. Instr. and Meth. A*, 513:524–537, 2003.

[58] F. Gunsing et al. Nuclear data activities at the n_TOF facility at CERN. *Eur. Phys. J. Plus*, 131:371, 2016.

[59] S. Lo Meo et al. GEANT4 simulations of the n_TOF spallation source and their benchmarking. *Eur. Phys. J. A*, 51(12):160, 2015.

[60] P. Boisseau. *Study of the γ-flash effect on the Spectrometer for Exotic Fission Fragments (STEFF) located at CERN*. Technical report, University of Manchester, 2016.

[61] U. Abbondanno et al. (The n_TOF Collaboration). The Data Acquisition System of the Neutron Time-of-Flight Facility n_TOF at CERN. *Nucl. Instr. Meth. A*, 538:692 – 702, 2005.

[62] CERN Advanced STORage manager. castor.web.cern.ch.

[63] R. Brun and F. Rademakers. ROOT: An object oriented data analysis framework. *Nucl. Instrum. Meth. A*, 389:81–86, 1997.

[64] P. Zugec et al. (The n_TOF Collaboration. Pulse processing routines for neutron time-of-flight data. *Nucl. Instr. Meth. A*, 812:134 – 144, 2016.

[65] S. Warren. *Development of the STEFF detector for the neutron Time Of Flight facility (n_TOF), CERN*. PhD thesis, University of Manchester, 2016.

[66] Hamamatsu Photonics K.K. Mcp (microchannel plate) and mcp assembly, 2016. *https://www.hamamatsu.com/resources/pdf/etd/MCP_TMCP0002E.pdf*, Retrieved 28/09/2016.

[67] J.P. Coffin & P. Engelstein. *Treatise on Heavy Ion Science*, volume 7: Instrumentation and Techniques. Springer Science and Business Media, New York, 1985. Section 3.2.

[68] F. Sauli. *Principles of Operation of Multiwire Proportional and Drift Chambers*. CERN, 1977. Lectures given in the Academic Training Programme of CERN, 1975-1976.

[69] D. Hodge. *Construction and Testing of a Large Acceptance Angle, Double Sided Bragg Ionisation Chamber for Fission Fragment Spectroscopy*. Master's thesis, University of Manchester, 2012.

[70] W.E. Burcham. *Elements of Nuclear Physics*. A Pearson education print on demand edition. Longman, 1979. ISBN 9780582460270. URL https://books.google.co.uk/books?id=t8-6AAAAIAAJ.

[71] R.M. Singru. *Introduction to Experimental Nuclear Physics*. Wiley, 1975.

[72] G.F. Knoll. *Radiation Detection and Measurement*. John Wiley & Sons, Inc. 3rd Edition.

[73] A. Oed et al. High resolution axial ionization chamber for fission products. *Nucl. Inst. and Meth.*, 205(3), 1983.

[74] Central Limit Theorem. http://mathworld.wolfram.com/CentralLimitTheorem.html. Retrieved 17.04.2017.

[75] D.P. Landau and K. Binder. *A Guide to Monte-Carlo Simulations in Statistical Physics*. Cambridge University Press, 2009. Third Edition.

[76] A. Ferrari et al. FLUKA: a multi-particle transport code. 2005. CERN-2005-10.

[77] The Joint Evaluated Fission and Fusion File (JEFF-3.2). www.nea.fr/html/dbdata/JEFF. Retrieved 18.09.2017.

[78] N. Soppera, M. Bossant, and E. Dupont. JANIS 4: An Improved Version of the NEA Java-based Nuclear Data Information System. *Nuclear Data Sheets*, 120:294 – 296, 2014.

[79] P. Schotanus. Private communications, 2015.

[80] Gafchromic Films. http://www.gafchromic.com/gafchromic-film/index.asp. Retrieved 11.07.2017.

[81] L. Snyder et al. Measuring the SF Branching Ratio of ^{252}Cf with the NIFFTE TPC. *Nuclear Data Sheets*, 119:386 – 388, 2014.

[82] B. Lher et al. High count rate γ-ray spectroscopy with $LaBr_3$:Ce scintillation detectors. *Nucl. Instr. Meth. A*, 686, 2012.

[83] L. Tassan-Got. Private communications, 2015.

[84] M. Sabaté-Gilarte. *The n TOF-EAR2 facility at CERN: neutron flux determination and $^{33}S(n,\alpha)^{30}Si$ cross section measurement; implications in BNCT*. PhD thesis, Universidad de Sevilla, 2017.

[85] S. Agostinelli et al. Geant4—a simulation toolkit. *Nucl. Inst. and Meth. A*, 506(3): 250 – 303, 2003.

[86] E. Süli et al. *An Introduction to Numerical Analysis*. Cambridge University Press, 2003.

[87] A.J. Pollitt et al. Gamma-ray multiplicity measurements using STEFF. *Journal of Physics: Conference Series*, 2012.

[88] E. Murray et al. Measurements of gamma energy distributions and multiplicities using STEFF. *Nuclear Data Sheets*, 119:217–220, 2014.

[89] A.G. Smith. Private communications, 2017.

Appendices

A

Appendix A - FLUKA Input File Description

The input file for FLUKA is a plain text file, containing sufficient information to describe the simulation, as an input file and produces binary output files which require special subroutines (offered within the FLUKA package) to process the data. The FLUKA input file contains:

1. Geometry description
2. Materials definitions and assigments
3. Beam properties
4. Physics options
5. Scoring/estimators
6. Biasing settings
7. Initialisation and START card

Geometry

The combinatorial geometry package allows FLUKA to simulate extremely detailed and complex geometries by using a system of bodies and regions. Bodies are generally convex solid bodies, but recently have been updated to include infinite cylinders and infinite planes (half-spaces). Regions are then combinations of these bodies produced by

boolean operations (Union, Subtraction and Intersection). Each region must be of homogeneous material composition and every point in space must belong to a single region. Additionally, the geometry must be surrounded entirely by a "black hole" region, which absorbs any particle entering the region and removes it from the simulation.

A comprehensively detailed geometry of the entire n_TOF facility has been developed since the start of the n_TOF experiments in 2001 and is maintained by V. Vlachoudis [1]. This report focuses on the new experimental area (EAR2), the geometry of which can be seen in Figure 5.1.

Materials

FLUKA contains a number of pre-defined materials and allows the user to easily define any materials they require which are not present already by assigning properties such as density and atomic composition in order to create a wholly accurate simulation. The FLUKA database contains each of the 'straight' elements of the periodic table which may be used to build materials and compounds. Each region must be assigned a material.

Beam Properties

In a typical FLUKA simulation a beam is defined by properties such the beam energy, the beam energy width, its spatial profile and the beam position/direction. However when dealing with complicated beams, such as the neutron beam at n_TOF, where the beam is not a single particle, doesn't have a simple energy distribution or has a complicated direction distribution, the user must use augment FLUKA with a user-written subroutine. A subroutine, written in FORTRAN, alters the way FLUKA deals with the input file, or affects the way the simulation runs. The most common subroutine (and the one used to define complex beams) is the "source" subroutine. The source routine may either replace or augment the beam card within the input file and may generate particles according to a

[1] V. Vlachoudis homepage: `bnv.home.cern.ch/bnv/`

user-given code or it may get particle data from another file (e.g. a collision file resulting from an earlier simulation).

Physics Options

The physics options section of an input file deals with how particles are transported and which interactions should be included within the simulation. For example, the EMF option may select whether or not to transport electrons, positrons and photons and at which energy threshold to remove these particles from the simulation (this can drastically reduce the simulation time necessary if these particles are of no interest). These options are mainly concerned with the production and transport thresholds for various types of particles.

Scoring

Scoring is how the user informs FLUKA of the desired output. The input file contains one or more scoring cards and these define the quantity the user is interested in measuring. FLUKA offers a wide range of quantities which may be scored in a simulation, e.g. energy deposition within a region, particle fluence across a boundary and the dose in a volume are among the most common. FLUKA may output these results in a formatted (ASCII) or non-formatted (binary) file with a given unit number. All binary output files can be post-processed, merged and graphically visualised in FLAIR [49].

Biasing

In order to improve convergence and/or run-time, a Monte Carlo simulation can be biased. In FLUKA there are two main forms of biasing, Particle Splitting (reduce variance, increase run-time) and Russian Roulette (decrease run-time, increase variance), these apply on particles crossing a boundary and can be used to encourage the simulation to focus on particles travelling in a desired direction.

Initialisation and Starting/Stopping

As Monte Carlo is a process based on random numbers it can be difficult to replicate results if one needs to. To get around this one can assign a starting "seed" number for a simulation, and then identical simulations with an identical starting seed number should output identical results. The simulation can then be started with a requested number of particle histories and will end when the stop command has been reached.

B

Appendix B - NaI(Tl) Calibration Graphs

These graphs show the results of NaI(Tl) calibration discussed in Section 6.3.

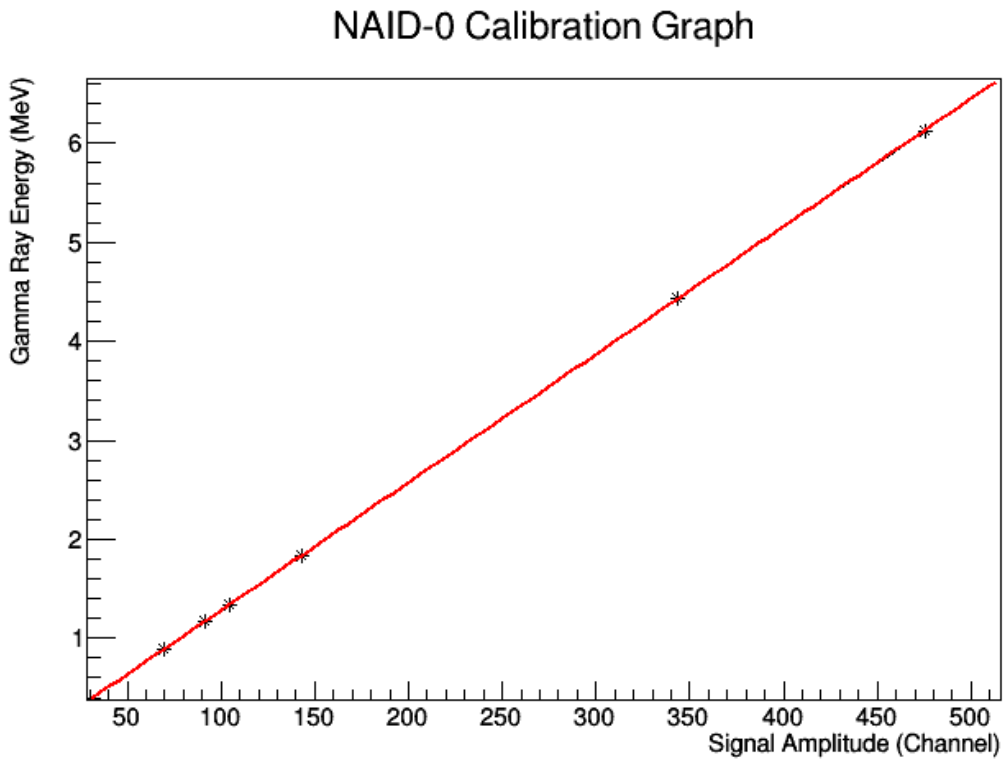

Figure B.1: Calibration data for NaI(Tl) detector #0, including results from ^{88}Y, ^{60}Co, ^{137}Cs, ^{241}Am-^{9}Be, and ^{244}Cm-^{13}C sources.

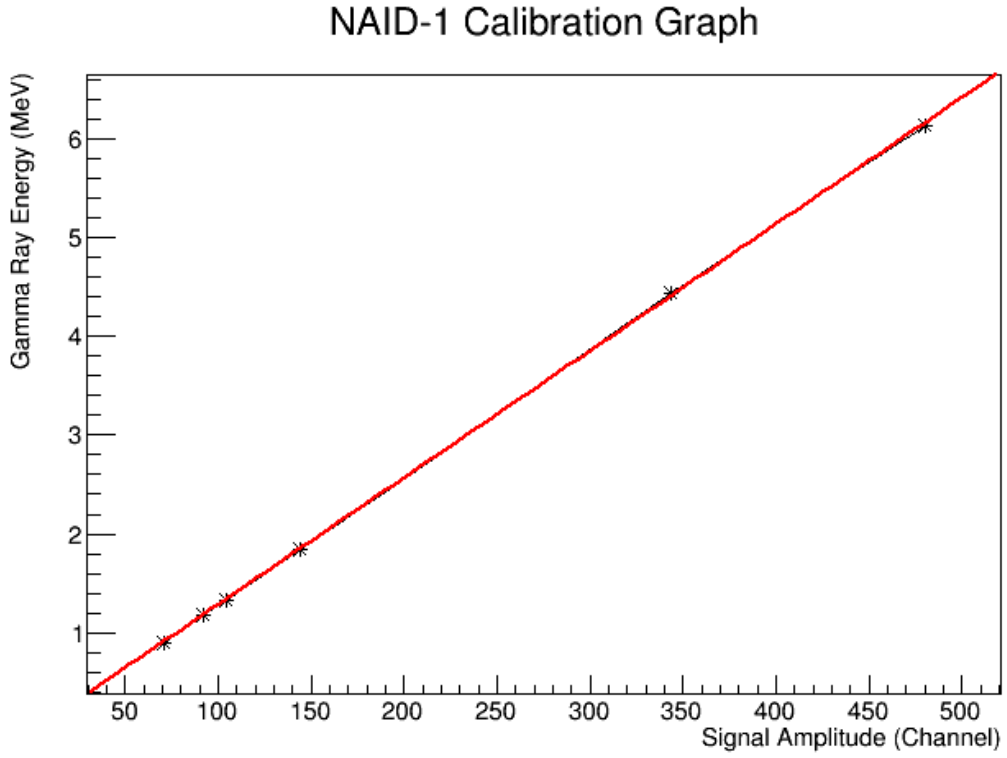

Figure B.2: Calibration data for NaI(Tl) detector #1, including results from ^{88}Y, ^{60}Co, ^{137}Cs, ^{241}Am-^{9}Be, and ^{244}Cm-^{13}C sources.

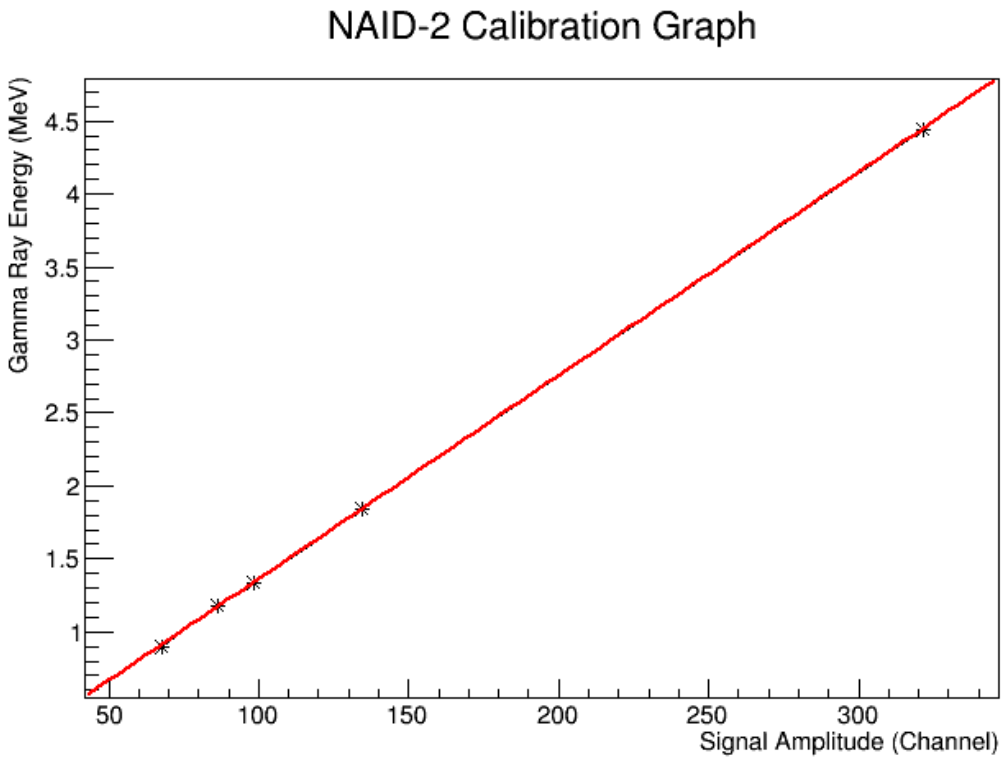

Figure B.3: Calibration data for NaI(Tl) detector #2, including results from ^{88}Y, ^{60}Co, ^{137}Cs and ^{241}Am-^{9}Be sources.

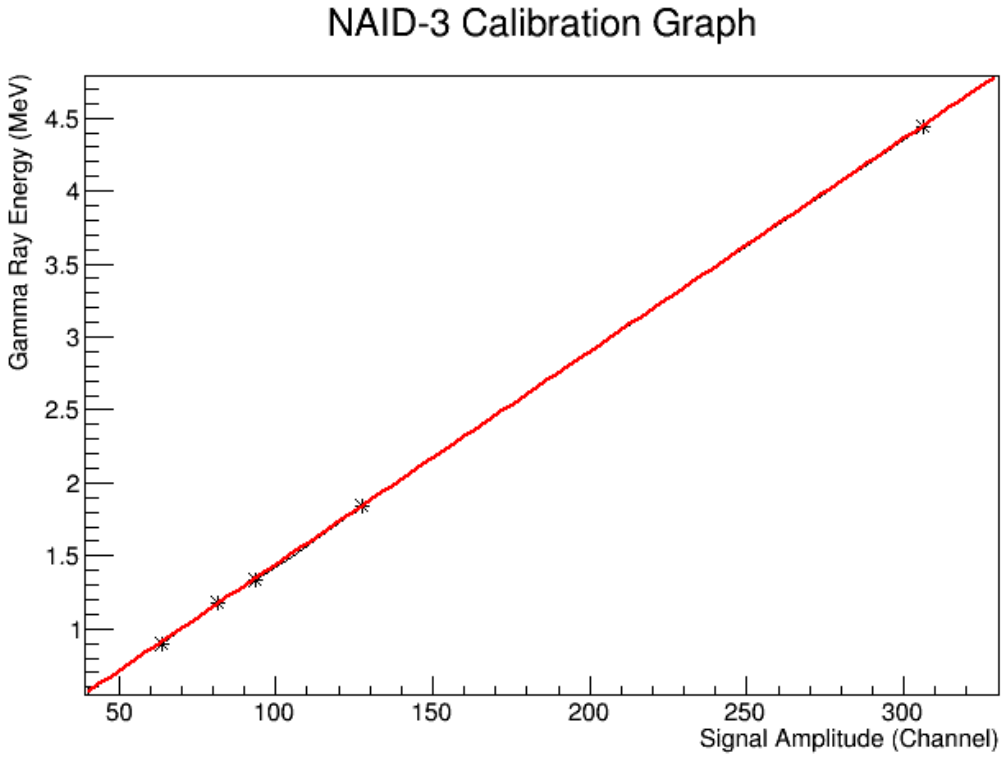

Figure B.4: Calibration data for NaI(Tl) detector #3, including results from ^{88}Y, ^{60}Co, ^{137}Cs and ^{241}Am-^{9}Be sources.

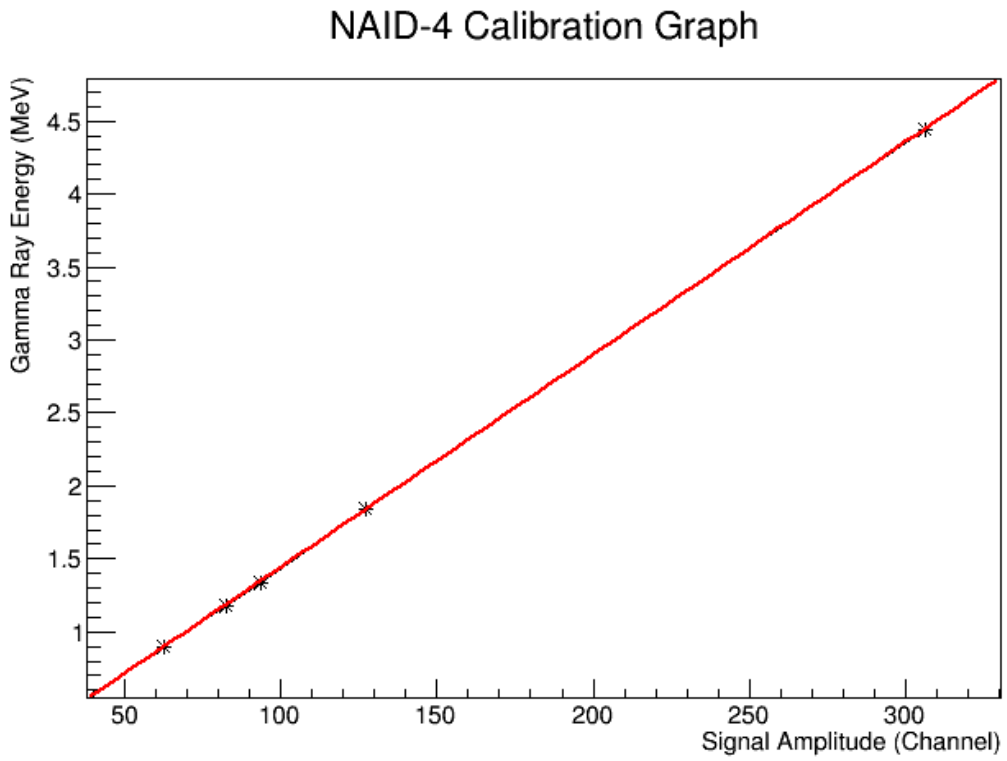

Figure B.5: Calibration data for NaI(Tl) detector #4, including results from ^{88}Y, ^{60}Co, ^{137}Cs and ^{241}Am-^{9}Be sources.

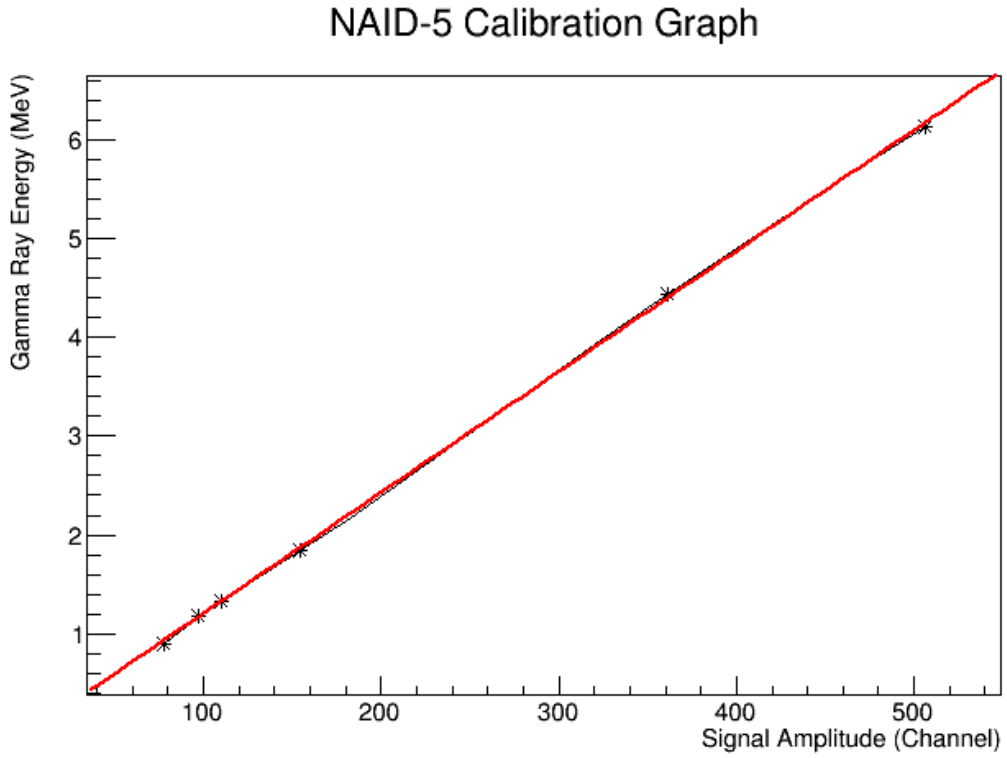

Figure B.6: Calibration data for NaI(Tl) detector #5, including results from ^{88}Y, ^{60}Co, ^{137}Cs, ^{241}Am-^{9}Be, and ^{244}Cm-^{13}C sources.

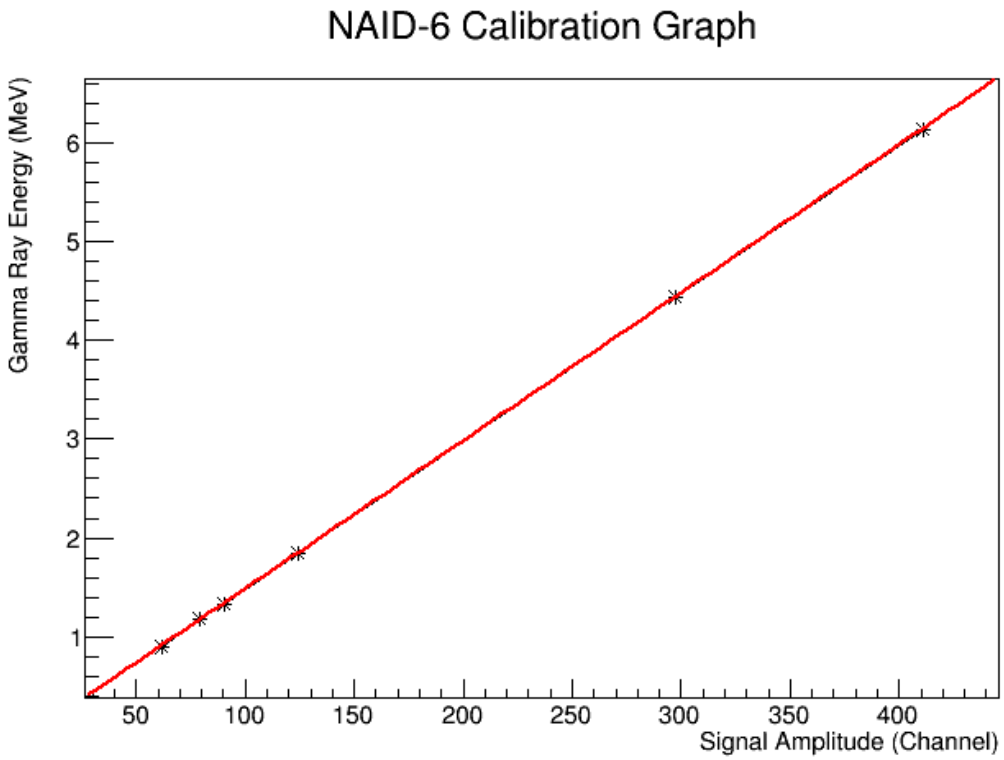

Figure B.7: Calibration data for NaI(Tl) detector #6, including results from ^{88}Y, ^{60}Co, ^{137}Cs, ^{241}Am-^{9}Be, and ^{244}Cm-^{13}C sources.

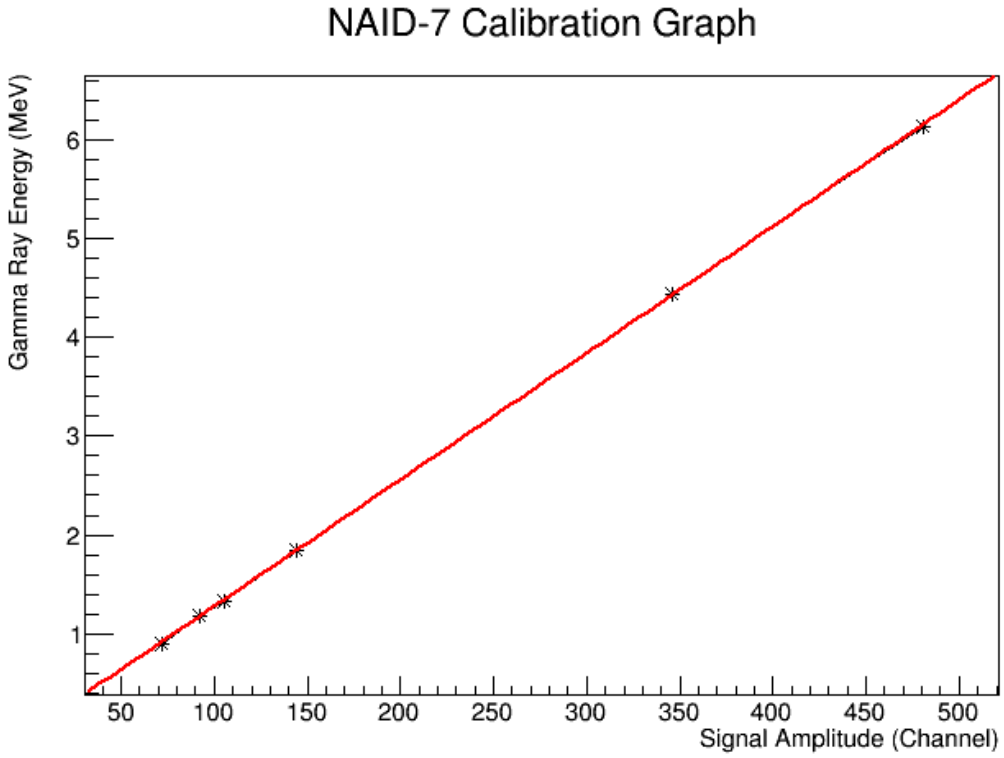

Figure B.8: Calibration data for NaI(Tl) detector #7, including results from ^{88}Y, ^{60}Co, ^{137}Cs, ^{241}Am-^{9}Be, and ^{244}Cm-^{13}C sources.

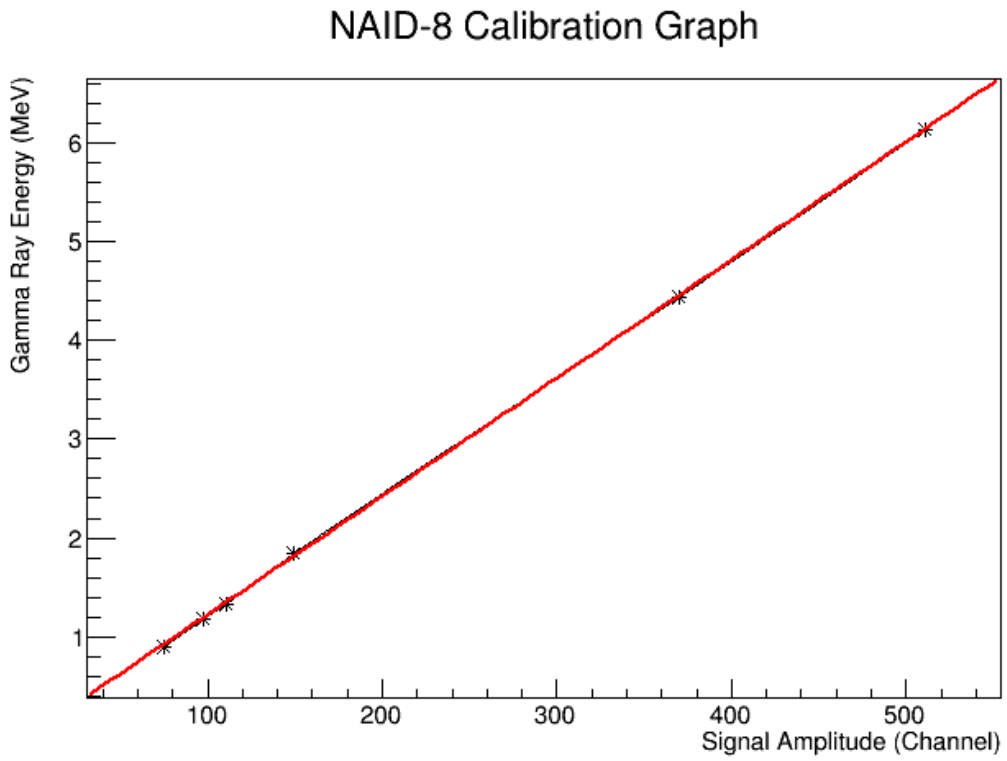

Figure B.9: Calibration data for NaI(Tl) detector #8, including results from ^{88}Y, ^{60}Co, ^{137}Cs, ^{241}Am-^{9}Be, and ^{244}Cm-^{13}C sources.

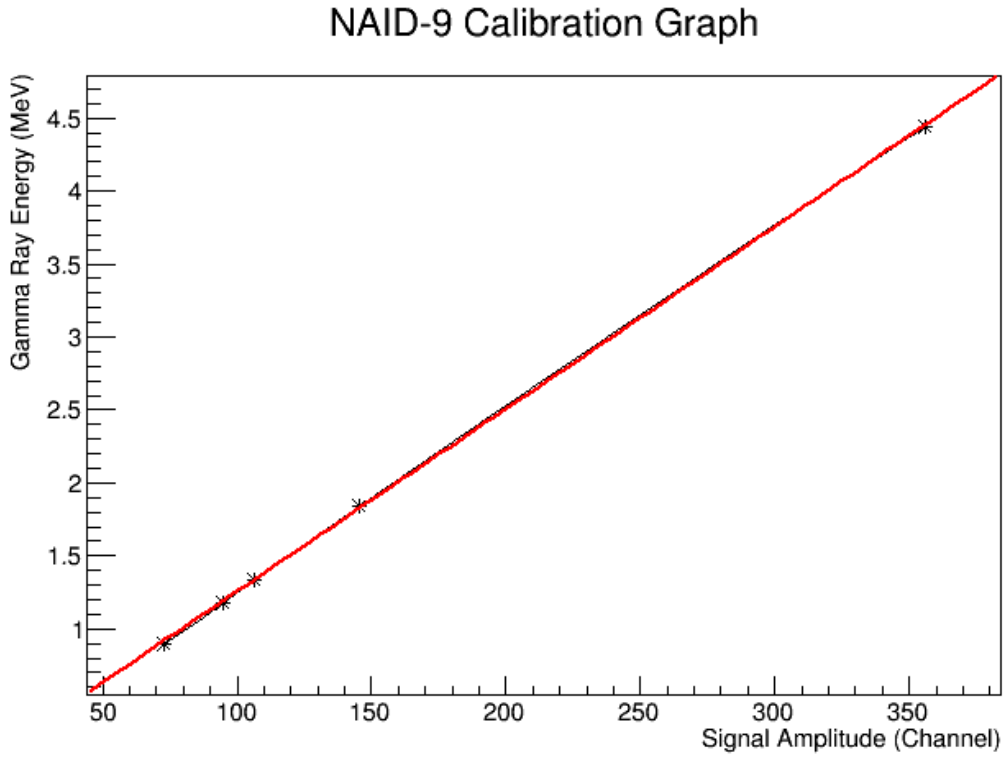

Figure B.10: Calibration data for NaI(Tl) detector #9, including results from ^{88}Y, ^{60}Co, ^{137}Cs and ^{241}Am-^{9}Be sources.

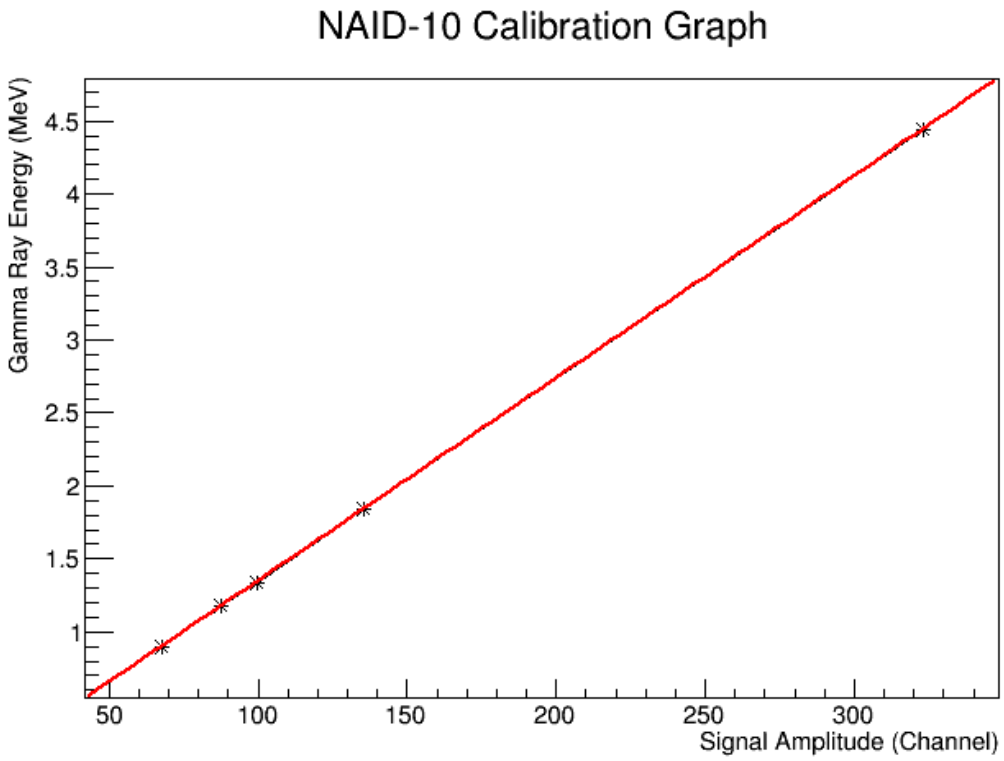

Figure B.11: Calibration data for NaI(Tl) detector #10, including results from ^{88}Y, ^{60}Co, ^{137}Cs and ^{241}Am-^{9}Be sources.

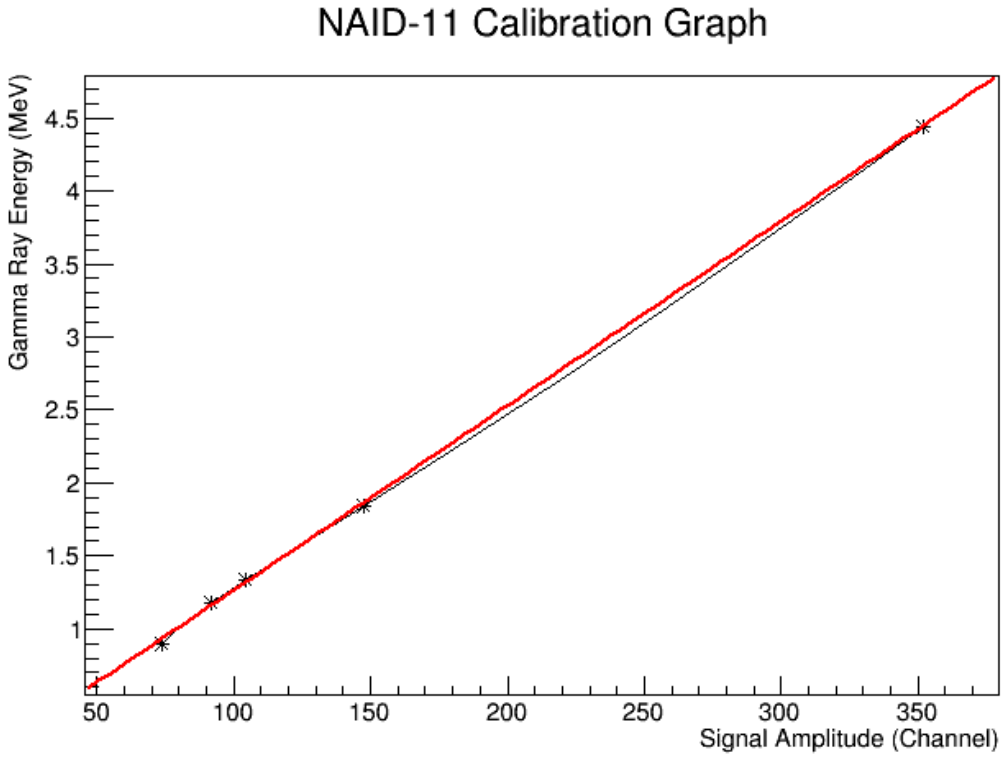

Figure B.12: Calibration data for NaI(Tl) detector #11, including results from ^{88}Y, ^{60}Co, ^{137}Cs and ^{241}Am-^{9}Be sources.

C

Appendix C - Fold Probability Uncertainty Propagation

The method for retrieving the fission γ-ray fold distribution from experimental and background results is discussed in Section 8.2.1. Equation 8.2 is derived which is used to calculate the probability of detecting k γ-rays following a fission event. Equation 8.3 is given also which calculates the uncertainty on this probability. The derivation of this is non-trivial and therefore is given here instead of the main text.

In order to help derive the uncertainty propagation, the first three terms of Equation 8.2 are:

$$P_F(0) = \frac{P_T(0)}{P_B(0)} \tag{C.1}$$

$$P_F(1) = \frac{P_T(1)}{P_B(0)} - \frac{P_F(0) \cdot P_B(1)}{P_B(0)} \tag{C.2}$$

$$P_F(2) = \frac{P_T(2)}{P_B(0)} - \frac{P_F(0) \cdot P_B(2)}{P_B(0)} - \frac{P_F(1) \cdot P_B(1)}{P_B(0)} \tag{C.3}$$

The terms $P_F(i)$, $P_B(i)$, and $P_T(i)$ refer to the probability of i γ-rays being detected associated with fission, the underlying background or the total measured data, respectively. The uncertainty propagation for each of these equations will be demonstrated and the

underlying pattern identified. First, a key definition needs to be made clear:

$$P_A(i) = \frac{N_A(i)}{\sum_{i=0}^{i=10} N_A(i)} = \frac{N_A(i)}{N_A}, \tag{C.4}$$

where $N_A(i)$ refers to the number of events corresponding to i γ rays for any event A, where A may be replaced with F, B, or T for fission, background or total. The uncertainty propagation for this general relationship is important and will percolate throughout the subsequent uncertainty calculations. This relationship is:

$$\sigma_{P_A(i)}{}^2 = P_A(i)^2 \cdot \left(\left(\frac{\sigma_{N_A(i)}}{N_A(i)} \right)^2 + \left(\frac{\sigma_{N_A}}{N_A} \right)^2 \right) \tag{C.5}$$

It is also important to note, that as the uncertainties on these measurements are based on Poisson statistics (i.e. the uncertainty is the square root of the number of counts) the above relationship may be simplifed.

$$\left(\frac{\sigma_{N_A(i)}}{N_A(i)} \right)^2 = \left(\frac{\sqrt{N_A(i)}}{N_A(i)} \right)^2 = \left(\frac{1}{\sqrt{N_A(i)}} \right)^2 = \frac{1}{N_A(i)} \tag{C.6}$$

Therefore, building from these key principles, the uncertainty propagation for Equation C.1 follows the equation:

$$\sigma_{P_F(0)}{}^2 = P_F(0)^2 \left(\left(\frac{\sigma_{P_T(0)}}{P_T(0)} \right)^2 + \left(\frac{\sigma_{P_B(0)}}{P_B(0)} \right)^2 \right) \tag{C.7}$$

Combining Equations C.5 and C.6 with Equation C.7, the following relationship follows:

$$\sigma_{P_F(0)}{}^2 = P_F(0)^2 \left(\frac{1}{N_T(0)} + \frac{1}{N_T} + \frac{1}{N_B(0)} + \frac{1}{N_B} \right) \tag{C.8}$$

Treatment of Equation C.2 is slightly more complex, as there are now two terms within the equation. If we consider these terms as "A" and "B" (where $C = A - B$), then the following relationship applies:

$$\sigma_C{}^2 = \sigma_A{}^2 + \sigma_B{}^2 \tag{C.9}$$

Treating each term separately and propagating the uncertainties as shown in the previous step Equation C.2 gives:

$$A = \frac{P_T(1)}{P_B(0)}. \tag{C.10}$$

The uncertainty for this term may be calculated in the same fashion as for Equation C.1, giving:

$$\sigma_A{}^2 = \frac{P_T(1)^2}{P_B(0)^2}\left(\frac{1}{N_T(1)} + \frac{1}{N_T} + \frac{1}{N_B(0)} + \frac{1}{N_B}\right) \tag{C.11}$$

Where $A^2 = \frac{P_T(1)^2}{P_B(0)^2}$ has been substituted in. Now propagating uncertainty on the next term, B, using the base equation:

$$B = \frac{P_F(0) \cdot P_B(1)}{P_B(0)} \tag{C.12}$$

Propagating the uncertainties in the same way as previously, gives the equation:

$$\sigma_B{}^2 = \left(\frac{P_F(0) \cdot P_B(1)}{P_B(0)}\right)^2 \left(\frac{1}{N_B(1)} + \frac{1}{N_B} + \frac{1}{N_B(0)} + \frac{1}{N_B} + \frac{1}{N_F(0)} + \frac{1}{N_F}\right) \tag{C.13}$$

Therefoe Equation C.9 becomes

$$\begin{aligned}\sigma_C{}^2 = &\frac{P_T(1)^2}{P_B(0)^2}\left(\frac{1}{N_T(1)} + \frac{1}{N_T} + \frac{1}{N_B(0)} + \frac{1}{N_B}\right) + \\ &\left(\frac{P_F(0) \cdot P_B(1)}{P_B(0)}\right)^2 \left(\frac{1}{N_B(1)} + \frac{1}{N_B} + \frac{1}{N_B(0)} + \frac{1}{N_B} + \frac{1}{N_F(0)} + \frac{1}{N_F}\right)\end{aligned} \tag{C.14}$$

This process may then be repeated, and the general equation determined.

$$\sigma_F(k)^2 = \frac{P_T(k)}{P_B(0)}\left[\frac{1}{N_T(k)}+\frac{1}{N_B(0)}+\frac{1}{N_B}+\frac{1}{N_T}\right]+ \sum_i^k M_{i(k-i)}\left(\frac{1}{N_B(0)}+\frac{1}{N_F(i)}+\frac{1}{N_B(k-i)}+\frac{1}{N_F}+\frac{1}{N_B}+\frac{1}{N_B}\right), \quad \text{(C.15)}$$

where the coefficients given by M are

$$M_{ij} = \frac{P_F(i)\cdot P_B(j)}{P_B(0)}. \quad \text{(C.16)}$$

This is the final uncertainty propagation equation, as discussed in Chapter 8.